DESIGN AND PERFORMANCE TESTING OF COUNTER-CROSS-FLOW RUN-AROUND MEMBRANE ENERGY EXCHANGER SYSTEM

A Thesis Submitted to the College of

Graduate Studies and Research

In Partial Fulfillment of the Requirements

For the Degree of Master of Science

In the Department of Mechanical Engineering

University of Saskatchewan

Saskatoon

By

KHIZIR MAHMUD

Permission to Use

In presenting this thesis in partial fulfilment of the requirements for a postgraduate degree from the University of Saskatchewan, I agree that the Libraries of this University may make it freely available for inspection. I further agree that permission for copying of this thesis in any manner, in whole or in part, for scholarly purposes may be granted by the professor or professors who supervised my thesis work or, in their absence, by the Head of the Department or the Dean of the College in which my thesis work was done. It is understood that any copying or publication or use of this thesis or parts thereof for financial gain shall not be allowed without my written permission. It is also understood that due recognition shall be given to me and to the University of Saskatchewan in any scholarly use which may be made of any material in my thesis.

Requests for permission to copy or to make other use of material in this thesis in whole or part should be addressed to:

Head of the Department of Mechanical Engineering

University of Saskatchewan

Saskatoon, Saskatchewan (S7N 5A9)

ABSTRACT

In this study, a novel counter-cross-flow run-around membrane energy exchanger (RAMEE) system was designed and tested in the laboratory. The RAMEE system consists of two (2) counter-cross-flow Liquid-to-Air Membrane Energy Exchangers (LAMEEs) to be located in the supply and exhaust air streams in the building Heating Ventilation and Air-Conditioning (HVAC) system. Inside each exchanger, a micro-porous membrane separates the air and liquid streams and allows transfer of the sensible and latent energy from the air stream to the liquid stream or vice-versa. The system exchanges sensible and latent energy between supply and exhaust air streams using a desiccant solution loop. The supply and exhaust air streams in the RAMEE can be located far apart from each other or adjacent to each other. The flexibility of non-adjacent ducting makes the RAMEE system a better alternative compared to available energy recovery systems for the retrofit of HVAC systems.

Two counter-cross-flow exchangers for the RAMEE system were designed based on an industry recommended standard which is to obtain a target overall system effectiveness of 65% for the RAMEE system at a face velocity of 2 m/s. The exchanger design was based on heat exchanger theory and counter-cross-flow design approach. An exchanger membrane surface aspect ratio (ratio of exchanger membrane surface height to exchanger length) of 1/9 and the desiccant solution entrance ratio (ratio of desiccant solution entrance length to exchanger length) of 1/24 were employed. Based on different heat transfer case studies, the energy transfer size of each exchanger was determined as

1800 mm x 200 mm x 86 mm. Propore^{TM} was used as the membrane material and Magnesium-Chloride solution was employed as the desiccant solution.

The RAMEE performance (sensible, latent and total effectiveness) was evaluated by testing the system in a run-around membrane energy exchanger test apparatus by varying the air stream and liquid solution-flow rates at standard summer and winter operating conditions. From the test data, the RAMEE effectiveness values were found to be sensitive to the air and solution flow rates. Maximum total effectiveness of 45% (summer condition) and 50% (winter condition) were measured at a face velocity ≈ 2 m/s. A comparison between the experimental and numerical results from the literature showed an average absolute discrepancy of 3% to 8% for the overall total system effectiveness. At a low number of heat transfer units, i.e. NTU = 4, the numerical and experimental results show agreement within 3% and at NTU = 12 the experimental data were 8% lower than the simulations. The counter-cross-flow RAMEE total system effectiveness were found to be 10% to 20% higher than those reported for a cross-flow RAMEE system by another researcher.

It is thought that discrepancies between experimental and predicted results (design and numerical effectiveness) may be due to the mal-distributed desiccant solution-flow, desiccant solution leakage, lower than expected water vapor permeability of the membrane, uncertainties in membrane properties (thickness and water vapor permeability) and heat loss/gain effects. Future research is needed to determine the exact cause of the discrepancies.

ACKNOWLEDGMENTS

The completion of this thesis would be impossible without the support and encouragement of many people, to whom I extend my deepest gratitude.

I would like to foremost acknowledge my supervisors, Prof. R.W. Besant and Prof. C.J. Simonson for their time and continuing support throughout this research. Without their assistance and motivation this work would not have been possible. Their patience, encouragement, understanding, are greatly appreciated. I am truly grateful for their mentorship and dedication.

Special thanks to the committee members, Prof. David Sumner and Prof. Greg J. Schoenau, for their recommendations and suggestions.

I also acknowledge the invaluable assistance of Mr. Chris James, Mr. Dave Deutscher, and David Beriault in facilitating the experimental components of this research.

Most importantly, I would like to express my deepest appreciation to my parents, brothers and sisters, who always encouraged and supported my educational pursuits, no matter what the cost and personal sacrifice.

I would like to thank my relatives and friends for their prayers and support. More specifically I would like to thank Zobayer Abdullah Khizir and Sheikh Hasibul Majid.

I also would like to acknowledge financial support from the Natural Science and Engineering Research Council of Canada (NSERC) and Venmar CES Inc, Saskatoon.

Dedication

To my parents, Late Sk. Muhammad Ali and Mrs Shafiqun Nahar.

It’s a blessing to have parents like you.

TABLE OF CONTENTS

page

LIST OF TABLES

LIST OF FIGURES

NOMENCLATURE

ACRONYMS

AAD	Average Absolute difference
AHRI	Air-conditioning Heating and Refrigerating Institute
ANSI	American National Standard Institute
ASHRAE	American Society of Heating, Refrigerating and Air-Conditioning Engineers
CAD	Computer Aided Design
DAQ	Data Acquisition
ER	Energy Recovery
ERV	Energy Recovery Ventilator
GPM	Gallon Per Minute (US)
HVAC	Heating, Ventilation and Air-Conditioning
LAMEE	Liquid-to-Air Membrane Energy Exchanger
RAMEE	Run-Around Membrane Energy Exchanger
RAMEETA	Run-Around Membrane Energy Exchanger Testing Apparatus
RMSE	Root Mean Square Error
RTD	Resistance Temperature Detector
SD	Standard deviation
SP	Solution Pump
VF	Vacuum Fan

ENGLISH SYMBOLS

a	coefficient used for salt solution density correlation

A	membrane area (mm^2)
A_{face}	face area of the exchanger (LAMEE)
b	coefficient used for salt solution density correlation
B	bias error
c	coefficient used for salt solution density correlation
C	heat capacity rate (W/K)
C_d	discharge coefficient
Cn_{sol}	concentration of the desiccant solution by mass (%)
C_{sol}/C_{air}	heat capacity rate ratio of desiccant solution to air
C_r	heat capacity rate ratio of minimum and maximum fluid (C_{min}/C_{max})
c_p	specific heat capacity [J /(kg.K)]
C_f	friction coefficient
d	diameter of the orifice plate opening (mm)
D	inside pipe diameter (mm)
D_h	hydraulic diameter (mm)
e_r	entrance ratio
EI	exhaust exchanger inlet
EO	exhaust exchanger outlet
f	friction factor
H	height of the exchanger (m)
H_{mem}	height of the membrane surface (m)
h	enthalpy (J/kg)
h_f	head loss due to friction

h	convective heat transfer coefficient [W/ (m^2.K)]
h_m	convective mass transfer coefficient [W/ (m^2.K)]
k	thermal conductivity [W/ (m.K)]
K_m	water vapor permeability of membrane [kg/(m·s)]
Le	Lewis number
L	length
$L_{sol,e}$	entrance length of the desiccant solution
$\dot{m}$	mass flow rate (kg/s)
n	number of liquid panels or air channel
N	number of observation
NTU	number of heat transfer units
NTU_m	number of mass transfer units
Nu	Nusselt number
P	pressure (Pa)
P	precision error
Pe	Peclet number
Pr	Prandtl number
q	volume flow rate (m^3/s)
Q	heat loss/gain either for supply or exhaust side
Q_{be}	heat loss/gain between exchanger (i.e. desiccant solution-flow path connecting the supply and exhaust exchanger)
Q_{total}	total energy transfer inside a single exchanger
r	coefficient used for salt solution heat capacity correlation

r*	coefficient used for salt solution viscosity correlation
R	universal gas constant
R	calculated parameters
RH	relative humidity
Re	Reynolds number
SI	supply exchanger inlet
SO	supply exchanger outlet
t_{mem}	membrane thickness
t_{air}	air-flow gap
t_{sol}	solution-flow gap
$t_{o.screen}$	thickness of the outer screen
t*	student-t value
t	time (minute)
T	temperature (^{o}C)
U	overall heat transfer coefficient [W /(m^{-2}.K)]
U	uncertainty with a 95% confidence
U_m	overall mass transfer coefficient [kg/ (m^2.s)]
V	bulk mean velocity (m/s)
W_{air}	humidity ratio ($kg_{water\ vapor}/kg_{dry\ air}$)
W	width
X	air properties (Temperature , Humidity ratio, and Enthalpy)
x , y , z	coordinates

GREEK SYMBOLS

β	orifice plate expansion coefficient (d/D)
d	ratio of heat loss/gain between exchanger to total energy transfer
Δ	difference
ε	effectiveness
λ	ratio of desiccant solution mass in the exchangers to the total solution mass in the RAMEE system
μ	viscosity (Pa.s)
ρ	density (kg/m^3)
σ_{sol}	heat loss/gain ratio between exchangers to total heat energy transfer inside an exchanger based on solution properties
σ_{air}	ratio of heat loss/gain ratio between exchangers to total heat energy transfer inside an exchanger based on air properties

SUBSCRIPTS

air	air
atm	atmosphere
avg	average
e	entrance length
(e)	exhaust exchanger
exhaust	exhaust exchanger side
face	exchanger face
in	inside exchanger
initial	initial condition of the test

max	maximum
mem	membrane
min	minimum
o	overall
(s)	supply exchanger
sat	saturation
sol	desiccant solution
supply	supply exchanger side
vap	water vapor
x	sensible, latent or total effectiveness
+	positive charge
-	negative charge

CHAPTER 1
INTRODUCTION

1.1 Overview

World energy consumption is growing rapidly due to the increasing energy demand by emerging and developed economies. The increasing energy demand has already raised concern over energy supply difficulties, exhaustion of energy resources and environmental impacts (e.g. global warming and climate change). Around 20%-40% of the total world energy is consumed by residential and commercial building services in the developed countries. Among building services, Heating, Ventilating and Air-conditioning (HVAC) systems account for 50% of the total building energy consumption and around 10-20% of the total world energy consumption. The energy demand of building services is predicted to grow due to population growth, increasing demands for comfort and air quality, and the rise in time spent inside buildings. Therefore HVAC system design for buildings is a major area for energy conservation consideration today (Pérez-Lombard et al., 2008).

In a HVAC system, substantial energy is consumed to modify the supply air (i.e. ventilation air) temperature and humidity in order to maintain a comfortable and healthy indoor environment for building occupants based on ANSI/ASHRAE Standard 55-2004. The energy consumption of HVAC systems could be reduced by reducing outdoor ventilation air-flow rates. However, lower ventilation air-flow rates reduce the capability of the HVAC system to lower contaminant concentrations (e.g. dust, odors, smoke and bacteria) affecting occupant health (Redlich et al., 1997). As a result, ventilation

standards are developed to provide sufficient ventilation air for maintaining healthy indoor environments. The ASHRAE ventilation standard has changed during the past decades. After the 1970s energy crisis the standard ventilation air-flow rate was reduced to 2.5 L/s per person for a typical office building (ANSI/ASHRAE Standard 62.1-1981). However, this reduced ventilation flow rate adversely affected the health of occupants in many buildings. To reduce the risk of occupant health effects and when the energy price was eased, the rate first increased to 10 L/s person in 1985 and then decreased somewhat to 8.5 L/s per person (ANSI/ASHRAE Standard 62.1-2004).

It has been an on-going challenge for HVAC designers to provide a healthy environment for occupants inside buildings while minimizing energy consumption.

1.2 Air-to-air energy recovery systems

The energy required to condition the supply air could be reduced if energy from the exhaust air is used to pre-condition the supply air. Based on this idea, air-to-air Energy Recovery (ER) systems have been developed. Sometimes ER systems are called Energy Recovery Ventilators (ERVs). In an air-to-air ER system, an ER device is installed between the supply and exhaust air ducting which transfers energy between the supply and exhaust air streams to reduce energy consumption to condition the ventilation air. Due to the energy transfer, the air temperature (T), humidity ratio (W) and enthalpy (h) changes as the air flows through the ER device. Figure 1-1 shows a schematic of a HVAC system with an air-to-air ER system. Figure 1-1 also shows different air properties before and after the ER device.

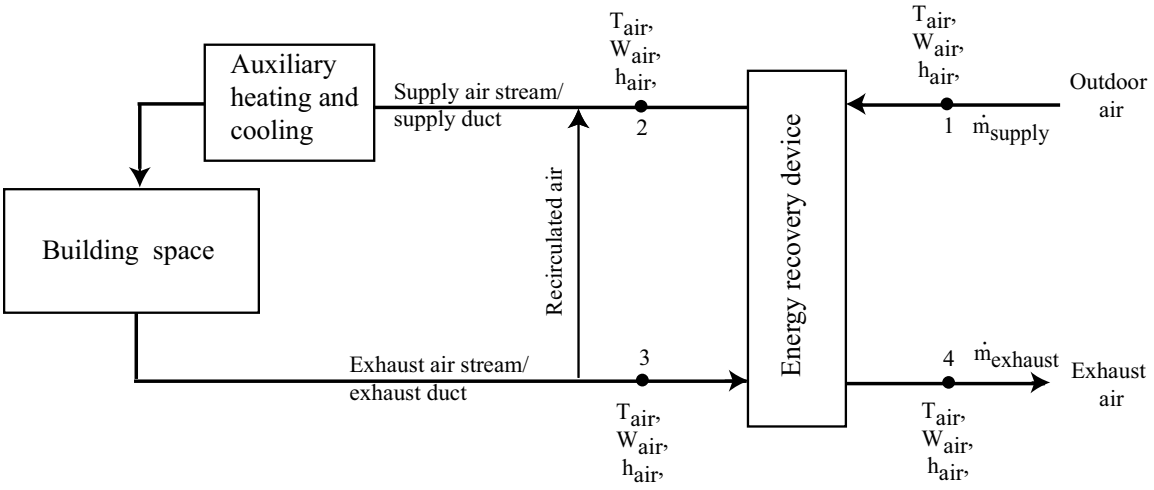

Figure 1-1. A schematic of a HVAC system with an air-to-air energy recovery system

1.2.1 Literature review

Several studies have been done on the economics and performance of different ER systems. The study of ER system economics includes the initial investment, operating costs and saving. Fehrm et al. (2002) showed that final energy consumption in buildings with an ER system can be reduced up to 20%. Besant and Simonson (2003) discussed various air-to-air ER systems and studied the energy savings possibility with air-to-air ER systems in a building. Based on a case study for the design condition of Chicago, they reported that the annual energy consumption for heating and cooling ventilation air could be reduced by up to 64% and 31%, respectively. As well, the required capacity of the boiler and chiller for ventilation air conditioning could be reduced by up to 44% and 52%, respectively.

Initially, ER devices were developed to transfer only sensible energy (indicated by temperature change, ΔT). A sensible energy recovery device is called a heat exchanger. Some of the commonly used heat exchangers include aluminum flat plate heat exchangers, heat pipes and heat wheels. However, in recent years, increasing attention

has been paid to develop ER devices which can transfer both sensible and latent energy (indicated by moisture change, ΔW) for maintaining standard indoor moisture content and temperature based on ANSI/ASHRAE Standard 55-2004. These devices are called energy or enthalpy exchangers. Currently available energy exchangers include energy wheels and flat plate exchangers (paper or membrane based). Besant and Simonson (2000) compared the energy recovery performance of heat exchangers and energy exchangers at various indoor and outdoor temperature differences. Besant and Simonson (2000) also recommended the selection of a heat or energy exchanger based on different design conditions. These data are very useful for selecting an energy recovery device for specific design conditions.

Zhang and Jiang (1999) presented a heat and mass transfer model of an Energy Recovery Ventilator (ERV) which used a porous membrane to transfer heat and moisture. They reported that a HVAC system equipped with a membrane based cross-flow ERV system could reduce energy consumption by 24%. Niu and Zhang (2001) studied the effect of different membrane materials on the sensible, latent and total effectiveness values of a cross-flow membrane exchanger by using a finite-difference numerical model. They reported that the sensible effectiveness is not sensitive to membrane or operating conditions but a strong relationship was found between the latent effectiveness, operating conditions and membrane materials.

Kistler and Cussler (2002) studied, built and tested a hollow fiber membrane exchanger for transferring heat and moisture. Their membranes were highly permeable to water vapor and impermeable to some toxic gases. Their test results, which are based on Arkansas climate, showed promising sensible and latent energy recovery. Johnson et al.

(2003) proposed the use of fiber materials in an evaporative cooling application as a wetted material. Fiber materials were housed within a frame positioned within the duct to allow cross-flow. The authors reported that the effectiveness of this exchanger could be comparable to conventional evaporative cooling equipment by using the appropriate number of fibers and membrane surface area.

Most ER devices were initially developed for transferring energy between adjacent supply and exhaust air ducting in a HVAC system. However, with the growing concern of the world energy conservation, the need for special ER devices to retrofit old buildings, where supply and exhaust ducts may not be side-by-side, has emerged. As a result, different ER devices have been developed to serve this purpose, including the twin-tower enthalpy recovery loop and the glycol run-around system (ASHRAE, 2005). These systems have two different exchangers in the supply and exhaust air streams/ducting and transfer either heat (glycol run-around system) or heat and moisture (twin-tower) through a circulating fluid.

Many numerical and experimental works considering different aspects of run-around heat exchangers have been undertaken and promising energy recovery rates have been reported. (Emerson, 1984; Zeng, 1990; Zeng et al., 1992; Bennett et al., 1994; Dhital et al., 1995; Johnson et al., 1995; and Fan et al., 2005).

Forsyth and Besant (1988) analyzed and optimized the design of a run-around heat recovery system for a given airflow, temperature and humidity. They analyzed the sensitivity of effectiveness to different system parameters and compared numerical data with measured data from an existing system. The system parameters included glycol Reynolds number, air Reynolds number, glycol flow, tube diameter, fin spacing , fin

thickness, tube spacing, coil height, coil width, supply air temperature and supply air-flow. From the parametric study they found that the exchanger effectiveness is most sensitive to the glycol Reynolds number.

1.2.3 Existing ER systems

Currently available ER systems can be divided into four categories. These four categories are based on the combination of energy transfer mode and ducting arrangements as shown in Figure 1-2.

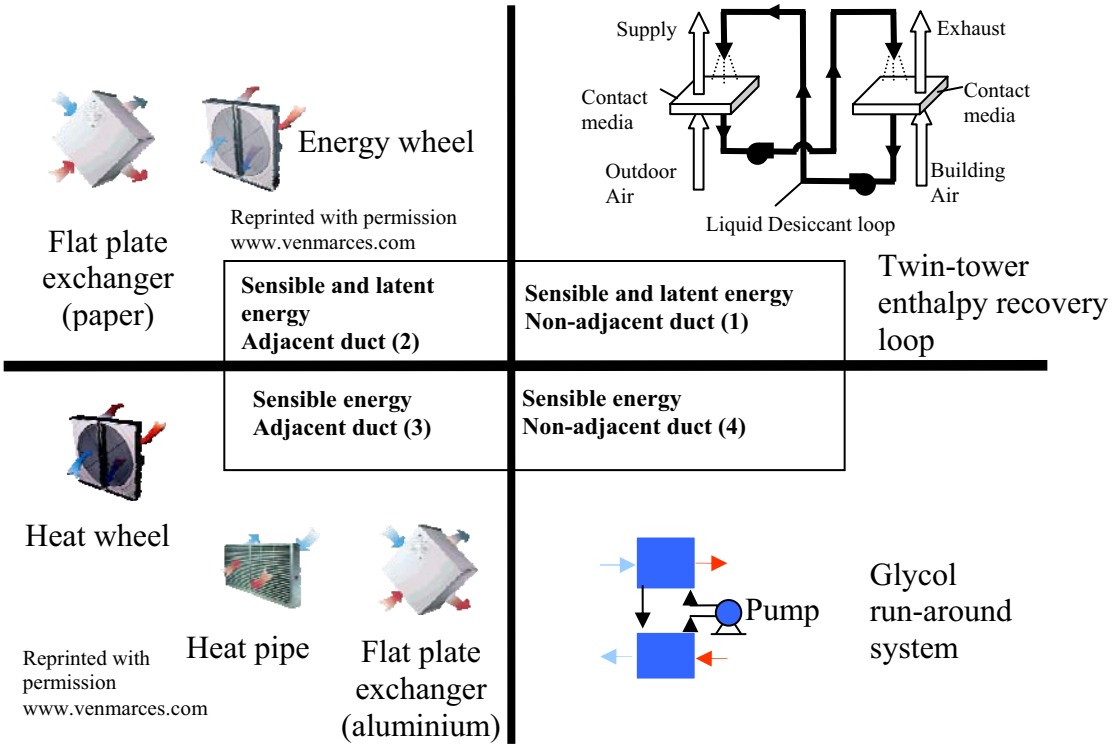

Figure 1-2. Divisions of Energy Recovery (ER) systems (Larson, 2006)

1.2.4 ER test standards and effectiveness

With the development of different ER devices, performance evaluation standards for ER devices have also been developed. According to ASHRAE Standard 84-2008, the performance of an air-to-air ER system is evaluated based on the effectiveness (ε), which

is a ratio of the actual transfer rate of heat, moisture or both heat and moisture, to the maximum possible transfer rate (equation 1.1). The ability of an exchanger to transfer heat is quantified by the sensible energy effectiveness. The mass transfer characteristics of an exchanger that transfers moisture/water vapor between two air streams/ducting are given by the latent energy effectiveness. The total energy or enthalpy effectiveness includes the effects of both the heat and mass transfer phenomena.

$$\varepsilon_x = \frac{\dot{m}_{air,supply}\left(X_1 - X_2\right)}{\dot{m}_{air,min}\left(X_1 - X_3\right)} = \frac{\dot{m}_{air,exhaust}\left(X_4 - X_3\right)}{\dot{m}_{air,min}\left(X_1 - X_3\right)} \tag{1.1}$$

Here

Subscript x = sensible, latent or total effectiveness

X = T, (^{o}C) dry bulb temperature for sensible energy effectiveness,

= W ($kg_{water\ vapor}/kg_{dry\ air}$), humidity ratio for latent energy effectiveness,

= h (J/kg), enthalpy for total energy effectiveness

$\dot{m}_{air,supply}$ = supply dry air mass flow rate (kg/s), average dry air mass flow rate of position 1 and 2 (Figure 1-1)

$\dot{m}_{air,exhaust}$ = exhaust dry air mass flow rate (kg/s), average dry air mass flow rate of position 3 and 4 (Figure 1-1)

$\dot{m}_{air,min}$ = minimum dry air mass flow rates (kg/s) between the supply and exhaust air, $\dot{m}_{air,min} = \min\left(\dot{m}_{air,supply}, \dot{m}_{air,exhaust}\right)$.

Equation (1.1) is based on the assumptions of steady-state conditions and no energy exchange between the ER device and the surroundings. Condensation or frosting is also considered negligible.

The minimum total energy effectiveness of an ER system is 50%, as required by ASHRAE Standard 90.1. Besant and Simonson (2003) reported currently available ER systems have total effectiveness from 40-85%.

1.2.5 Ideal air-to-air energy recovery system

Different ER devices (Figure 1-2) have been developed to reduce building energy consumption and each of the ER devices has its own advantages and disadvantages (Besant and Simonson, 2003). According to ASHRAE (2004), an ideal air-to-air recovery system is one which fulfills the following criteria:

- Allows sensible energy transfer between the exhaust and supply air streams;
- Allows latent energy transfer between the exhaust and supply air streams;
- Allows no significant transfer of air contaminants (e.g. other gases, pollutants, biological contaminants and particulates) between the exhaust and supply air streams.

The above criteria from ASHRAE (2004) work well for most new buildings, but are not complete for existing buildings; retrofitting existing buildings should also be considered because of the slow building replacement rate of 2% to 3% per year. As mentioned earlier, non-adjacent ducting is one of the major concerns when retrofitting buildings. Non-adjacent ducting is also very important for new applications, where slight cross contamination can cause serious health effects (e.g. hospitals, laboratories, and manufacturing facilities). As a result, the ability of the ER system to transfer heat and moisture between non-adjacent ducts is an important criterion that should be added to the ASHRAE (2004) criteria to develop the criteria for an ideal ER system.

Based on the ASHRAE (2004) and non-adjacent ducting criteria, none of the four groups of ER systems in Figure 1-2 satisfy the criteria of an ideal air-to-air ER system. Group 3 and 4 fail to qualify because they only transfer heat (i.e. sensible energy). Heat wheels, heat pipes and aluminum flat plate exchangers only transfer sensible energy with adjacent ducting; whereas, glycol run-around systems transfer only sensible heat. Flat plate exchangers (paper or membrane based) and energy wheels transfer both sensible and latent energy but do not allow non-adjacent ducting. As a result, the exchangers in Group 2 fail to meet the criteria of an ideal exchanger. Twin-tower enthalpy recovery loops in Group 1 also fail because there is a possibility of contamination in this open system where the liquid desiccant solution comes in direct contact with the air stream.

As a result, an ideal air-to-air ER system which satisfies both the ASHRAE (2004) and non-adjacent ducting criteria is still needed. The idea of developing such a system started with the idea of modifying glycol run-around systems with moisture transfer ability. To allow moisture transfer, a semi-permeable membrane is used in the system. The membrane also serves as a separator between the air and liquid in each exchanger. This makes the system a closed system. A coupling liquid, which has the ability to absorb and desorb water vapor from/to air streams, is used in a closed loop between the supply and exhaust exchangers to transfer heat and moisture between the air streams. Since the system is a Run-Around (RA) system and uses a Membrane (M) as an exchange interface to Exchange (E) Energy (E) it is called the Run-Around Membrane Energy Exchanger (RAMEE).

A research project has been initiated at the University of Saskatchewan (in partnership with Venmar CES Inc.) to investigate the design, performance (both experimentally and

numerically), limitations, advantages and disadvantages of the RAMEE system. The research presented in this thesis is a part of the RAMEE research project and it is aimed to design, build and test a RAMEE system in the laboratory.

1.3 RAMEE system

The RAMEE system consists of two Liquid-to-Air Membrane Energy Exchangers (LAMEEs). The membranes are semi-permeable is that they are permeable to water vapor but impermeable to liquid water. More details on membrane properties can be found in Chapter 2 and Larson (2006). The two LAMEEs are coupled with a liquid desiccant (or desiccant solution) flow loop. The liquid desiccant gains or releases water depending on the humidity and temperature of the air stream. The liquid desiccant properties are presented in Chapter 2.

One of the two LAMEEs in a RAMEE system is located in the supply air stream entering the building, and the other one is located in the exhaust air stream leaving the building. A schematic of the RAMEE system is shown in Figure 1-3.

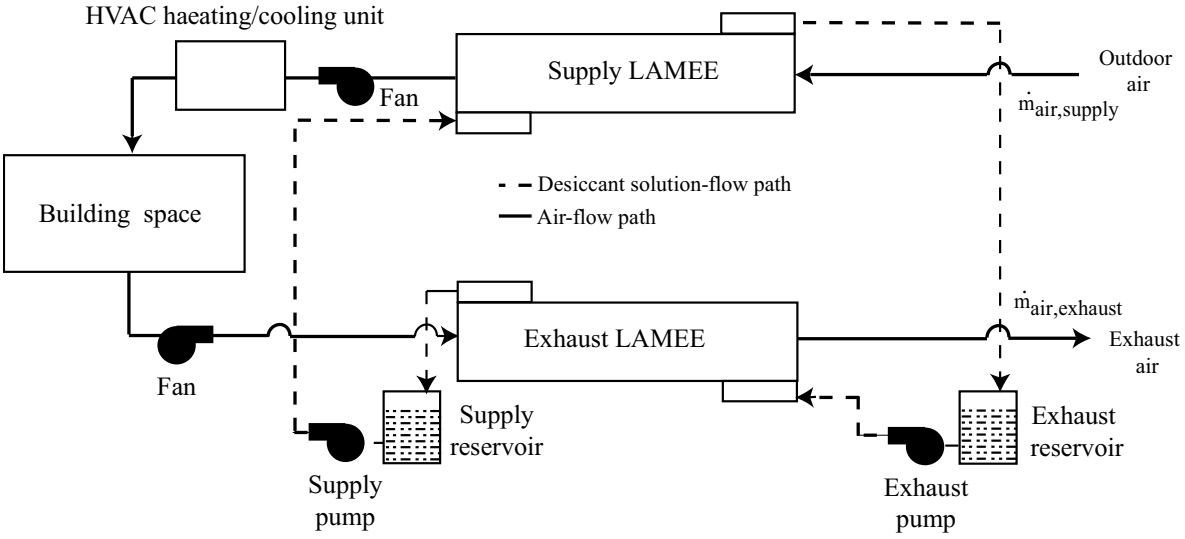

Figure 1-3. Schematic of a Run-Around Membrane Energy Exchanger (RAMEE) system

Heat and water vapor are transported between the two LAMEEs by the desiccant solution which flows in a closed liquid loop. The fans that provide the air-flow and the pumps that provide the solution-flow are the only components in the RAMEE system that require external power input during operation.

The desiccant solution gains or loses water from/to the air streams through the semi-permeable membrane inside each LAMEE. As a result, the solution volume changes as it flows through the loop. In order to allow for the volume changes of the solution-flow, two desiccant storage tanks/reservoirs are placed in the RAMEE system as shown in Figure 1-3.

RAMEE systems could be counter or cross or counter-cross-flow based on the solution-flow configuration relative to the air stream inside the LAMEEs. Figure 1-4 shows LAMMEs with different solution flow configurations. The air and desiccant solution flow in opposite directions in the counter-flow LAMEE (Figure 1-4a) and in perpendicular directions in the cross-flow LAMEE (Figure 1-4b). In the counter-cross-flow configuration, the desiccant solution enters through a small portion ($L_{sol,e}$) of the header of the exchanger. At the entrance of the LAMEE, the desiccant solution flows in a cross-flow direction relative to the air; but in the middle of the LAMEE, the solution flows mostly in the counter-flow direction relative to the air-flow (Figure 1-4c).

In all the three LAMEE configurations, desiccant solution can enter the liquid panel of the exchanger either from the bottom or top. However, only the bottom-to-top flow configuration is illustrated in Figure 1-4.

After entering the liquid panel, desiccant solution flow occurs in-between two semi-permeable membranes in all three configurations (Figure 1-4). In the Figure 1-4, average

air and solution-flow gap is represented by t_{air}, t_{sol} whereas membrane thickness, membrane height and membrane length is represented by t_{mem}, H_{mem}, and L.

(a)

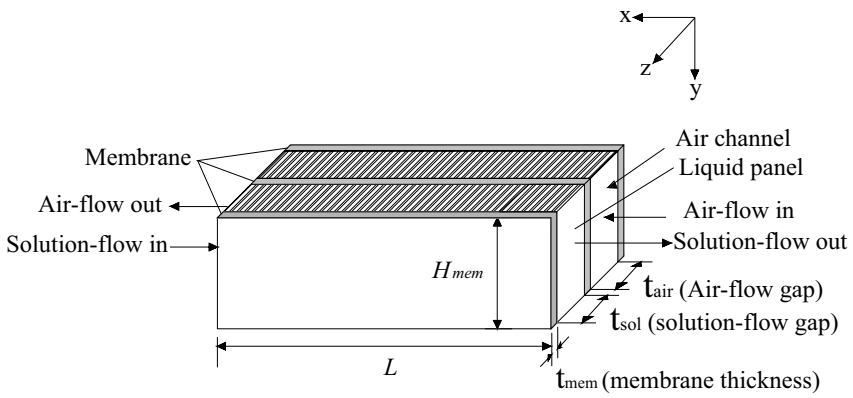

(b)

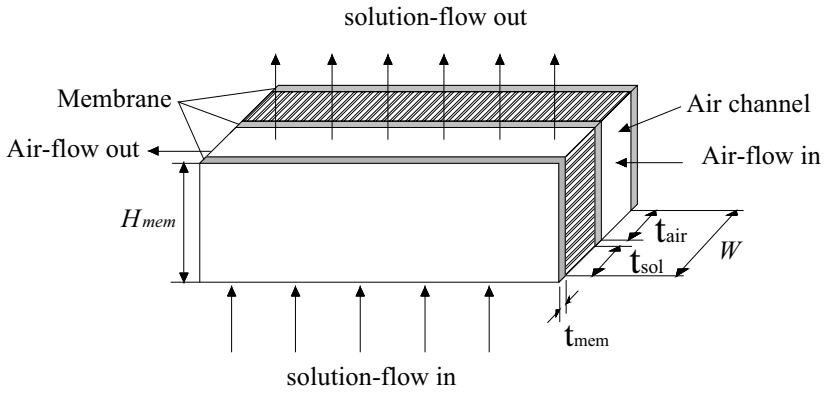

(c)

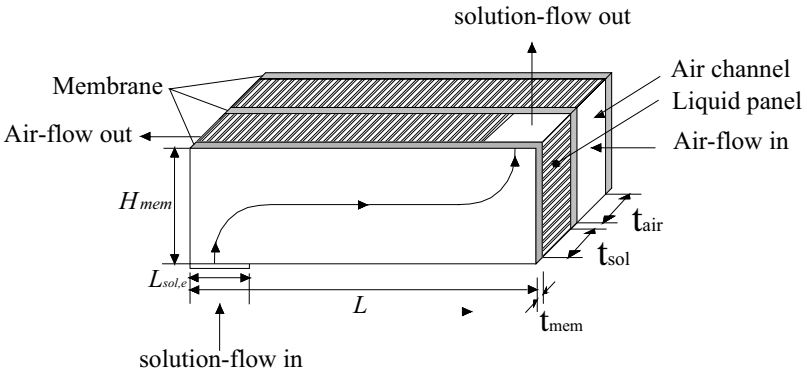

Figure 1-4. A Liquid-to-Air Membrane Energy Exchanger (LAMEE) designed with a) counter-flow, b) cross-flow and c) counter-cross-flow arrangements

Inside each liquid panel, the membrane allows water vapor to diffuse normal to the plane of the membrane in the z direction. The membranes also restrict desiccant solution from entering the air channel.

1.4 RAMEE performance evaluation

RAMEE performance can be evaluated based on the actual amount of heat and moisture transfer with respect to maximum amount of heat and moisture transfer. The amount of heat and moisture transfer can be evaluated either from the air or desiccant solution property change before and after each LAMEE in a RAMEE system shown in Figure 1-5. The supply and exhaust LAMEEs are indicated by (s) and (e), respectively. A RAMEE system transfer energy between the supply and exhaust air streams. Therefore, the energy transfer effectiveness of supply and exhaust air streams can be calculated based on ASHRAE standard 84-2008. In addition to that, HVAC engineer can accurately measure air properties and is most interested in air properties. Therefore, supply and exhaust air stream effectiveness of the RAMEE system is defined based on air properties in this thesis. Supply and exhaust air stream effectiveness also represents the supply and exhaust LAMEE effectiveness. Table 1-1 tabulates the effectiveness of supply and exhaust air streams (i.e. supply and exhaust LAMEE).

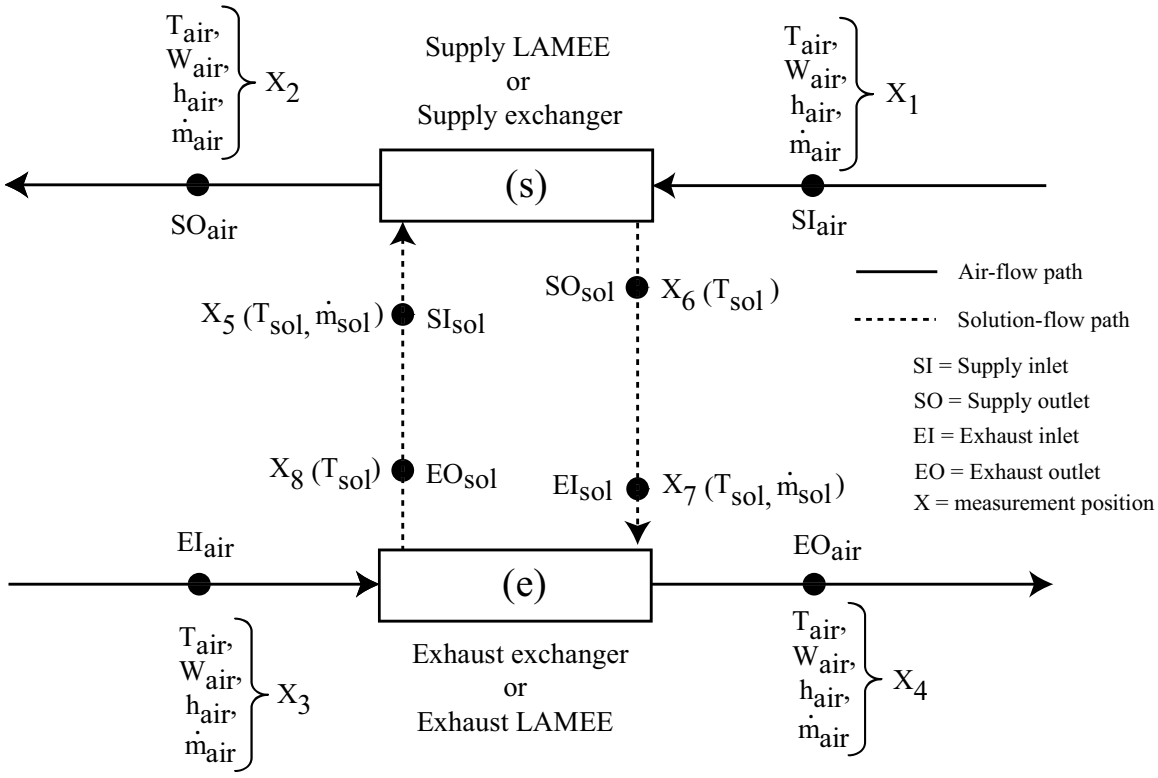

Figure 1-5. Air and solution properties before and after each LAMEE in a RAMEE system

Table 1-1. RAMEE effectiveness (supply and exhaust) based on air properties

Supply LAMEE		*Exhaust LAMEE*	
$\varepsilon_{o,x,(s)} = \dfrac{\dot{m}_{air,supply}(X_1 - X_2)}{\dot{m}_{air,min}(X_1 - X_3)}$	(1.2a)	$\varepsilon_{o,x,(e)} = \dfrac{\dot{m}_{air,exhaust}(X_4 - X_3)}{\dot{m}_{air,min}(X_1 - X_3)}$	(1.2b)

From equation (1.2) is it evident that, the maximum possible energy transfer of the LAMEEs is based on the RAMEE system. Therefore, an additional subscript "o" is used in the LAMEE effectiveness symbol. At the steady-state condition the supply and exhaust LAMEE effectiveness will be equal (equation 1.3) and the overall RAMEE effectiveness

can be calculated as the average of the supply and exhaust LAMEE effectiveness (equation 1.4),

$$\varepsilon_{o,x,(s)} = \varepsilon_{o,x,(e)} = \varepsilon_{o,x} \tag{1.3}$$

$$\frac{\varepsilon_{o,x,(s)} + \varepsilon_{o,x,(e)}}{2} = \varepsilon_{o,x} \tag{1.4}$$

where $\varepsilon_{o,x}$ represents the overall sensible, latent or total effectiveness of the RAMEE system.

To avoid repetition, the overall effectiveness values of the supply ($\varepsilon_{o,sensible,(s)}, \varepsilon_{o,latent,(s)}, \varepsilon_{o,total,(s)}$) and exhaust LAMEE ($\varepsilon_{o,sensible,(e)}, \varepsilon_{o,latent,(e)}, \varepsilon_{o,total,(e)}$) of the RAMEE system are referred to as supply and exhaust exchanger effectiveness in this thesis. Similarly, the overall effectiveness of the RAMEE system ($\varepsilon_{o,sensible}, \varepsilon_{o,latent}, \varepsilon_{o,total}$) is referred to as the RAMEE effectiveness, $\varepsilon_{o,x}$.

1.5 Previous RAMEE research

1.5.1 Fan (2005)

Fan (2005) published the first thesis on the RAMEE system. The thesis presented a numerical study of a cross-flow RAMEE system using a very high performing polytetrafluoroethylene (PTFE) membrane. The results showed that the maximum effectiveness occurs at C_{sol}/C_{air} of 3 (C is the heat capacity rate, W/K) and varies with Number of Transfer Unit (NTU). NTU is defined as follows (Incropera and Dewitt, 2002),

$$NTU = \frac{UA}{C_{min}} \tag{1.5}$$

where, U is the overall heat transfer coefficient, A is the membrane area,

and $C_{min} = \min(C_{air}, C_{sol})$.

1.5.2 Hemingson (2005)

Based on the success of a cross-flow RAMEE simulation (Fan, 2005, and Fan et al., 2006) which showed promising effectiveness values, the first prototype of the RAMEE system was built in the Thermal Science Laboratory at the University of Saskatchewan (Hemingson, 2005). The exchanger was a cross-flow exchanger and Tyvek was used as the membrane material (Figure 1-6). The desiccant solution-flow configuration was from top-to-bottom. The prototype was not fully successful due to the deflection of the membrane (caused by the liquid pressure) which partially blocked the air-flow channels. For this reason, the prototype was only operational for low liquid pressures which restricted the flow through the exchanger and minimized the effectiveness of the exchanger.

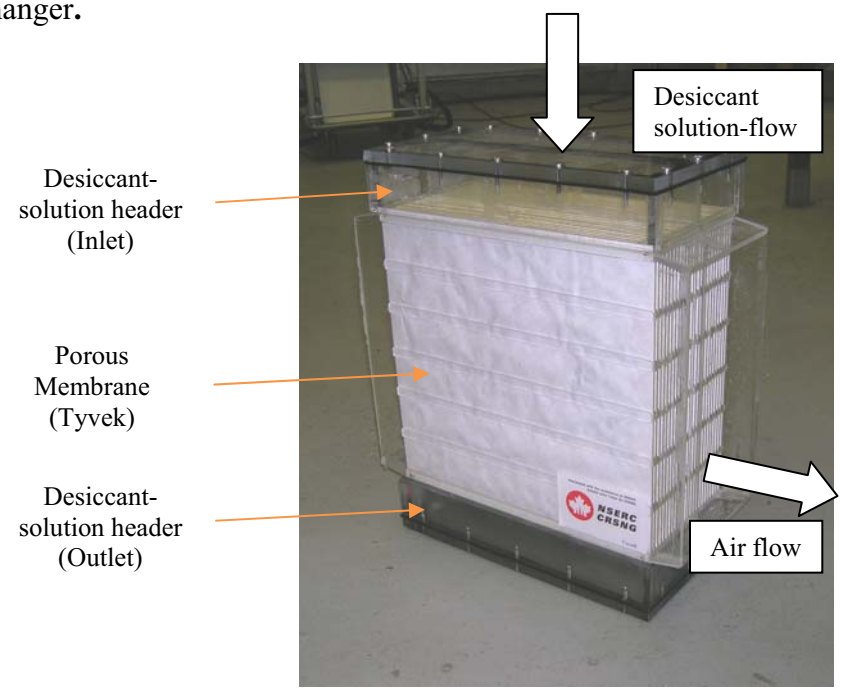

Figure 1-6. Cross-flow LAMEE to be used in a cross-flow RAMEE system developed by Hemingson (2005)

1.5.3 Larson (2006)

To address the problems faced by Hemingson (2005), Larson (2006) investigated the mechanical and moisture transfer properties of different membranes in order to select a better membrane. Larson et al. (2007) and Larson (2006) presented data on the elastic modulus, deflection, water vapor permeability, liquid penetration and cost for two membranes: Propore^{TM} and Tyvek. These data showed that Propore^{TM} is superior to Tyvek as a membrane with respect to cost, water vapor permeability, and liquid penetration pressure. Larson (2006) also investigated the deflection in a membrane by using a bulge test and reported that membrane slack greatly affected the effectiveness. He also reported that a pre-stressed membrane is less sensitive to pressure variation and should be used to reduce the effect of membrane deflection.

1.5.4 Erb (2006)

A second prototype was built and tested in the Thermal Science Laboratory at the University of Saskatchewan by Erb (2006) based on the findings of Hemmingson (2005), Larson (2006), and Fan et al. (2006). Two identical cross-flow exchangers (Figure 1-7) were built to construct a cross-flow RAMEE system and tested. The dimension of each LAMEE was 300 mm (H_{mem}) x 600 mm (L) x 100 mm (W). Each LAMEE consisted of ten liquid panels. These ten individual liquid panels introduced a modular approach to the exchanger. Each liquid panel was prepared by wrapping a plastic screen with a semi-permeable Propore^{TM} membrane (suggested by Larson, 2006) which was wrapped again with metal screens to give it rigidity. Erb (2006) reported a problem of leakage at the corner where the propore^{TM} membrane was wrapped by metal outer screen. The leakages were fixed by using plastic corner pieces which were filled with silicone (Dow Corning

732 Silicone). Aluminum was used for the outer casing to reduce the weight and machining cost of the exchanger.

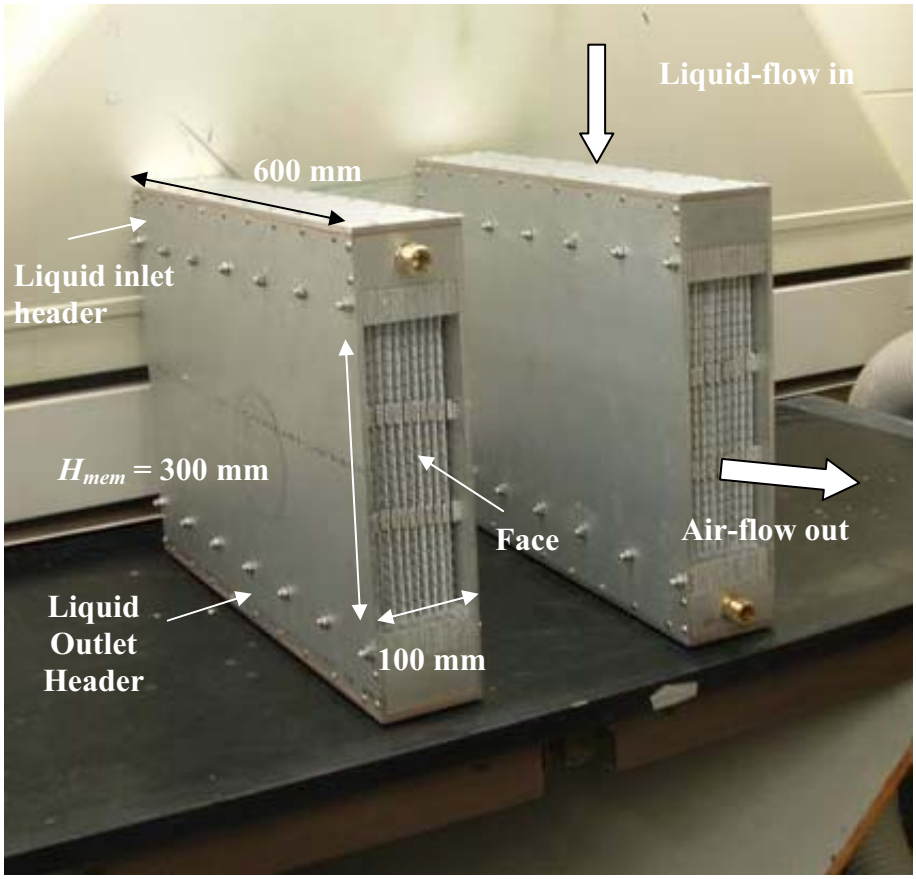

Figure 1-7. Two cross-flow LAMEEs designed and built by Erb (2006)

Tests were conducted at the standard AHRI summer and winter conditions (Table 1-2) at various NTU values and C_{sol}/C_{air} values.

Table 1-2. AHRI summer and winter operating conditions (AHRI STANDARD 1060, 2005)

	Summer	*Winter*
Supply inlet (SI_{air})	35°C Dry bulb, 26°C Wet bulb , 49% RH	1.7°C Dry bulb, 0.6°C Wet bulb 82.6% RH
Exhaust inlet (EI_{air})	24°C Dry bulb, 17°C Wet bulb, 49.5% RH	21°C Dry bulb, 14°C Wet bulb, 46% RH

The flow direction of the desiccant solution was from top-to-bottom. Erb (2006) reported a maximum effectiveness ($\varepsilon_{o,total}$) of 36% (NTU = 9.5, C_{sol}/C_{air} = 10, face velocity = 0.21 m/s, AHRI summer condition). Face velocity (V_{face}) indicates the velocity at the face of the exchanger and is determined from the conservation of mass as follows.

$$V_{face} = \frac{\dot{m}_{air}}{\rho_{air} A_{face}} \tag{1.6}$$

Af_{ace} and ρ_{air} in equation (1.6) represent face area at the inlet of the exchanger and the density of air. Larson (2006, Figure 2-16) predicted the effectiveness value of the second prototype (Erb, 2006) using Fan's (2005) model. He predicted about 25% higher than measurements values (Erb, 2006) at NTU = 4 and C_{sol}/C_{air} = 5 based on summer condition. The lower measured effectiveness was suggested to be due to non-uniform desiccant-solution flow through the LAMEE prototype. The non-uniform solution flow was caused as the inner plastic screen between the membranes was squished while fitting the whole assembly. Another reason for the non-uniform solution flow could be the bolts which went through the panel header and blocked some desiccant-solution flowing areas.

1.5.5 Erb (2007)

Erb (2007) tested again the same cross-flow RAMEE system developed in 2006 but with a different set of NTU values (2 to 11) and C_{sol}/C_{air} values (1 to 20). The flow direction of desiccant solution was reversed (from bottom-to-top rather than from top-to-bottom) to overcome some of the mal-distributed flow problems that were observed in the earlier testing (Erb, 2006). This time $\varepsilon_{o,total}$ was found to be 40% for NTU = 9.8, C_{sol}/C_{air} = 10.7 and V_{face} = 0.20 m/s. The better performance than his earlier testing (Erb, 2006) indicated that the mal-distributed flow problem was reduced with the new flow

direction. The peak effectiveness was measured to be $\varepsilon_{o,total}$ = 43%, at NTU = 11, C_{sol}/C_{air} = 20, V_{face} = 0.18 m/s and summer AHRI conditions.

1.5.6 Seyed Ahmadi (2008)

Seyed Ahmadi (2008) developed a two-dimensional numerical model to investigate the transient behavior of a cross-flow RAMEE system. The study showed that the transient response of the RAMEE system depends on the initial desiccant solution concentration, mass of the desiccant solution and heat loss/gain in between the exchangers of the solution with the surroundings. The predicted effectiveness from the numerical model was compared with the experimental data (Erb, 2007). The maximum average absolute differences between the experimental and predicted effectiveness were 7.5% and 10.3% for summer and winter operating conditions, respectively.

1.5.7 Vali (2009)

Vali (2009) developed a two-dimensional, steady-state numerical model for determining coupled heat and moisture transfer in the RAMEE system using two counter-cross-flow exchangers and with a salt solution of $MgCl_2$ as the coupling fluid. He reported that the overall effectiveness of the counter-cross-flow RAMEE system depends on the entrance ratio (the ratio of the desiccant solution entrance length to the length of the exchanger, $L_{sol,e}$ /L), aspect ratio (the ratio of the membrane surface height to the length of the exchanger, H_{mem}/L), number of heat transfer units (NTU), heat capacity rate ratio (C_{sol}/C_{air}), number of mass transfer units (NTU_m), and the mass flow rate ratio of pure salt in desiccant solution to dry air . Beside these dimensionless parameters, he also reported that, the performance of the RAMEE system is affected by the liquid-air flow configuration and the operating inlet temperature and humidity.

Vali (2009) also found that the maximum effectiveness of the RAMEE system occurs when NTU and NTU_m are large. At any NTU, the overall effectiveness of the RAMEE system increases with C_{sol}/C_{air} until it reaches a maximum value and decreases slightly after that.

1.5.8 Summary of previous RAMEE research and current research goal

Numerical simulations and experimental tests have been reported for cross-flow RAMEE systems and good agreement is found (Erb et al. 2009). However, cross-flow experimental tests results (Erb, 2006 and 2007) reported lower effectiveness values than the minimum standard effectiveness of 50% (ASHRAE Standard 90.1). In addition to that, the standard effectiveness has not been achieved at typical design velocities of HVAC components, which mostly varies from 2 m/s to 5 m/s (ASHRAE, 2005).

Numerical simulations have also been reported for a counter-cross-flow RAMEE system (Vali, 2009). However, no experimental results for counter-cross-flow RAMEE system have been reported to-date.

Based on the above previous findings, it is found that, there is a current need to design a RAMEE system to achieve standard effectiveness at the typical design velocities of the HVAC components. The effectiveness of the RAMEE system can be increased by introducing a counter-flow configuration in the two exchangers (i.e. LAMEEs) to be installed in the RAMEE system. In a counter-flow LAMEE, desiccant and air-flow headers are needed to be placed side-by-side at the inlets and outlets of the exchanger. However, the side-by-side locations of the fluid flow headers pose serious design and constructional constraints. In order to avoid the complexity of the header design and construction of a counter-flow LAMEE, a counter-cross-flow configuration with small

entrance and membrane surface aspect ratio could be used to achieve better performance than a pure cross-flow RAMEE (Vali, 2009).

Vali (2009) found that a counter-cross-flow RAMEE with an exchanger (i.e. LAMEE) entrance ratio ($L_{sol,e}$ /L) of 0.1 has a total effectiveness around 1.5% lower (at NTU = 10, C_{sol}/C_{air} = 3, H_{mem}/L = 1/5 or 0.2) compared to a counter-flow RAMEE (Vali, 2009, Figure 5-2). The Lower effectiveness in a counter-cross-flow RAMEE than a counter-flow RAMEE is due to some less active energy transfer areas at the corners of the exchanger due to lower flow rate.

Due to the close performance of a counter-cross-flow RAMEE (with small aspect and entrance ratios) in comparison to a counter-flow LAMEE, and simpler design, this M.Sc. research project will investigate the performance of a counter-cross-flow RAMEE system. The counter-cross-flow RAMEE design criterion of this study is to achieve an overall effectiveness of 65% at a typical face velocity of HVAC components. For this study face velocity of 2 m/s will be considered. The air-side pressure drop will be considered 0.5" of water ($\Delta P \leq 0.5$", 125 Pa) at 2 m/s. The air side pressure drop is based on the standard pressure drop in the residential and commercial ducting system, which varies from ±125Pa to ±2500 Pa (ASHRAE, 2004). The liquid panel design will be based on a pressurized system which can hold at least the pressure of the height of the exchanger. The above design criteria, based on current design practice, will be considered in this study to make the RAMEE system a competitive system for the commercial applications.

In addition to investigating the performance of the counter-cross-flow RAMEE system for a specific design condition, the test results will also be used to investigate any

discrepancies between the numerical model (Vali, 2009) and the measured data and to recommend improvements that should be made to the physical system and factors that should be added to the numerical model so that good agreement will result. Once this has been achieved for a wide range of test conditions further model verification tests may be unnecessary.

1.6 Objectives and constraints

The overall objectives of this research are to design a RAMEE system to achieve competitive overall effectiveness, performance testing of the designed RAMEE system and to investigate any discrepancies between the theoretical/numerical model and the measured test data. The overall objectives are divided into the following four categories.

- Design and construct two counter-cross-flow LAMEEs (having $L_{sol,e}/L < 0.1$ and $H_{mem}/L < 0.2$) and for a RAMEE system to get an overall effectiveness of 65% at face velocity of 2 m/s (400 fpm). The pressure drop inside the air channel should be less than 0.5" of water ($\Delta P \leq 0.5$" or 125 Pa) at 2 m/s. The liquid panel design will be based on a pressurized system which can hold at least the pressure of the height of the exchanger.
- To conduct tests of the developed RAMEE system at AHRI summer and AHRI winter conditions (Table 1-1) for various NTU and C_{sol}/C_{air} values.
- Analyze the steady-state and transient experimental data and their uncertainties.
- Compare the counter-cross-flow RAMEE results with simulated (Vali, 2009) and experimental results (Erb, 2007; Erb et al., 2009).

1.7 Thesis overview

The counter-cross-flow RAMEE system design and construction are described in Chapter 2. The LAMEE design is based on the effectiveness-NTU correlation for a counter-flow flat plate heat exchanger.

In Chapter 3, the test facility used for testing the counter-cross-flow RAMEE system is presented. The sensors used to measure the various air and desiccant solution properties required to determine the RAMEE performance and uncertainty are also described.

Experimental test results and analysis for the designed and built counter-cross-flow RAMEE system are presented in Chapter 4.

In Chapter 5 the experimental data are compared with numerical data (Vali, 2009) and experimental data for a cross-flow RAMEE (Erb, 2007).

Finally, Chapter 6 presents the conclusions based on the findings in this thesis. Recommendations for future RAMEE studies are also described in Chapter 6.

CHAPTER 2
COUNTER-CROSS-FLOW RAMEE SYSTEM DESIGN AND CONSTRUCTION

2.1 Introduction

This chapter describes the design of a counter-cross-flow RAMEE system which includes the design of two counter-cross-flow LAMEEs. As described in Chapter 1, the design criterion of the LAMEEs in this study is to achieve an overall effectiveness of 65% at a face velocity (V_{face}) of 2 m/s (400 fpm). This design objective is not an optimized design; rather it is a practical design goal. That is, the counter-cross-flow RAMEE system should meet the design goals without considering mechanical design factors, including the elasticity and deflection of the construction materials of the exchanger.

The desiccant solution and air-flow loop in the RAMEE system is not involved in the design process. These two loops are part of the test facility (Chapter 3) where the LAMEEs are installed to make a counter-cross-flow RAMEE system. After designing the LAMEE, the construction of the LAMEEs is also described in this chapter.

2.2 LAMEE design

The LAMEE design, proposed in this thesis based on counter-cross-flow design approach (Chapter 1). Figure 2-1 shows a schematic of a current LAMEE design. In the current design a membrane surface aspect ratio (H_{mem}/L) of 1/9 and an entrance ratio ($L_{sol,e}/L$) of 1/24 are considered which gives a very close (i.e. less than 1.5%) total effectiveness in comparison to true counter-flow effectiveness (Vali, 2009, Figure 5-1).

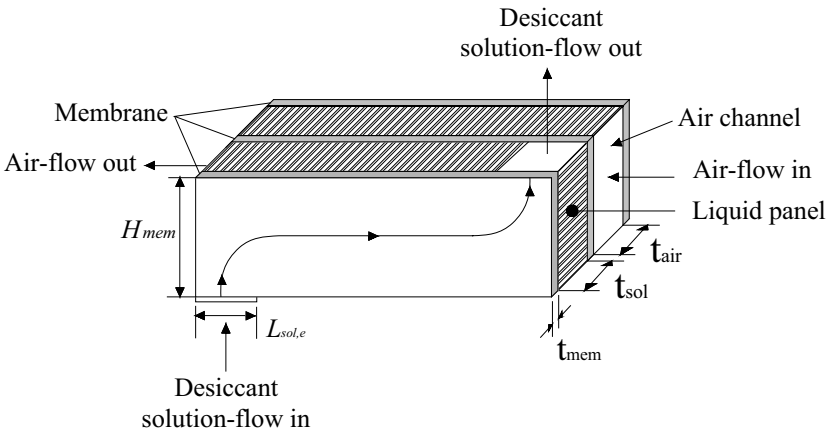

Figure 2-1. Schematic of a counter-cross-flow LAMEE

The LAMEE design process consists of liquid panel design, air channel design and desiccant solution selection. Each liquid panel holds two semi-permeable membranes whereas each air channel allows air to flow over the liquid panel. In the present LAMEE design, 10 liquid panels and 11 air channels are placed side by side as shown in Figure 2-1. The selection of the number of liquid panels is based on the study of Seyed Ahmadi (2008). He showed that for NTU = 5 and $C_{sol}/C_{air} = 3$, if the number of liquid panels of a cross flow exchanger was increased from 10 to 50, the overall total effectiveness ($\varepsilon_{o,total}$) increased less than 1%, which is not significant (Seyed Ahmadi , 2008, Figure 2-12).

Selection of a desiccant solution is also the part of the LAMEE design process which will be described in the next section. After that, liquid panel and air channel design will be addressed.

2.2.1 Desiccant solution selection

Desiccant solutions absorb or desorb moisture or water vapor from the air stream inside a LAMEE depending on the vapor pressure difference between the air stream and

desiccant solution. The vapor pressure of a desiccant solution is inversely proportional to its concentration and directly proportional to its temperature (ASHRAE, 2005).

There are many desiccant solutions available, which are suitable for transferring heat and moisture between the supply LAMEE and the exhaust LAMEE. These include solutions of lithium bromide, lithium chloride, calcium chloride, and magnesium chloride. In the present counter-cross-flow RAMEE design, the magnesium chloride ($MgCl_2$) solution is chosen due to its low cost and availability compared to the other desiccant solutions. A suitable desiccant solution will be one which can operate (i.e. absorb and desorb moisture) at the operating weather conditions without crystallization (Erb et al., 2009).

Operation of a desiccant solution can be illustrated by plotting the humidity ratio that exists for air in equilibrium with the desiccant solution at different concentrations on the psychrometric chart (Figure 2-2), where the desiccant solution concentration (Cn_{sol}) is defined as,

$$Cn_{sol} = \frac{\text{mass of desiccant}}{\text{mass of desiccant} + \text{mass of water}}. \tag{2.1}$$

The humidity ratio of air (W_{air}) at equilibrium is determined using the correlations developed by Cisternas and Lam (1991), where Cn_{sol} = 35.9% corresponds to the saturation condition of the desiccant solution where the correlation has more uncertainty.

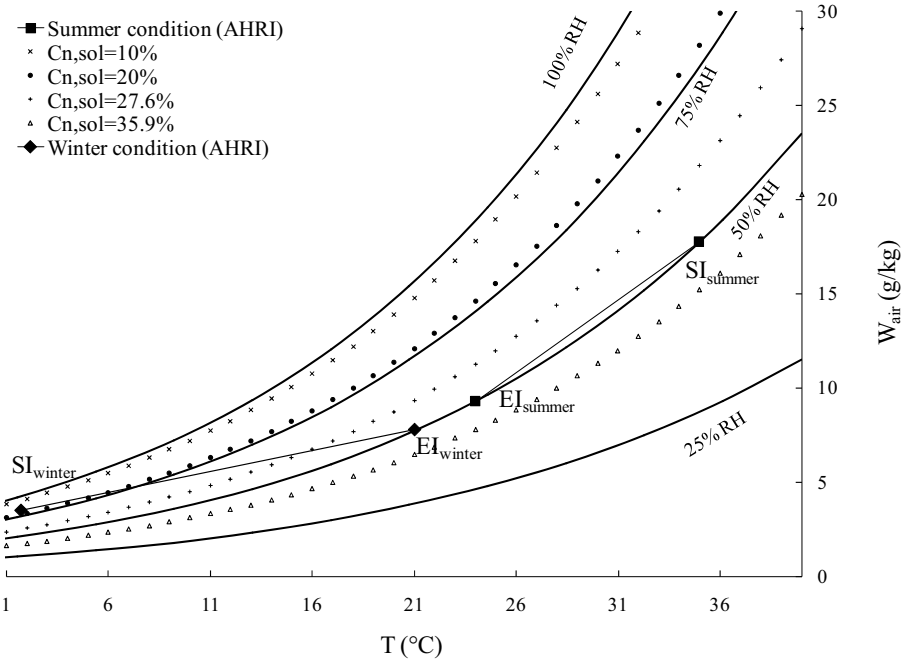

Figure 2-2. Humidity ratio of air in equilibrium with aqueous magnesium-chloride ($MgCl_2$) at different concentrations superimposed on the psychrometric chart (Erb et al., 2009) showing AHRI summer and winter operating conditions for the RAMEE system

The AHRI summer and winter operating conditions in the psychrometric chart of Figure 2-2 indicate air-flow properties at the LAMEE inlets. The same conditions in the plot then also indicate the corresponding concentration of $MgCl_2$ solution in the LAMEEs. The working principle of the $MgCl_2$ desiccant solution is described below using the summer operating condition.

The supply air conditions for the AHRI summer test condition is noted by the point SI_{summer} (35°C and 50% RH). The conditions of the exhaust air from the space are noted by the point EI_{summer} (24°C and 50.5% RH). Point SI_{ummer} indicates a concentration of 32.5% for the desiccant solution in the supply LAMEE (air entering the building), whereas point EI_{summer} indicates a concentration of 32% for the desiccant in the exhaust LAMEE (air leaving the building). When the desiccant solution travels through the

supply LAMEE, it dehumidifies the supply air by absorbing water vapor from the air. As a result, the concentration of the desiccant solution is decreased at the supply LAMEE. The desiccant solution then flows through the pump and solution flow loop and passes through the exhaust LAMEE, where it humidifies the exhaust air stream by evaporating the dissolved water. As a result, concentration of the liquid desiccant solution is increased in the exhaust LAMEE. With time, the desiccant solution reaches a quasi-steady concentration between the supply (32.5%) and exhaust (32%) equilibrium concentrations.

Figure 2-2 also shows that the saturation concentration of $MgCl_2$ is 35.9%. Saturation concentration indicates the maximum allowable desiccant solution concentration in the RAMEE system as crystallization of the desiccant begins at this concentration. Crystallization in the RAMEE system can cause many problems like blockage of solution-flow gap, membrane blocking and pumping. Charles and Johnson (2008) and Seyed Ahmadi (2008) reported that crystallization could also decrease heat and moisture transfer performance of the semi-permeable membrane. It is recommended not to operate the RAMEE system close to the saturation limit of desiccant solution. An alternative desiccant solution should be chosen for the dry operating conditions that cause the solution to approach saturation. The present RAMEE system is tested at the AHRI summer and winter operating conditions which are safely away from the desiccant saturation limit as indicated in Figure 2-2. The $MgCl_2$ solution is thus a suitable choice for the current RAMEE system. Investigations with different desiccant solutions in the RAMEE system are left for future study.

2.2.2 Liquid panel and air channel design

A liquid panel is constructed with two membranes, an inner screen, corrugated plastic, air and liquid spacers and an outer screen. Figure 2-3 (a) shows the three-

dimensional (3D) view and Figure 2-3 (b) shows the cross-sectional front-view of a liquid panel. Only the air spacer dimension is specified in the figure because the heat and moisture transfer area and air and solution flow gaps will be determined in section 2.3 on exchanger sizing. Figure 2-4 shows the inside design of the liquid panel. Corrugated plastic is used for entering and leaving the liquid from the liquid panels. Inner screens are inserted in between two membranes to prevent the membrane walls from collapsing inside and blocking the liquid panel. Air spacers are used for creating an air-flow gap over the liquid panel. A liquid spacer (Figure 2-4) having similar thickness of the liquid flowing gap is used at the four edges of the liquid panel to seal the panel edges and to provide a constant gap for solution-flow. The outer screen is used to reduce the membrane deflection. Machine grooves (Figure 2-3b) along the length of air spacers secure the edges of outer screens firmly.

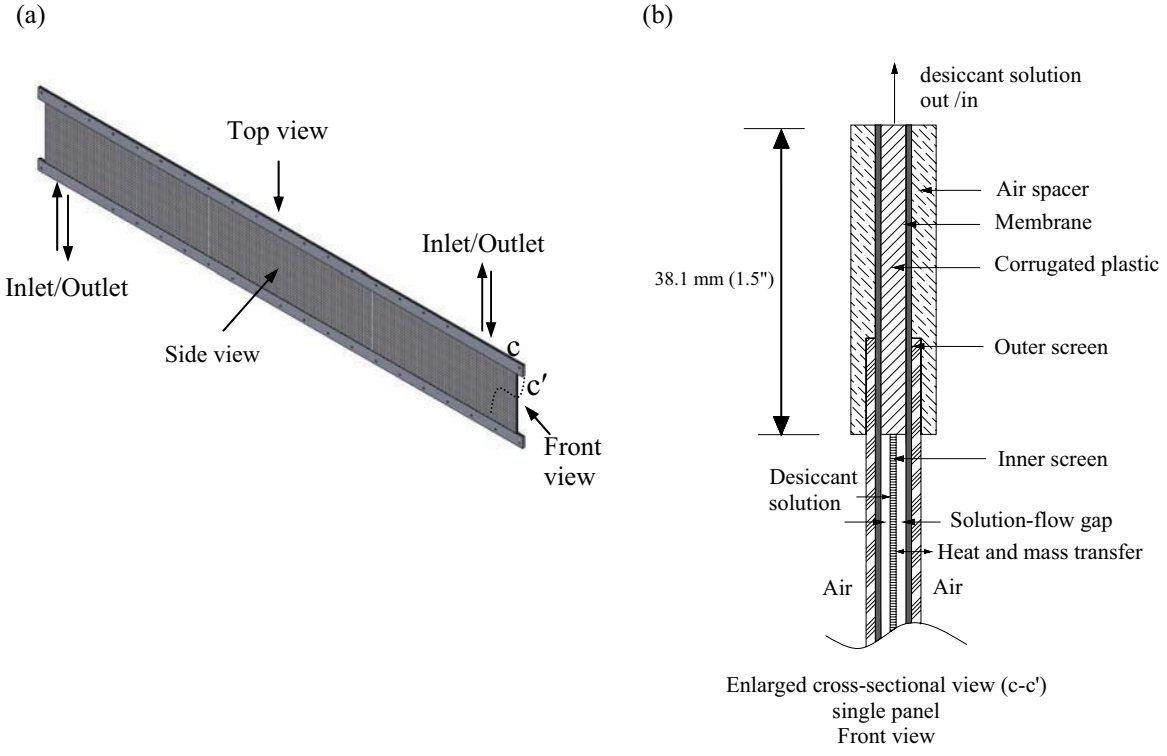

Figure 2-3. a) 3D-view and b) cross-sectional front view of a liquid panel

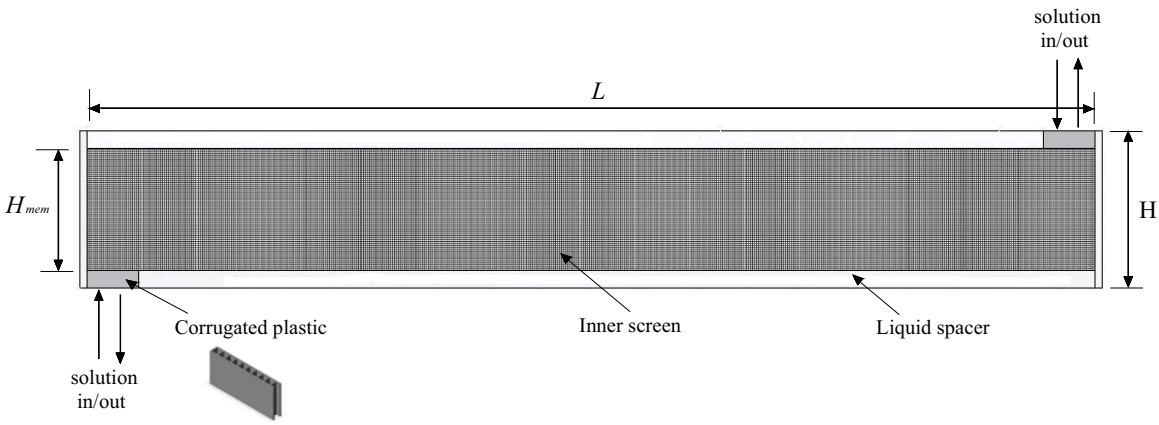

Figure 2-4. Inside liquid panel construction used in the LAMEE design (side view)

Two liquid panels separated by round spacers and air spacers are placed side-by-side to create the air-flow channel (Figure 2-5a). When desiccant solution flows inside the liquid panels, the membranes deflect into the airflow channels because of a pressure difference between the liquid panel and air channel (Figure 2-5b). The outer screen may also deflect along with the membrane.

Due to membrane and outer screen deflection, the solution-flow gap (t_{sol}) increases. The increased solution-flow gap is represented by average solution-flow gap ($t_{sol,avg}$). The air-flow gap also increases due to spaces occupied by the outer screen and is indicated as $t_{air,avg}$ (Figure 2-5b).

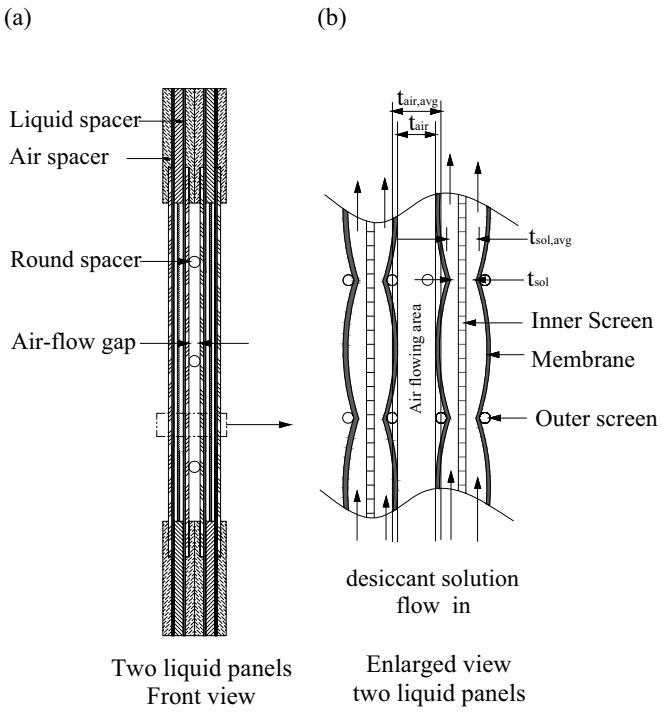

Figure 2-5. a) Air-flow channel and b) membrane deflection through the outer screen opening inside liquid panels

To design the liquid panel and air channel, the following information is required.

- Sizing of the liquid panel. The sizing of the liquid panel depends on the sizing of the LAMEE membrane surface area (H_{mem} *x L*), is based on the membrane area required to achieve 65% overall effectiveness.
- Materials need to be selected for air and liquid spacers, corrugated plastic, and the inner and outer screens. A suitable membrane also needs to be selected.
- The average solution and air-flow gap ($t_{sol,avg}$, $t_{air,avg}$) also needs to be determined. The values of $t_{sol,avg}$ and $t_{air,avg}$ depend on the allowable pressure drop across the exchanger, the selection of t_{sol} and t_{air} and the deflection of membrane and outer screen. The value of t_{air} is equal to the thickness of the

round spacer (Figure 2-5a) and t_{sol} is equal to the thickness of the liquid spacer.

The following sections describe material and membrane selection, membrane area estimation, and liquid panel and LAMEE construction.

2.2.3 Materials and membrane selection

Acrylic round bars inserted in between two membranes in the air-flow gap in Figure 2-5. Coroplast™ is used as a corrugated plastic in Figure 2-4 and Delrin is used for the spacers in Figure 2-3. Delrin is chemically known as Polyoxymethylene. Delrin is similar to nylon, but stiffer, and has better fatigue and water resistance (CES Edu Pack, 2007). Fiber glass (0.77 mm thickness) screen is used as the inner screen.

For the current liquid panel design, the membrane is selected based on the study of Larson (2006). As described in Chapter 1, Larson (2006) reported that the polypropylene Propore™ membrane is superior to Tyvek. The same Propore™ membrane is chosen as the membrane material in the current LAMEE design and its properties are given in Table 2-1. Propore™ membrane is formed by thermally laminating a non-woven polypropylene fabric with microporous poly-propylene (PP) membrane. The non-woven fabric provides support to the highly elastic polypropylene membrane. Figure 2-6 shows an atomic force microscope image of the microstructure of the Propore™ membrane on the microporous polypropylene face (Larson, 2006).

Table 2-1. Properties of Propore™ membrane

Parameters	*Values*	*Comments*
Membrane thickness (t_{mem})	0.2 mm	Mike Larson (2007)
Membrane thermal conductivity (k_{mem})	0.334 W/m	Mike Larson (2007)
Membrane permeability (K_m)	16.6 x 10-7(kg/m.s)	Mike Larson (2007)

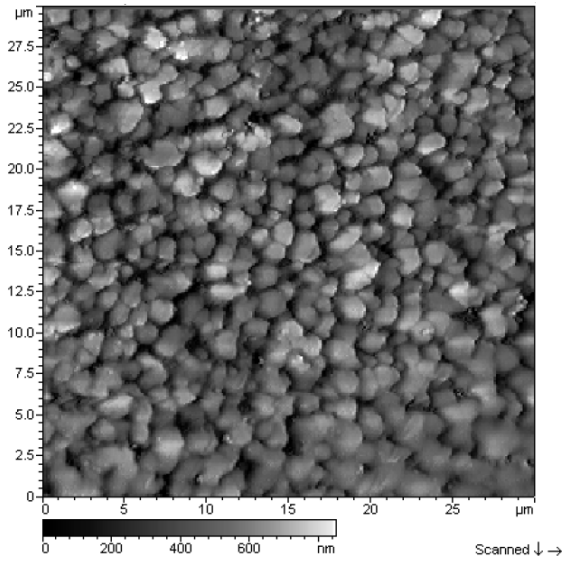

Figure 2-6. Microscope image of the polypropylene Propore^{TM} membrane (Larson, 2006)

The outer screen for the current panel design is also selected based on the study of Larson (2006). Larson (2006) investigated the Propore^{TM} membrane deflections using different outer screen sizes. He reported that for an outer screen (1.77 mm thickness) having the mesh size of 12.7 mm x 12.7 mm, pre-stressed (1230 kPa) Propore^{TM} membrane will deflect 1 mm at a pressure of 20 kPa (around 90 inches of water).

2.2.4 Membrane area estimation

An important step in designing a LAMEE is to estimate the membrane surface area which will be used to transfer heat and moisture between the air and desiccant solution based on the industry recommended effectiveness value. Therefore an effectiveness correlation which is based on heat and moisture is required for estimating membrane area. However, no heat and moisture transfer based effectiveness correlation is available to date for LAMEE or any similar exchangers. Due to this, a heat transfer based effectiveness correlation for flat-plate heat exchangers is used in this study. Recently a

heat transfer based correlation for a LAMEE has been developed (Vali, 2009) which was not available at the time of LAMEE design. Heat transfer based effectiveness correlation is known as the effectiveness-NTU method in the literature. Apart from the correlation, both heat and moisture transfer effects could be included in the design if a simulation program is used. However, a program was not available when the LAMEE system was designed. In the following sections both the effectiveness-NTU method (heat transfer only) and a simulation method for estimating membrane area are described.

2.2.4.1 Membrane area estimation based on heat transfer

The effectiveness of a heat exchanger depends on the number of transfer units (NTU), the heat capacity ratio of the two fluids (C_r) and the flow consideration as shown below (Incropera and Dewitt, 2002),

$$\varepsilon = f(\text{NTU}, C_r, \text{flow arrangement}) . \tag{2.2}$$

For sensible heat transfer the number of transfer units (NTU), can be defined for each exchanger of the RAMEE system by equation (2.3) and C_r can be expressed by equation (2.4) as follows.

$$\text{NTU} = \frac{UA}{C_{min}} \tag{2.3}$$

$$C_r = \frac{C_{min}}{C_{max}} = \frac{(\dot{m}c_p)_{min}}{(\dot{m}c_p)_{max}} \tag{2.4}$$

In equation (2.3), U is the overall heat transfer coefficient (W/m^2K) and A is the membrane surface area of the exchanger (m^2). In equation (2.4), c_p is the specific heat capacity and $\dot{m}$ is the mass flow rate of the fluid.

Different correlations are available for different flow configurations and types of exchanger. The LAMEE proposed in this thesis is similar to a counter-flow flat plate exchanger, where

$$\varepsilon_{\text{sensible (s) or (e)}} = \frac{1-\exp[-\text{NTU}(1-C_r)]}{1-C_r\exp[-\text{NTU}(1-C_r)]} \quad , C_r < 1 \tag{2.5}$$

$$\varepsilon_{\text{sensible (s) or (e)}} = \frac{\text{NTU}}{\text{NTU}+1} \quad , C_r = 1 \tag{2.6}$$

Since the target effectiveness is based on the overall effectiveness of the RAMEE system, a relationship between the effectiveness of a LAMEE and the overall effectiveness needs to be defined. Zeng (1990) reported that when the heat capacity ratio and number of transfer units of both the supply and exhaust exchanger were equal, i.e. $C_{r,(s)} = C_{r,(e)}$, $\text{NTU}_{(s)} = \text{NTU}_{(e)}$,the overall sensible effectiveness of the RAMEE system could be defined as

$$\frac{1}{\varepsilon_{o,\text{sensible}}} = \frac{1}{\varepsilon_{\text{sensible},(s)}} + \frac{1}{\varepsilon_{\text{sensible},(e)}} - C_r \qquad \text{for } C_{air} \le C_{sol} \tag{2.7}$$

$$\frac{1}{\varepsilon_{o,\text{sensible}}} = \frac{1}{C_r}\left(\frac{1}{\varepsilon_{\text{sensible},(s)}} + \frac{1}{\varepsilon_{\text{sensible},(e)}} - 1\right) \qquad \text{for } C_{air} > C_{sol} \tag{2.8}$$

The required NTU and C_r of the LAMEE to achieve a 65% overall sensible effectiveness of the RAMEE system can be determined, using equations (2.5) to (2.8). Figure 2-9 represents equations (2.5 to 2.8) graphically where $\varepsilon_{o,\text{sensible}}$ is shown as a function of C_{sol}/C_{air} and NTU. As shown, $\varepsilon_{o,\text{sensible}}$ increases and peaks at $C_{sol}/C_{air} = 1$. It can be observed from equations (2.6 and 2.7) that at NTU = 4 the overall RAMEE system effectiveness reaches approximately 0.65 for $C_{sol}/C_{air} = 1$. NTU = 4 and $C_{sol}/C_{air} = 1$ could then be used to estimate membrane area. However, a value of NTU = 4.5 and $C_{sol}/C_{air} = 1$

is chosen for this design to have a factor of safety. With these values the heat transfer area of the exchanger can be calculated using equation (2.3)

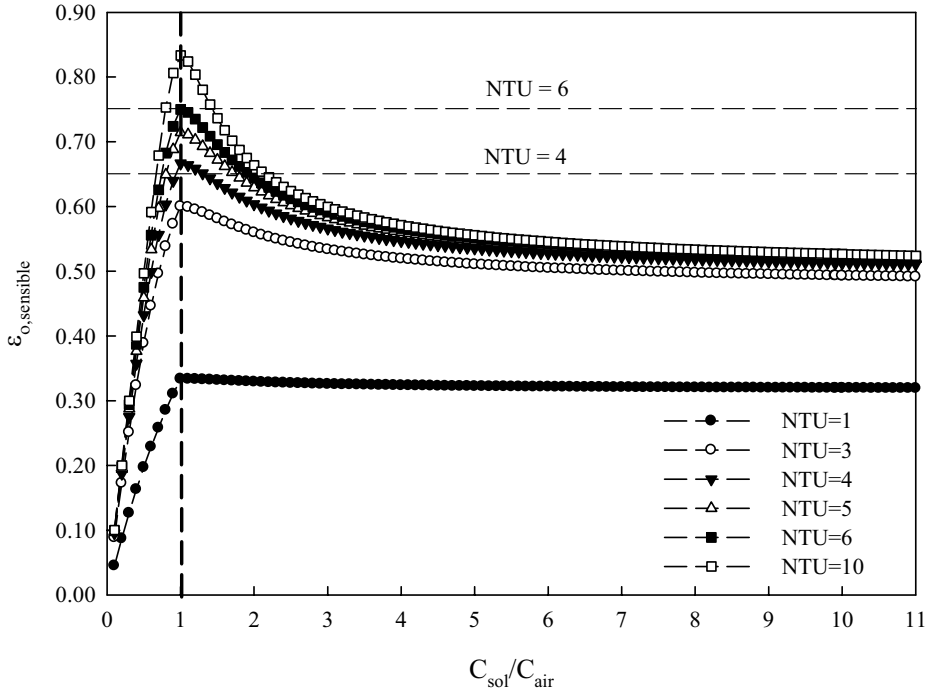

Figure 2-7. Variations of the overall sensible effectiveness of a counter-cross-flow RAMEE as a function of C_{sol}/C_{air} with NTU as a parameter

2.2.4.1.1 Overall heat transfer coefficient

The overall heat transfer coefficient (U) is the thermal conductance between the two fluid streams. The product of U and the heat transfer area (A) is the inverse of the total resistance between the two fluid streams as shown below.

$$R_{tot} = \frac{1}{UA} \tag{2.9}$$

The total thermal resistance (R_{tot}) includes the conduction and convection resistances of the fluid streams, membrane separating the fluid streams. In a general exchanger, the

effects of fouling and finned surfaces may be included as follows (Incropera and Dewitt, 2002)

$$R_{total} = \frac{1}{UA} = \frac{1}{(\eta_o hA)_{cold}} + \frac{R''_{f.cold}}{(\eta_o A)_{cold}} + R_w + \frac{R''_{f.hot}}{(\eta_o A)_{hot}} + \frac{1}{(\eta_o hA)_{hot}} \quad (2.10)$$

Here, subscripts cold and hot denote the cold and hot fluids, respectively. R_f'' is the fouling factor, η_o is the overall surface efficiency of the fin, R_w is the resistance of the separating materials and *h* is the convective heat transfer coefficient.

For a LAMEE, designed with flat membranes (i.e. no finned surfaces) and neglecting fouling factor, the overall heat transfer coefficient can be written as follows,

$$U = \left[\frac{1}{h_{sol}} + \frac{t_{mem}}{k_{mem}} + \frac{1}{h_{air}} \right]^{-1} \quad (2.11)$$

where, h_{sol} is the convective heat transfer coefficient of desiccant solution, h_{air} is the convective heat transfer coefficient of air stream, t_{mem} is the thickness of the membrane and k_{mem} is the thermal conductivity of the membrane. In the equation (t_{mem}/k_{mem}) is then the thermal resistance of the membrane. For this design k_{mem} = 0.334 W/ (m.K) and t_{mem} = 0.2 mm are adopted as reported by Larson (2006) for Propore™ membrane. Decreasing the value of membrane resistance increases the overall heat transfer coefficient, which improves the exchanger effectiveness values and the heat transfer rates between the two fluid flows.

2.2.4.1.2 Convective heat transfer coefficient

Convective heat transfer coefficients (h_{sol}, h_{air}) are required to calculate the overall heat transfer coefficient in equation (2.11). The convective heat transfer coefficient for fully developed laminar flow ($Re \leq 2300$) in the liquid panel and air channel (i.e. liquid

and air-flow gap) can be determined from the dimensionless heat transfer coefficient, Nusselt number (Nu),

$$\mathrm{Nu} = \text{constant} = \frac{h\mathrm{D_h}}{\mathrm{k}} \tag{2.12}$$

where $\mathrm{D_h}$ is the hydraulic diameter of the air-flow channel or solution-flow panel. In designing the exchanger, Nu = 8.24 (Kays and Crawford, 1984, page 103) is used to estimate the convective heat transfer coefficient. The value of Nu = 8.24 is based on the fully developed flow between two infinite parallel plates with a uniform surface heat flux. The Hydraulic diameter in equation (2.12) is calculated from the following equation.

$$\mathrm{D_h} = \frac{4\ \text{Area}}{\text{Perimeter}} \tag{2.13}$$

For the present LAMEE design, a very large membrane height (H_{mem}) compared to the air or liquid flow gap (t_{sol}, t_{air}) is considered. Therefore, the hydraulic diameter of the liquid panel is twice the average solution-flow gap for the LAMEE.

$$\mathrm{D_{h,sol}} = \lim_{H_{mem}\to\infty} \frac{4\mathrm{t_{sol,avg}} H_{mem}}{2(\mathrm{t_{sol,avg}} + H_{mem})} = 2\mathrm{t_{sol,avg}} \tag{2.14}$$

Similarly, the hydraulic diameter of the air channel can be calculated using equation (2.15) as follows.

$$\mathrm{D_{h,air}} = \lim_{H_{mem}\to\infty} \frac{4\mathrm{t_{air,avg}} H_{mem}}{2(\mathrm{t_{air,avg}} + H_{mem})} = 2\mathrm{t_{air,avg}} \tag{2.15}$$

2.2.4.1.3 Minimum heat capacity rates (C_{min})

As shown in Figure 2-7, the heat capacity rates of the air and the solution in a LAMEE (sensible design only) should be equal (C_r = 1) in order to achieve the highest sensible effectiveness for a given NTU. In this design, C_{air} ($C_{air} = \dot{m}_{air} c_{p,air}$) is determined

based on the design targets specified by industry and C_{sol} will be adjusted to give optimal performance.

The $\dot{m}_{air}$ to determine C_{air} is calculated from the design target to get a face velocity (V_{face}) of 2 m/s, where the face velocity is determined from the conservation of mass as follows,

$$\dot{m}_{air} = V_{face}\rho_{air}A_{face} \tag{2.16}$$

The face area (A_{face}) is the total cross-sectional area of the LAMEE that is exposed to the air-flow and is calculated as follows,

$$A_{face} = H\left[\left(t_{sol} + 2t_{mem} + 2t_{o.screen}\right)n_{sol} + n_{air}t_{air}\right] \tag{2.17}$$

where, $t_{o.screen}$ is the thickness of the outer screen, n_{sol} is the number of liquid panels, and n_{air} is the number of air channels.

If the numbers of liquid panels are increased, the face area will be increased. According to equation (2.16), the air-flow rate ($\dot{m}_{air}$) must then be increased to maintain a constant face velocity (V_{face}). More fan power is needed to maintain the face velocity of 2 m/s with higher number of liquid panels, consequently.

2.2.4.2 Membrane area estimation based on numerical simulation

Section 2.2.4 describes the LAMEE design based on the heat transfer correlations alone as no experimental or analytical heat and mass transfer correlations are available to date to guide the present design. Another way to design the exchanger is to use the numerical simulation model based on the heat and moisture transfer. A numerical model on a similar system was developed by Vali (2009). Design NTU values can be predicted from his model based on the target effectiveness of 0.65 of the RAMEE system. The

required membrane area can then be estimated from the predicted NTU using both the heat and mass transfer units as follows.

$$NTU_m = \left\{ \frac{U_m A}{\dot{m}_{min}} \right\} \tag{2.18}$$

$$NTU = \left(\frac{UA}{C_{min}} \right) \tag{2.19}$$

Here, U_m is the overall mass transfer coefficient (W/m^2K) and A is the membrane surface area of each exchanger (m^2). The overall mass transfer coefficient (U_m) can be calculated using the following equation,

$$U_m = \left[\frac{1}{h_{m,sol}} + \frac{t_{mem}}{k_{mem}} + \frac{1}{h_{m,air}} \right]^{-1} \tag{2.20}$$

where, $h_{m,sol}$ and $h_{m,air}$ are the convective mass transfer coefficients of the liquid desiccant and air stream, respectively. These coefficients can be calculated using the equation based on the Chilton-Colburn analogy (Seyed Ahmadi, 2008).

$$h_m = \frac{h}{c_p} Le^{-2/3} \tag{2.21}$$

The maximum estimated heat or mass transfer area using the equations (2.18) and (2.19) could also be used in designing the exchanger. Air and liquid flow gaps can be adjusted based on the design constraints.

2.2.5 Estimation of $t_{sol,avg}$ and $t_{air,avg}$

To estimate $t_{sol,avg}$ and $t_{air,avg}$ the volume of a small segment of the liquid panel and adjacent air channel is considered .Figure 2-8 shows the smallest segment adjacent to the liquid panel and air channel.

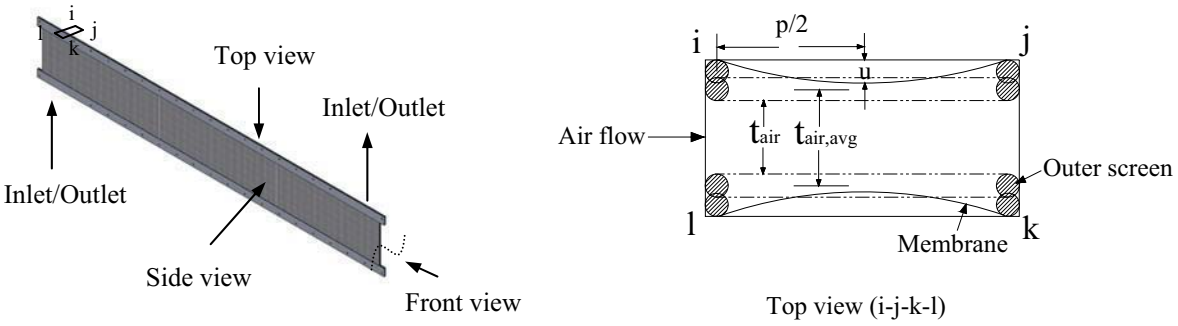

Figure 2-8. Smallest segment adjacent to the liquid panel showing average air-flow gap ($t_{air,avg}$) and constant air-flow gap (t_{air})

The average air and solution-flow gap is calculated by calculating the volume of the small segment, membrane and outer screen deflection shown in the following equations (2.22 to 2.24). Membrane deflection is assumed spherical and is calculated using equation (2.24) (Avallone, E.A. and Baumeister, T., 1996). Volume of outer screen deflection is assumed parabolic.

$$t_{air,avg} = \frac{\text{Volume}(\text{block}_{ijkl} - \text{mem}_{deflection} - \text{o.screen}_{deflection} - \text{o.screen} - \text{round spacer})}{H_{mem} \times p} \quad (2.22)$$

$$t_{sol,avg} = t_{sol} + \frac{\text{Volume}(\text{mem}_{deflection})}{H_{mem} \times p} \quad (2.23)$$

$$\text{Volume}\left(\text{mem}_{deflection}\right) = \frac{1}{6}\pi h\left(3p^2 + u^2\right) \quad (2.24)$$

Membrane deflection is considered 1 mm which is reported by Larson (2006) at 20 kPa (80 inch of water) and the specific outer screen used in this design. As a result the worst-case operating liquid pressure for this current design is 20 kPa. Outer screen deflection of 1 mm at the maximum between two round spacers is assumed inside the solution-flow gap. This may be checked in future research.

Selection of $t_{sol,avg}$ and $t_{air,avg}$ is constrained by the industry set standard of pressure drop across the exchanger (i.e. ΔP across the exchanger is less than 0.5 inch of water). Pressure drop across an exchanger can be calculated using the following equation.

$$\Delta P = \rho g h_f \tag{2.25}$$

where, h_f is the head loss due to friction inside the exchanger. The friction head loss can be predicted for both laminar and turbulent flow using Darcy-Weisbach equation (White, 2005)

$$h_f = f \frac{L}{2t_{air,avg}} \frac{V_{in}^2}{2g} \tag{2.26}$$

where, f is the duct friction factor, L is the exchanger length, $t_{air,avg}$ is the average solution-flow gap of the liquid panel, and V_{in} is the average velocity of air inside the exchanger. The equation (2.26) can be modified by introducing the friction coefficient, C_f, where $(C_f = \frac{f}{4})$, and hydraulic diameter, D_h .Therefore, the final form of the pressure drop equation becomes

$$\Delta P/L = \frac{4}{2t_{air,avg}} \left(\frac{1}{2} \rho V_{in}^2 \right) C_f \tag{2.27}$$

Equation (2.27) is used to calculate the pressure drop across the exchangers in the RAMEE system. The friction coefficient (C_f) depends on the Reynolds number (Re) and roughness of the duct. The value of the C_f can be determined from the correlations available in the literature. In designing the present LAMEE, equation (2.28) by Shah and London (1979, page 386) is used to determine C_f, where the exchanger length is assumed infinite.

$$C_f \, Re = 24 \tag{2.28}$$

V_{in} in equation (2.27) is calculated by using the ratio of face area (A_{face}) to inside air-flow area. Due to reduced flow area inside the air-flow gap caused by the membrane deflection, the air velocity inside the exchanger is higher than the face velocity. Based on the continuity equation, V_{in} is calculated by using the ratio of face area to inside air-flow area in equation (2.29) below.

$$V_{in} = \frac{A_{face}}{A_{in}} \times V_{face} \tag{2.29}$$

V_{in} is also used to determine the Reynolds number (equation 2.30) inside the exchanger to predict the flow behavior. A_{in} is determined using equation (2.31).

$$Re = \frac{\rho V_{in} D_h}{\mu} \tag{2.30}$$

$$A_{in} = H_{mem}\left[n_{air} t_{air}\right] \tag{2.31}$$

2.3 Exchanger sizing

A spreadsheet was developed based on the design equations, correlations, constraints and goals for sizing the exchanger for heat transfer only. Exchanger sizing is largely dependent on the solution gap (t_{sol}) and air-flow (t_{air}) gap. A thin air-flow gap and solution-flow gap increases the overall heat transfer coefficient and as a result decreases the size of the exchanger. On the other side, a thick air and solution-flow gap decreases the overall heat transfer coefficient which results in a bigger exchanger to achieve the desired effectiveness. For the current design, a minimum solution-flow gap can be considered as the thickness of the inner screen (0.7 mm). However, to reduce the non-uniformity of solution-flow inside the liquid panel, a t_{sol} of 1.5 mm is considered. Further increasing the solution-flow gap increases the size of the exchanger. To increase the

average U, the end channels on two sides of the exchanger are made with half the air-flow gap (0.5 t_{air}).

Different case studies are carried out to determine the membrane surface area by varying air-flow gap (t_{air}). The membrane area for a single liquid panel is estimated using equation (2.3). The heat transfer coefficient h_{air}, h_{sol} and U are calculated from equations (2.11) and (2.12). $t_{sol,avg}$ and $t_{sol,avg}$ are estimated using equations (2.22), (2.23) and (2.24). Desiccant solution properties (C_{sol} and k_{sol}) are calculated using correlations reported by Zaytsev and Aseyev (1992) in Appendix-A. Table 2-2 shows the LAMEE specifications based on the spreadsheet. Table 2-2 shows that exchanger sizing increases with increasing air-flow gap. Case-study 2 is considered in this design to reduce the risk of blockage in the air-flow gap due to membrane deflection and to reduce the size of the exchanger. The length of the exchanger is considered to the nearest round figure (1800 mm). The height of the exchanger will be the membrane height (H_{mem}) plus the height of the air spacer ($2 \times 1.5"$, Figure 2-3b).

Table 2-2. LAMEE design case-study

Parameters	*Case study-1*	*Case study-2*	*Case study-3*
Air-flow gap (mm), t_{air}	2	3.18	4
Solution-flow gap (mm), t_{sol}		1.5	
Number of liquid panels		10	
Average air-flow gap (mm), $t_{air,avg}$	3.3	4.4	5.2
Average solution-flow gap (mm), $t_{sol,avg}$	2.7	2.7	2.7
ΔP (across exchanger) Pa	110	80	69
Reynolds number, Re	1768	2047	2243
Propore™ thickness (mm)		0.2 (Larson , 2006)	
NTU		4.5	
C_{sol}/C_{air}		1	
$\dot{m}_{air}$ (kg/s)	0.022	0.038	0.053
$\dot{m}_{sol}$ (kg/s)	0.001	0.002	0.002
Membrane surface aspect ratio (H_{mem}/L)		1:9	
Membrane area (mm) Lx H_{mem}	1159 x 130	1775 x 200	2278 x 250
LAMEE sizing (mm) L x Hx W^1	1159 x 206 x 74	1775 x 276 x 86	2278 x 326 x 94

[1]*This is the width of the liquid panels and air channel. The thickness of the exchanger outer casing needs to be added to get the exchanger width.*

2.4 Liquid panel and LAMEE construction

A die consisting of two aluminum boxes and a block is used for panel construction. The aluminum block is made of the size of the membrane area of the exchanger (1800×200 mm or $70.87" \times 10.87"$). The aluminum box is made 3.18 mm (1/8 inch) bigger than the block so that it can slide over the block. Figure 2-9 shows the aluminum block and box.

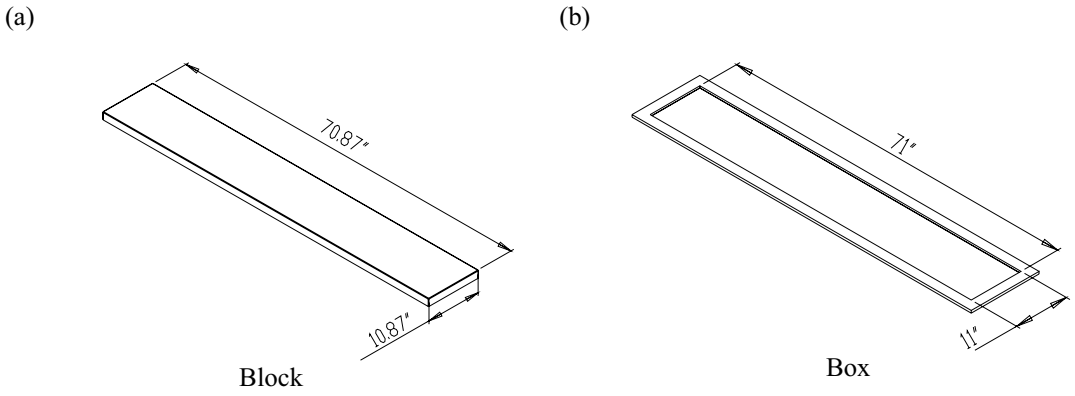

Figure 2-9. (a) Block and (b) box die for liquid panel construction (dimensions are in inch)

The liquid panel is constructed with the aluminum die described above in several steps. The steps are described below. The same steps are illustrated in Figure 2-10.

1. The first layer of Propore^{TM} membrane is attached to the aluminum box and taped.
2. Propore^{TM} membrane attached with the aluminum box is hanged over the block to produce tension. This is done to provide both lengthwise and widthwise tension to the membrane as the pre-stressed membranes are less sensitive to the pressure changes across the membrane (Larson 2006).

3. A guide which has the same size as the inner screen is laid on the first layer of membrane. Glue is sprayed on the membrane where the liquid spacer and coroplast^{TM} to be attached. 3M High-strength spray adhesive 90 is used for gluing. Liquid spacer, coroplast is laid on the membrane after spraying adhesive.
4. The guide is removed and the inner screen is laid on that place. Liquid spacers and coroplast^{TM} are laid on the edges of the inner screen. 3M hi-strength adhesive is sprayed again on top of the liquid spacer and coroplast.

(a) Step-1 (b) Step-2 (c) Step-3

(d) Step-4 (e) Step-5 (f) Step-6

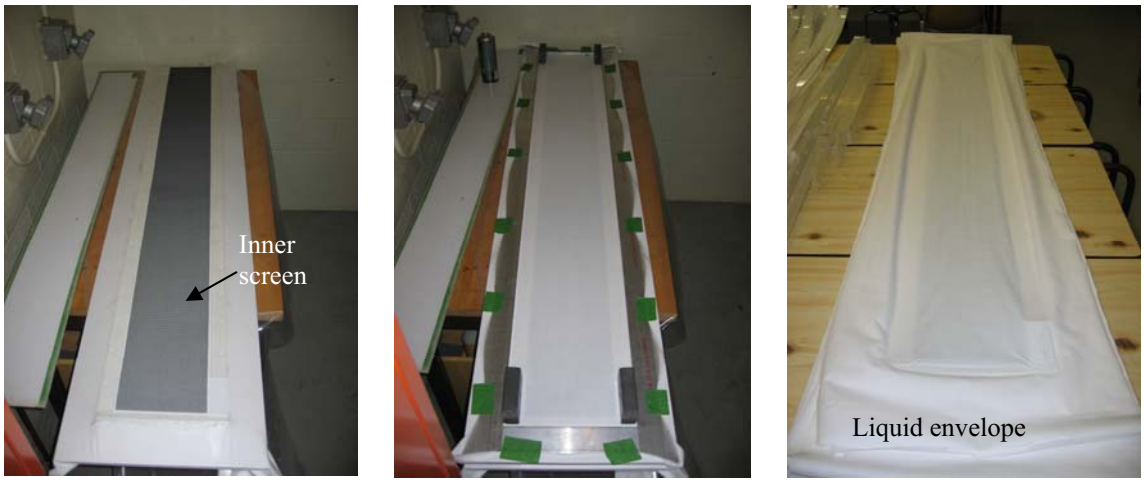

Figure 2-10. Different steps of liquid panel construction

5. Another layer of Propore^{TM} is taped with another box and laid on top of the inner screen, liquid spacer and coroplast^{TM}. The die with the membrane is kept like this for a while to cure the adhesive/glue.
6. The aluminum box is detached from the liquid envelope (consists of two layers of membranes, inner screen and liquid spacers) and is left for further cure.

The liquid envelope prepared at step-6 is attached with grooved air spacers at the top and bottom to support the outer screen. Three round spacers are attached with surgical tape longitudinally at the outer screen to create a uniform air-flow gap. The liquid panel edge is attached with aluminum tape to provide smooth air entrance to the exchanger. Figure 2-11(a) shows the placement of the round spacer and aluminum tape at the edge; whereas Figure 2-12 shows a complete liquid panel after construction.

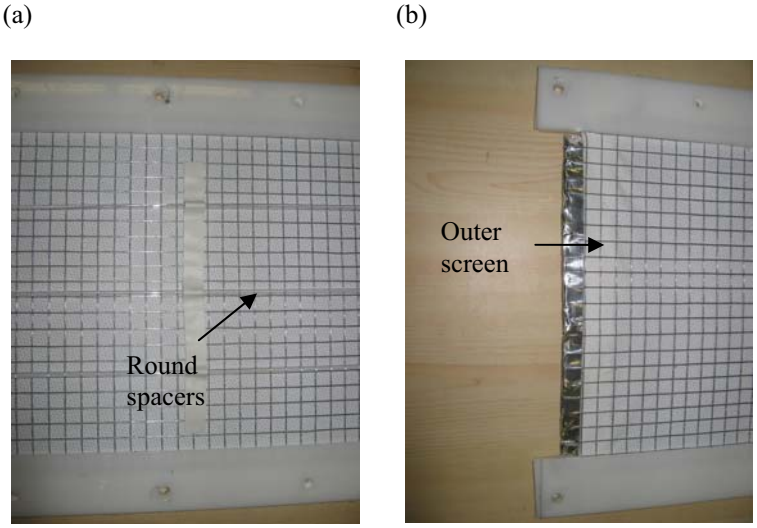

Figure 2-11. A closer view of the single liquid panel, a) middle of the liquid panel, and b) edge of the liquid panel

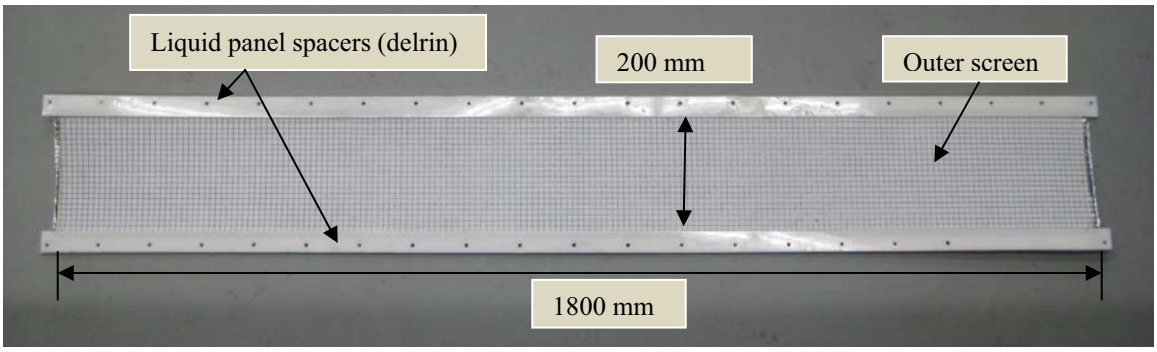

Figure 2-12. A single liquid panel after construction

Twenty (20) identical liquid panels (Figure 2-12) are constructed for the construction of two LAMEEs. After constructing all the liquid panels, leakage testing of the liquid panel is carried out using leakage testing apparatus developed by Beriault (2009). Leakage testing apparatus and testing procedures are described in Appendix-B. After checking leakages of the liquid panels, ten (10) liquid panels are bolted together between two outer aluminum plates of 1.58 mm (1/16 inch) thickness to construct a LAMEE as shown in Figure 2-13 and 2-14. Sidebars ($25.4 \times 25.4 \times 3.175$ mm or 1"x 1"x 1/8") are added on the outer aluminum plates to provide structural support and to minimize any desiccant solution leaks.

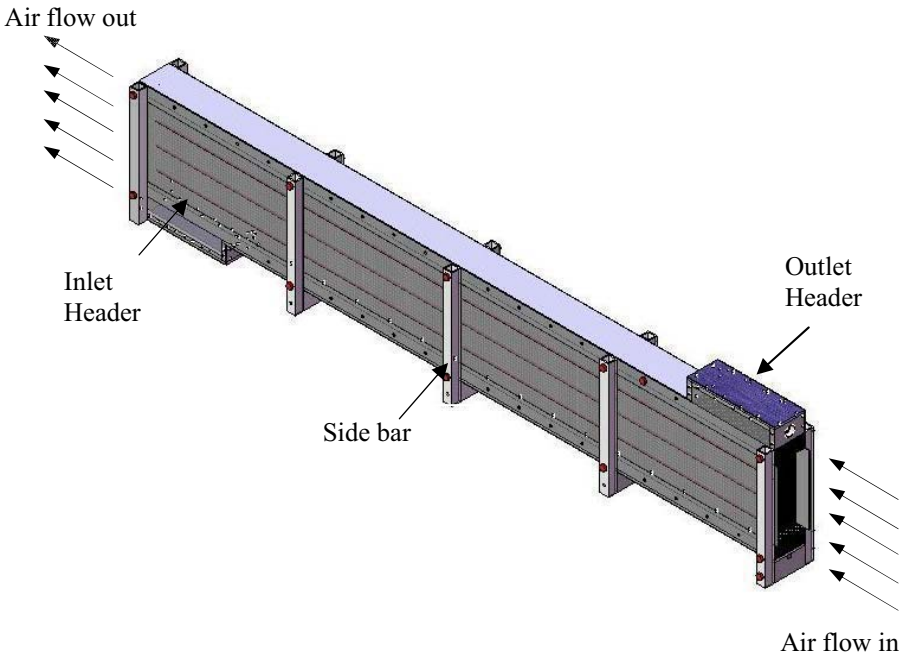

Figure 2-13. 3D-CAD model of the LAMEE based on design constraints and goals

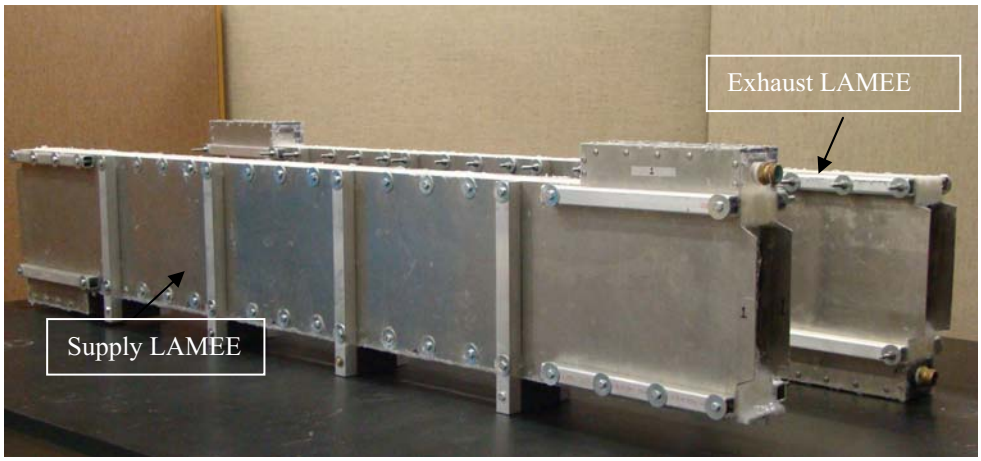

Figure 2-14. Constructed supply and exhaust LAMEE based on design constraints and goals

2.5 Other design considerations

Entrance length effect

Entrance length effect increases the heat and mass transfer in the hydrodynamic and thermal entry length region. In the design of the LAMEE, the entrance length effect is not considered. However, the entrance length effect on the heat transfer was investigated by using a correlation developed by Shah and London (1978, page 182). They recommended a correlation given by the equation (2.32) below to estimate the heat transfer coefficient in the entry length region between parallel plates with uniform wall heat flux. The correlation is also valid for laminar flow inside the duct:

$$\mathrm{Nu} = \begin{cases} 2.236\left(\mathrm{x}^*\right)^{-1/3} & \text{for } \mathrm{x}^* \le 0.001 \\ 2.236\left(\mathrm{x}^*\right)^{-1/3} + 0.9 & \text{for } 0.001 < \mathrm{x}^* < 0.01 \\ 8.235 + \dfrac{0.0364}{\mathrm{x}^*} & \text{for } \mathrm{x}^* \ge 0.01 \end{cases} \tag{2.32}$$

where,

$$\mathrm{x}^* = \frac{2\mathrm{x}/\mathrm{D_h}}{\mathrm{Re.Pr}} \tag{2.33}$$

Here x is the distance measured from the exchanger inlet and Pr is the prandtl number. Using equations (2.32) and (2.33), the Nusselt number (Nu) in the entrance region is calculated inside the LAMEE for the case of heat transfer only. It is found that the heat transfer coefficient was increased by 3%.

Area increase due to membrane deflection

Due to the membrane deflection, the membrane area increases inside the exchanger. This increased membrane area increases the heat and mass transfer rate between the liquid desiccant solution and air-flow. This effect is not considered in the exchanger

design. However, the membrane deflection is considered to figure out the percent of increase membrane area. It is found that the membrane area is increased around 1.4% due to the membrane deflection. For the present design this increase is considered insignificant.

2.6 Summary

In this chapter, the LAMEE design process is described. The LAMEE design is based on the sensible effectiveness correlation for a flat plate heat exchanger. A counter-cross-flow configuration is used in the current design. However, due to the small entrance ratio ($L_{sol,e}/L$), effectiveness of the current design varies less than 1% from the ideal counter-flow design. Therefore, the current design is very close to counter-flow and counter-flow heat exchanger correlation is used to design the exchangers. The property of desiccant solution which is used in this exchanger is discussed.

LAMEE design process involves membrane area estimation, determination of overall heat transfer coefficient, convective heat transfer coefficient, face velocity and membrane surface aspect ratio and air side pressure determination.

Construction of the liquid panels and LAMEE is also discussed after designing the LAMEE. Before the LAMEE construction leakage testing of the liquid panels is carried out using leakage testing apparatus.

LAMEE system design based on heat and mass transfer is also discussed. At the end of this chapter other design considerations are also discussed. Other design considerations include, entrance length effect, and area increase due to membrane deflection.

CHAPTER 3
TEST FACILITY AND UNCERTAINTY ANALYSIS

3.1 Introduction

The performance of the RAMEE system can be evaluated using the effectiveness equations shown in Chapter 1 (equation 1.2). Effectiveness depends on the air properties (dry air mass flow rate, temperature, humidity ratio and enthalpy) entering and leaving the RAMEE system. Therefore, the performance (or effectiveness) of the RAMEE system can be determined by measuring the air properties in the RAMEE system when it is operating in a laboratory or in an actual building. In this thesis, air properties are measured during laboratory testing. In addition to the air properties, some desiccant solution properties are also measured.

This chapter describes the air and desiccant solution properties that need to be measured in order to evaluate the RAMEE performance. It also presents the instrumentation used to measure these properties, the test facility used for laboratory testing of the RAMEE system, and the uncertainty analysis.

3.2 Properties, instrumentation and uncertainties

Different air properties (dry air mass flow rate, temperature, humidity ratio, and enthalpy) are required at the inlet and outlet of each exchanger (i.e. supply and exhaust LAMEEs) to calculate the RAMEE effectiveness (sensible, latent and total) based on equation (1.2). To fully document the experiments, the mass flow rate ($\dot{m}_{sol}$) and temperature (T_{sol}) of the coupling salt solution are also required. $\dot{m}_{sol}$ is required to investigate how the RAMEE effectiveness changes with different solution-to-air-heat-

capacity ratios (i.e. C_{sol}/C_{air}). The solution temperatures (T_{sol}) entering and leaving each exchanger (measurement positions X_5,X_6, X_7 and X_8 in Figure 3-1) are required to calculate solution properties (for example, $c_{p,sol}$) and to estimate the heat loss/gain from/to the solution. Tables 3-1 lists air properties required to evaluate each type of effectiveness. Figure 3-1 shows the measurement locations for all the air and desiccant solution properties required for RAMEE performance evaluation.

Table 3-1. Required air properties to calculate the different RAMEE effectiveness values

Effectiveness	*Air properties*
Sensible effectiveness	Dry air mass flow rate ($\dot{m}_{air}$), Temperature (T_{air})
Latent effectiveness	Dry air mass flow rate ($\dot{m}_{air}$), Humidity ratio (W_{air})
Total effectiveness	Dry air mass flow rate ($\dot{m}_{air}$), Enthalpy (h_{air})

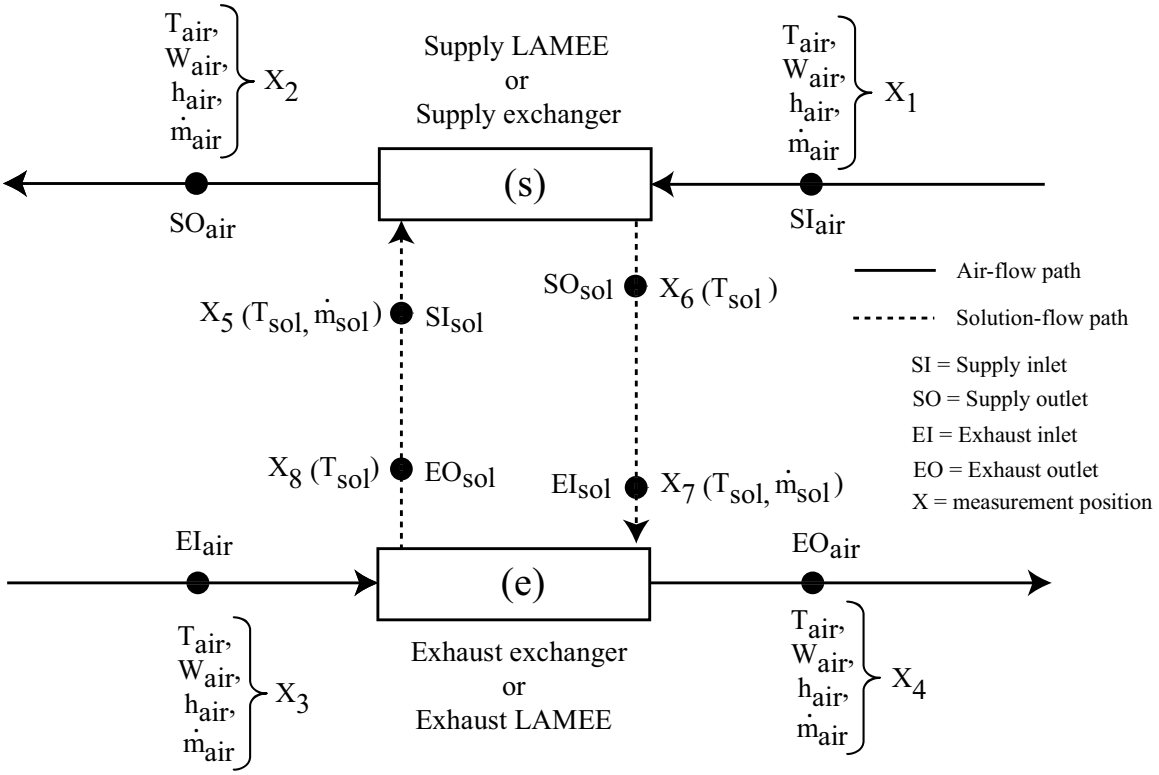

Figure 3-1. Air and desiccant solution property measurement positions for RAMEE performance evaluation

Among the air and desiccant solution properties shown in Figure 3-1, temperature (T_{air}, T_{sol}) is the only directly measured quantity. The other properties ($\dot{m}_{air}$, $\dot{m}_{sol}$, W_{air} and h_{air}) are calculated from other measured properties/physical quantities. The following sections describe the instruments used to measure the properties, calibration and uncertainties of the instruments and the methods used to determine the required properties from the measured data.

3.2.1 Temperature (T_{air}, T_{sol})

T_{air} and T_{sol} before and after each exchanger are measured using T-type thermocouples (0.51 mm diameter). Thermocouples are calibrated using an Ectron thermocouple simulator/calibrator (model:1100) connected to the data acquisition (DAQ) system as indicated in Figure 3-2. The simulator can simulate E, J, K or T thermocouples over the temperature range of -270°C to 1372°C. The simulator is accurate to ±0.1°C (Ectron-1100, 2008).

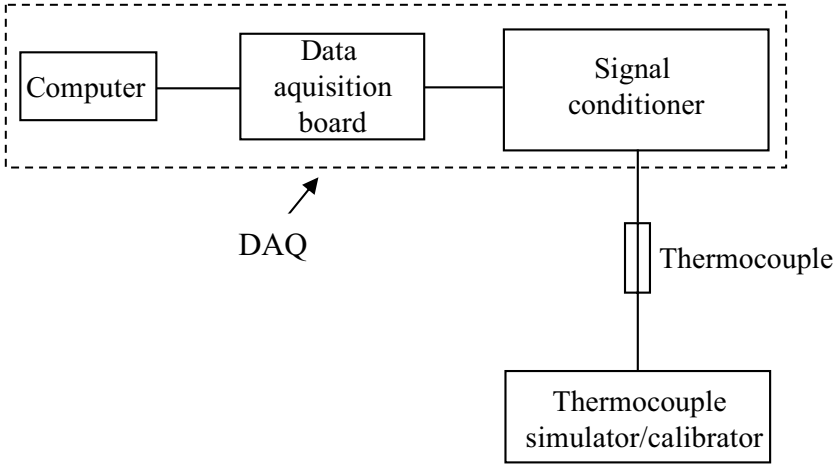

Figure 3-2. Schematic diagram of the thermocouple calibration process

When a specific temperature is set with the thermocouple simulator, the output voltage signals from the thermocouples are transmitted to a signal conditioner. The

response from the signal conditioner is then recorded using the data acquisition board, and computer. Different components of the DAQ system will be discussed in detail in Section 3.4. The DAQ system converts the voltage generated by the thermocouples to temperature reading by using standard temperature conversion polynomial equation.

Data recorded during the calibration process include uncertainties arising from precision (*P*) and bias (*B*) errors of the thermocouple sensor. Precision error is defined as the variation/scatter of the recorded data in the repeated measurements. The scatter of the calibration data from the mean is calculated using a standard deviation (SD) which is defined by equation 3.1 (ASME PTC 19.1-1998),

$$\mathrm{SD} = \sqrt{\sum_{k=1}^{N} \frac{\left(X_k - \overline{X}\right)^2}{N-1}} = P \tag{3.1}$$

where, X_k is the individual observation in a data sample, $\overline{X}$ is the sample mean, N is the number of measurements/observation.

Bias error (*B*) is defined as the measurement error that remains constant in repeated measurements of the true value using the instruments (ASME PTC 19.1 1998). Bias error is determined from the relationship of the calibrator data and recorded data from the sensor (e.g. thermocouple). Figure 3-3 shows the typical precision and bias errors of one of the thermocouples to be used to measure air temperature, as an example.

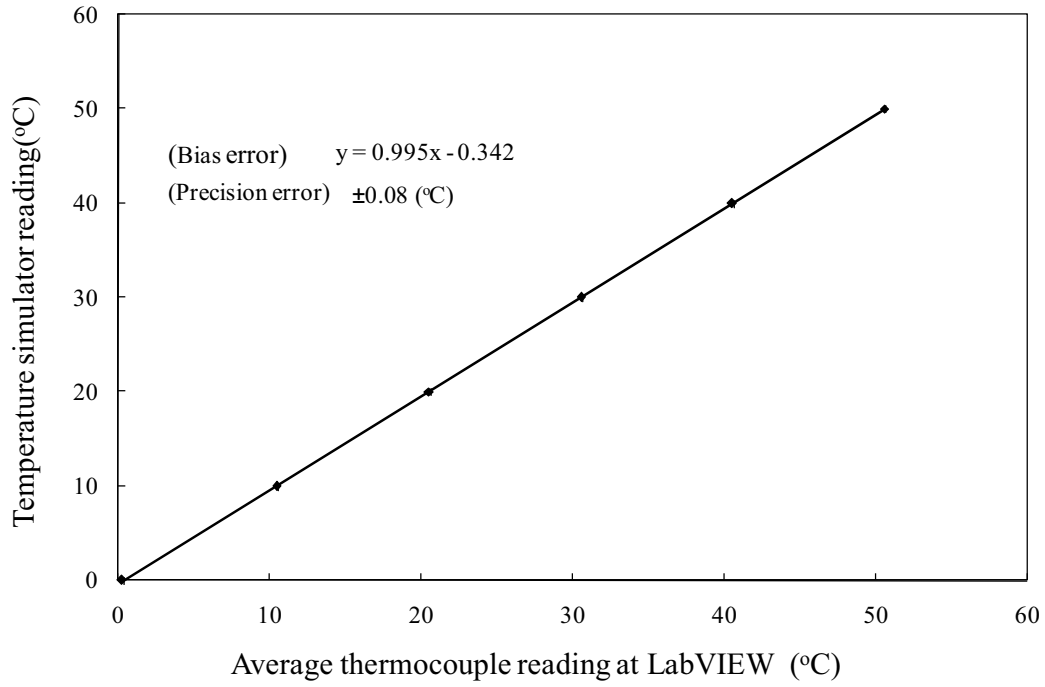

Figure 3-3. Typical calibration curve of thermocouples to be used to measure air temperature

The maximum precision error for the sensor shown in Figure 3-3 is found to be 0.08 (^{o}C) from different set points. The bias error is found linear (y = 0.995x-0.3426) as the linear relationship exists between simulator (i.e. true value) and thermocouple reading. The bias error of the sensor can be reduced if the sensor reading is corrected using the relationship found earlier. However, the calibrator has its own bias error which is then used in the uncertainty analysis of the sensor. The calibrator's bias errors are rated by the manufacturer during its calibration tests.

Overall uncertainty at 95% confidence interval of the sensor (e.g. thermocouple) is determined by combining the bias and precision errors of the sensor using equation (3.2) (ASME PTC 19.1 1998),

$$U_{95\%} = \sqrt{(B)^2 + (t * P)^2} \tag{3.2}$$

where $U_{95\%}$ is the total uncertainty with a 95% confidence interval, B is the bias error, P is the precision error (equation 3.1), and t^* is the student-t value. The student-t distribution depends on the number of data points considered to determine the precision error. In the current analysis, a t* value of 2.228, which corresponds to 10 data points (ASME PTC 19.1 1998, Table B-1), is used.

Each sensor may have different uncertainties associated with it. In the current analysis the worst case scenario is chosen and applied to all sensors for simplicity. Using equation (3.2) at worst case scenario the 95% uncertainty of the thermocouples is found to be ±0.20 (^oC).

3.2.2 Humidity ratio of air (W_{air})

The humidity ratio of air (W_{air}) is calculated from the measured temperature and relative humidity (RH) of the air. The humidity ratio is defined (ASHRAE, 2005):

$$W_{air} = 0.62198\left(\frac{P_{water\ vapor}}{P_{atm} - P_{water\ vapor}}\right) \tag{3.3}$$

where P_{atm} is the atmospheric pressure and $P_{water\ vapor}$ is the partial pressure of water vapor in air, which can be calculated from the RH and the saturation pressure ($P_{air,sat}$) of air at that temperature as shown below.

$$P_{water\ vapor} = P_{air,sat}\left(\frac{RH}{100}\right) \tag{3.4}$$

$P_{air,sat}$ is calculated using correlation which is a function of T_{air} shown in Appendix-A.

When calculating W_{air} from T_{air} and RH, it is important to use measurement data from the same measurement point. RH and T_{air} are measured using a Vaisala humidity and temperature transmitter (model: HMP230). The humidity and temperature transmitter

incorporates a capacitive humidity sensor (humicap) and Resistance Temperature Detector (RTD). The installed humicap sensor converts the input RH (0-100%) to voltage output ranges from 0-1 V using a linear relationship. The RTD converts the temperature input (-40 to +200^{o}C) to voltage output ranges from 0 to 10 V.

The humidity and temperature transmitter is calibrated using a humidity generator and DAQ system as shown schematically in Figure 3-4. As shown in Figure 3-4, the humidity generator consists of an air supply, saturator, an expansion valve and a constant humidity chamber and operates over a large range of humidity and temperature (10°C to 60°C and 10% RH to 95% RH). The accuracy of the relative humidity generator is ±1% (Mini-1200, 2004).

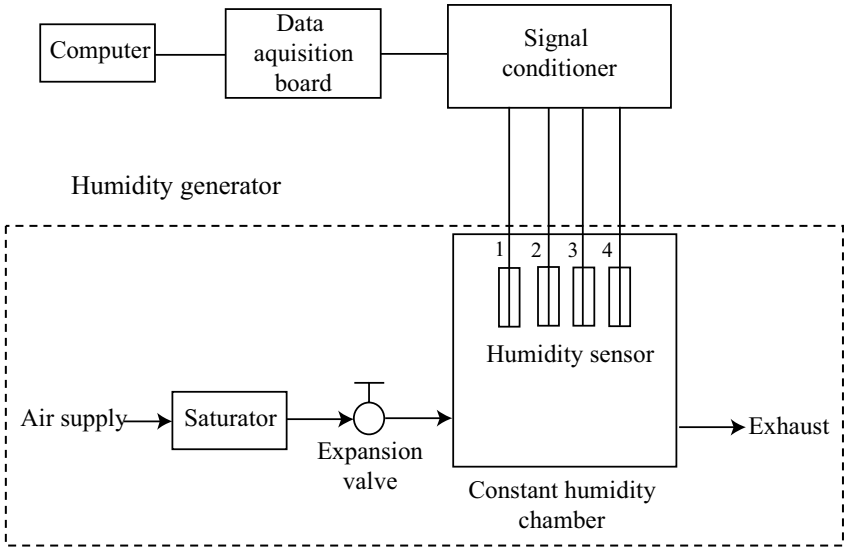

Figure 3-4. Schematic diagram of the humidity and temperature transmitter calibration

The humidity generator maintains a desired relative humidity at the humidity chamber by changing the pressure of air or gas of the humidity generator. At first air or gas (e.g. nitrogen) is saturated with water vapor at a given temperature and pressure. After it is saturated, the saturated gas flows through an expansion valve where it is

isothermally reduced to the test pressure. As pressure is lowered, RH drops. By controlling the pressure change, the RH of the air is controlled at constant humidity chamber.

Humidity sensors are placed inside the constant humidity chamber for calibration. For a specific RH value generated by the constant humidity chamber, the readings of the humidity sensor voltage are recorded using the DAQ system. The recorded voltage is converted to pressure reading using the linear relationship described earlier. Figure 3-5 shows the typical calibration curve for RH sensors to be used to measure relative humidity of air as an example. The precision error is found to be ±0.3 % and the bias error found to be linear (y = 1.0458x-2.2251).

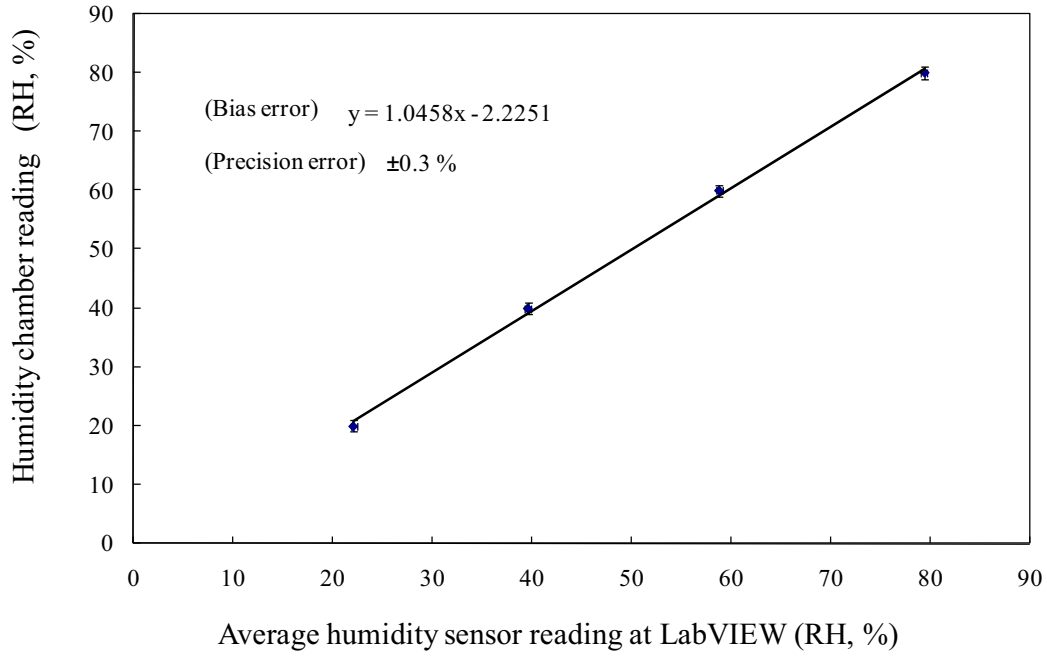

Figure 3-5. Typical calibration curve of RH sensors to be used to measure relative humidity of air

All the humidity sensors are calibrated by the above mentioned procedures and the 95% uncertainty of the RH sensor is calculated using the process described in section 3.2.1. At worst case scenario the 95% uncertainty of the RH sensor is found ±1.2 (%).

Calibrations of the RTD sensors are done using a dry block (model: 9107) temperature generator. The temperature and humidity transmitter is placed inside the dry bock generator and data are recorded using the DAQ system. At worst case scenario the 95% uncertainty of the RTD sensor is found to be ±0.2 (^{o}C).

3.2.3 Dry air mass flow rate ($\dot{m}_{air}$)

Dry air mass flow rates are calculated from volumetric flow measurements before and after each exchanger as shown in Figure 3-1. The following equation provides the dry air mass flow rates.

$$\dot{m}_{air} = \rho_{dry,air} q_{air} \tag{3.5}$$

where, $\dot{m}_{air}$ is the dry air mass flow rate (kg/s), $\rho_{dry,air}$ is the dry air density (kg/m^3), and q_{air} is the measured volume flow rate of air (m^3/s). The density of dry air is a function of air temperature (T_{air}), atmospheric pressure (P_{atm}), vapour pressure ($P_{water\ vapor}$), and the gas constant (R). It can be found from the ideal gas law as shown below.

$$\rho_{dry,air} = \frac{P_{atm} - P_{water\ vapor}}{RT_{air}} \tag{3.6}$$

The volumetric flow rate of air (q_{air}) in equation (3.5) is calculated from the pressure drop across an orifice plate as given below (ISO standard 5167-1),

$$q_{air} = C_d \frac{\pi}{4} d^2 \left[\frac{2\Delta P}{\rho_{humid,air}\left(1-\beta^4\right)} \right]^{\frac{1}{2}} \tag{3.7}$$

where C_d is the discharge coefficient, d is the diameter of the orifice plate opening, ΔP is the measured pressure drop across the orifice plate, $\rho_{humid,air}$ is the density of the humid air, and $\beta = \frac{d}{D}$ is the expansion coefficient, where D is the inside diameter of the pipe where the orifice plate is installed. The density of humid air ($\rho_{humid,air}$) in equation (3.7) is calculated using equation (3.8) below.

$$\rho_{humid,air} = \frac{P_{atm}}{RT_{air}} \tag{3.8}$$

The value of C_d can be calculated from the equation (3.9) (ISO standard 5167-1). The equation is valid for the specific configuration of the orifice plate where two static pressure taps are located at 1D upstream and D/2 downstream of each orifice plate to measure ΔP.

$$C_d = 0.5959 - 0.0312\beta^{2.1} - 0.1840\beta^{8} - 0.0029\beta^{2.5}\left(\frac{10^6}{Re_D}\right)^{0.75} \tag{3.9}$$
$$0.090 \times 0.0390 - 0.0337 \times 0.47\beta^{3}$$

C_d depends on the Reynolds number (Re_D) and β. Since the velocity, which is determined from the volumetric flow rate (q_{air}), is needed to calculate Re_D, C_d and q_{air}, iteration is required to solve for q_{air} using equations (3.7) and (3.9).

Equations (3.5) to (3.9) indicate that the pressure drop (ΔP) measurement across the orifice plate is required to calculate $\dot{m}_{air}$. ΔP is measured by a differential pressure transducer (Validyne-P855, 2007) which works with both liquids and gases directly at the sensing diaphragm. Depending on the sensing diaphragm, the pressure transducer measurement range varies. The differential pressure transducer is connected to the upstream and downstream pressure taps using flexible PVC tubing (1/4″ diameter)

according to the ISO standard 5167-1. The installed pressure transducer can measure accurately from 1 inch of H_2O (249 Pa) to 5 inch of H_2O (1245 Pa).

The pressure transducer is calibrated against a high precision Druck electronic pressure calibrator as shown in Figure 3-6 (a). During calibration, a specific pressure is applied on the transducer using the Druck pressure calibrator and the transducer voltage signals are recorded on a computer using the DAQ system. The recorded voltage reading is then converted to pressure reading using the linear conversion relationship of 1 V = 1 inch of H_20 (≈ 249 Pa) (Erb, 2007). Figure 3-6 (b) shows the typical calibration curve for one of the pressure transducers to be used to measure pressure difference across the orifice plate as an example.

(a)

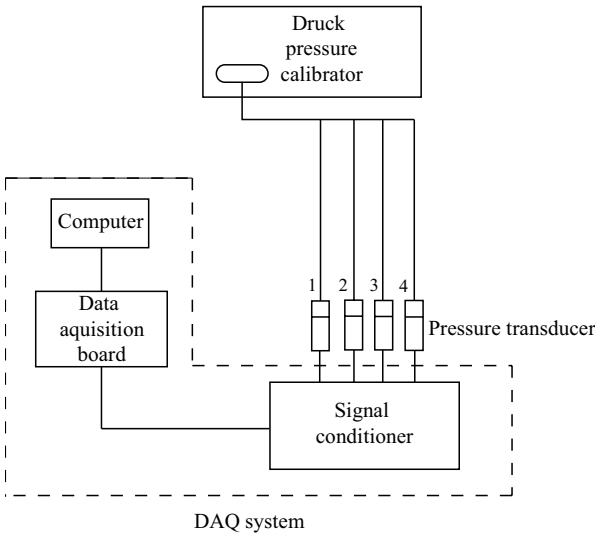

(b)

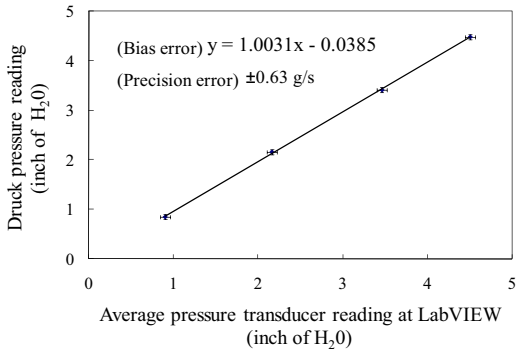

Figure 3-6. a) Schematic diagram of the differential pressure transducer calibration process, b) typical calibration curve for one of the pressure transducers

The uncertainty of all the pressure transducers was carried out using the process described in Section 3.2 and at worst case 95% uncertainty of the pressure transducer is found to be 0.16 inch H_2O (≈40 Pa).

3.2.4 Enthalpy of air (h_{air})

The enthalpy of air (h_{air}) required to calculate the total effectiveness (Table 3-1), is calculated based on equation (3.10) (ASHRAE, 2005).

$$h_{air} = 1.006T_{air} + W_{air}\left(2501 + 1.86T_{air}\right) \tag{3.10}$$

T_{air} in equation (3.10) is measured using thermocouples (section 3.2.1) and W_{air} is calculated from the capacitance RH and temperature (RTD) sensors (Section 3.2.2) described earlier.

3.2.5 Desiccant solution mass flow rate ($\dot{m}_{sol}$)

The desiccant solution mass flow rate is calculated from the solution volume flow rate (q_{sol}) which is measured using a Dwyer variable area flow meter (rotometer). The measurement range of the flow meter is 0.2 GPM (US) to 2.2 GPM (US) water.

The flow meter is calibrated by measuring the time it takes to fill a container with a certain mass of fluid. Calibration curves for both water and desiccant solution are developed. An electronic balance (model: Ohaus Voyager Pro VP6102CN) which has a maximum measurement capacity of 6100 g and has accuracy of ±0.01 g is used in the calibration. Figure 3-7 (a) shows the calibration curves for the desiccant solution and water mass flow rates against flow meter reading (GPM). The standard deviation (precision error, *P*) of the calibration data for $\dot{m}_{sol}$ is found ±0.63 gram/s.

Figure 3-7(b) shows the flow meter reading against calculated volume flow rate of water and desiccant solution in US gallon per minute (GPM). It shows that calculated

water flow rate is off by 4% (at 1 GPM) to 8% (at 0.3 GPM) from the flow meter reading. However, the calculated desiccant solution-flow rate is off by 34% (at 1 GPM) to 54% (at 0.3 GPM) from the manufacture's data.

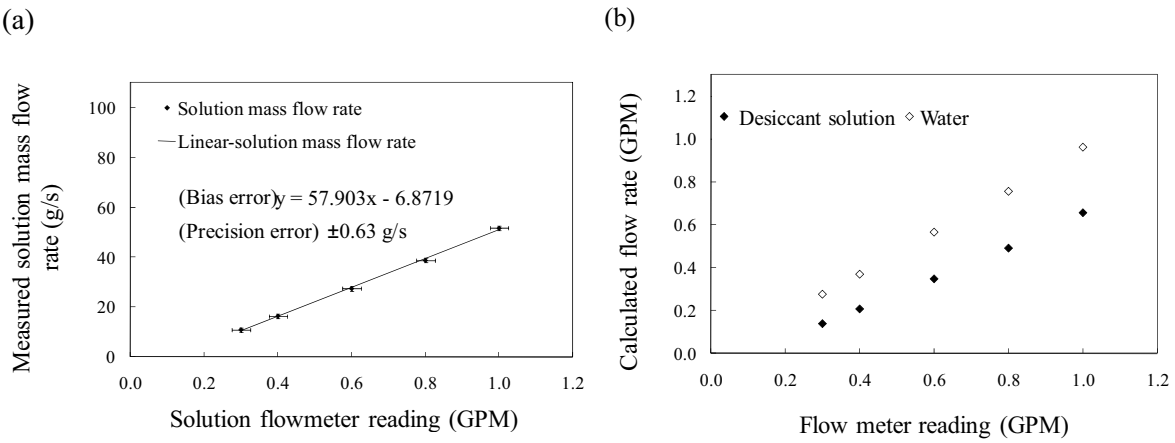

Figure 3-7. a) Calibration curve for $\dot{m}_{sol}$ b) calibration curve for q_{sol} and q_{water}

3.3 Test facility

To measure the physical quantities discussed in section 3.2, which are required to evaluate RAMEE performance, a test facility was developed based on ISO Standard 5167-1 in the heat transfer laboratory at the University of Saskatchewan by Erb (2007). The test facility is named the Run-Around Membrane Energy Exchanger Test Apparatus (RAMEETA). The RAMEETA is composed of an air-flow loop and desiccant solution-flow loop (Figure 3-8). The solid lines are the air-flow loop and the dashed lines are the liquid flow loop. The air-flow loop delivers conditioned air to the exchangers and the solution-flow loop couples the two exchangers.

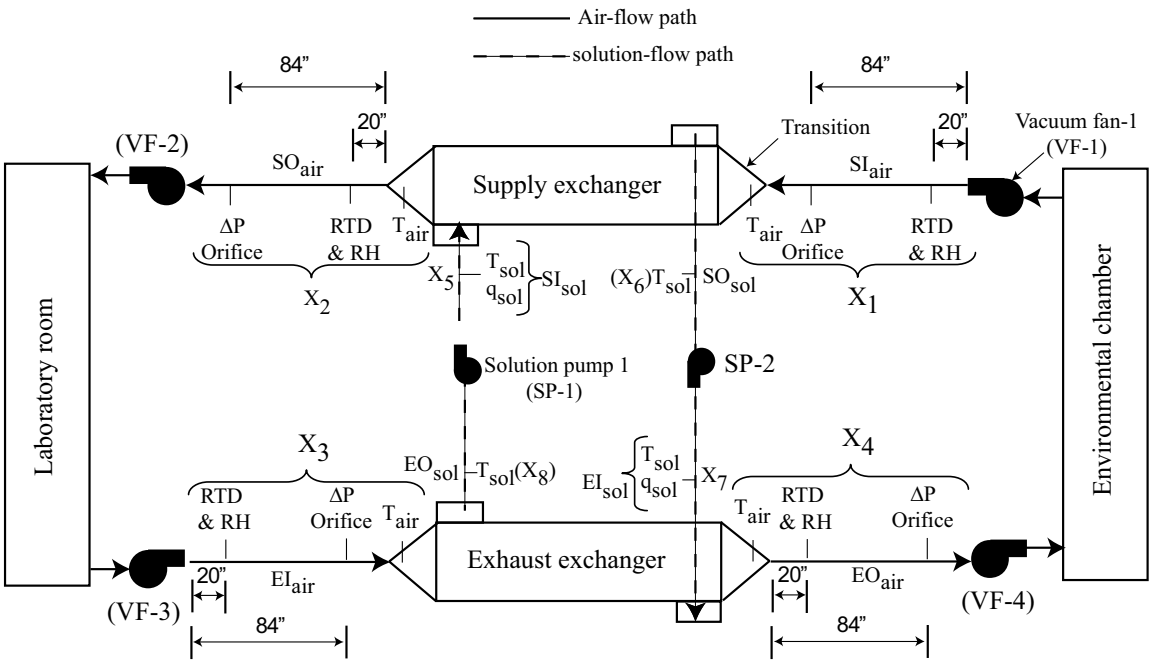

Figure 3-8. Schematic diagram of the Run-Around Membrane Energy Exchanger Test Apparatus (RAMEETA) with air and desiccant solution property measurement positions

3.3.1 Air-flow loop

In the supply air stream, air from an environmental chamber enters the supply air inlet (SI_{air}) duct (2 inch diameter) which delivers the air to the supply exchanger through a transition. The air leaving the supply exchanger, flows through the supply air outlet (SO_{air}) duct and is exhausted to the laboratory room. The laboratory is large enough to act as a constant temperature and humidity source for the exhaust air steam. The exhaust air stream enters from the laboratory and passes through the exhaust air inlet (EI_{air}) ducting, the transitions, the exhaust exchanger, and the exhaust air outlet (EO_{air}) ducting before entering the environmental chamber. The supply and exhaust air streams, the laboratory room and the environmental chamber constitute an air-flow loop. Air flow in the loop is maintained by four 5.0 hp vacuum fans. Vacuum fans are controlled by variable transformers which control the voltage delivered to them.

The environmental chamber controls the supply inlet (SI_{air}) temperature (T_{air}) and RH and is set to represent outdoor environmental conditions. The environmental chamber is capable of providing T_{air} between -40 ^{o}C and +40 ^{o}C and an RH of up to 90%. Air humidity (W_{air}) is controlled by a humidity generator which injects steam into the environmental chamber. The operation of the humidity generator is controlled by a RH sensor installed inside the chamber. Depending on the set point of the RH sensor, the steam generator injects steam in to the chamber. The temperature of the environmental chamber is controlled by a chiller and two room heaters. The set points of the heaters are adjusted manually by trial and error method as they change with the supply air-flow rates.

Air-flow in the RAMEE system travels four (4) identical branches (SI_{air} ,SO_{air} ,EI_{air} ,EO_{air}) before and after the exchangers (Figure 3-8). The ISO Standard 5167-1 is followed to design each branch of the test apparatus piping as reported by Erb (2007). Figure 3-9 shows the details of SI_{air} branch as an example.

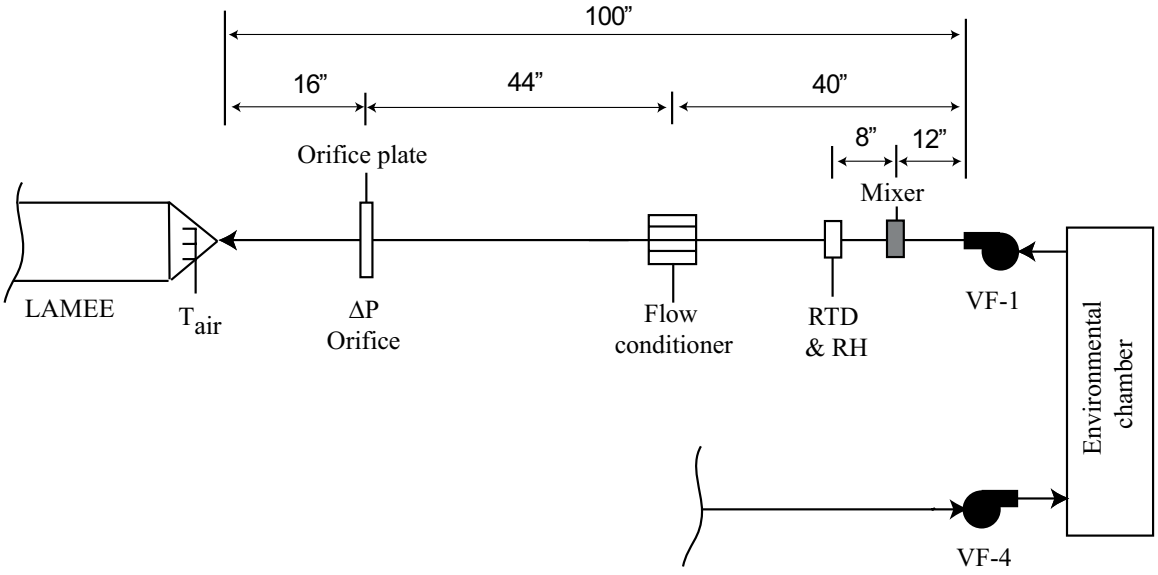

Figure 3-9. Schematic diagram of SI_{air} branch

Each branch consists of 2-inch-diameter PVC piping. Air in each branch first passes through a mixer which creates uniform temperature and humidity distributions in the duct. Temperature (RTD) and humidity (RH) are measured 8" (203 mm) downstream of the mixer. After the mixer, the air passes through a flow conditioner that straightens the flow before entering the orifice plate. A honeycomb grid straightener, shown in Figure 3-10, is used to create a uniform velocity profile. The location of the orifice plate downstream of the flow straightener ensures flow is fully developed. All the air ducts are covered with 1" thick fiber glass insulation to reduce the heat transfer with the surroundings.

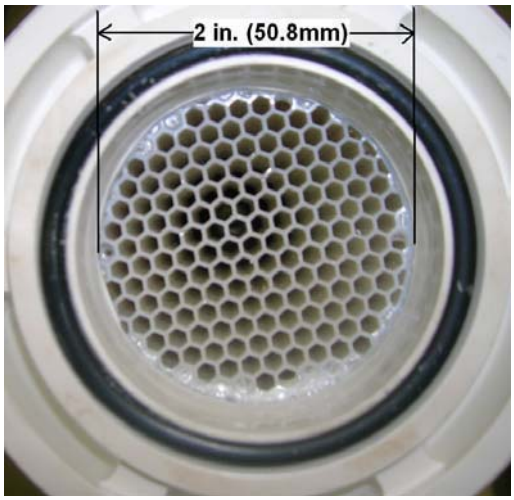

Figure 3-10. Photograph of the honeycomb flow straightener and distribution conditioner (Erb , 2007)

For testing a large range of air-flow rates in the test facility, several different orifice plates are developed by Erb (2007) with diameter ratios (β) ranging between 0.20 and 0.80. In the current study the C_d value is calculated using the iteration of equation (3.7) and equation (3.9) and reported in Table 3-2 for different orifice plates developed by Erb

(2007) with their rated minimum and maximum mass flow rates based on the installed transducer measurement range (1 inch H_20 to 5 inch of H_20).

Table 3-2. Orifice plate throat diameters and minimum and maximum air-flow rates

Orifice Plate Throat Diameter (mm)	*ΔP across Orifice(in H2O)*	*Mass Flow Rate (kg/s)*	C_d
12.5	1	0.0018	0.61
12.5	5	0.0040	0.61
18	1	0.0037	0.61
18	5	0.0083	0.61
26	1	0.0082	0.62
26	5	0.0180	0.61
30	1	0.0112	0.62
30	5	0.0245	0.61
38	1	0.0199	0.61
38	5	0.0438	0.60

The data of Table 3-2 show that the coefficient of discharge varies between 0.61 and 0.62. The coefficient of discharge of 0.61 is used in this study to simplify the experimental data analysis. According to the Table 3-2, the maximum and minimum air mass flow rates which can be measured with the combination of orifice plates and pressure transducer used in the test facility are $1.8x10^{-3}$ kg/s and $43.8x10^{-3}$ kg/s, respectively.

3.3.2 Desiccant solution-flow loop

The desiccant solution-flow loop in the RAMEETA is used to circulate desiccant solution between the exchangers (Figure 3-11). Two 1/8-hp (70-W) magnetic drive pumps, one for each exchanger, are installed to circulate the desiccant solution. In order to reduce the risk of cavitation, the pump inlets are connected from the bottom of the reservoirs.

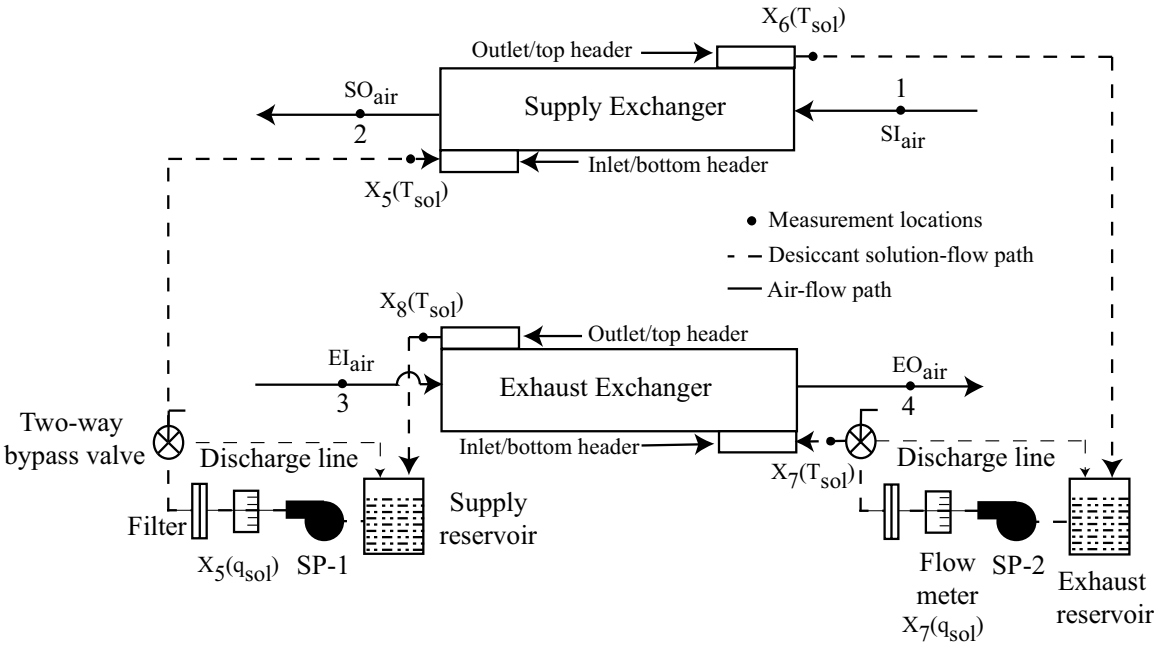

Figure 3-11. Desiccant solution-flow loop and measurement positions in the RAMEETA.

Two flow meters, one for each pump, capable of controlling the desiccant solution-flow rate between 0.1 and 1.5 US GPM (0.006 L/s to 0.096 L/s) are used to control the desiccant solution-flow rate. Foam insulation (9.53 mm or 3/8" thick) is used on all the solution piping to reduce heat transfer with the surroundings. Two-way bypass valves are installed upstream of the inlet headers of the supply exchanger and exhaust exchanger to control the desiccant solution-flow and discharge the desiccant solution to the storage reservoirs when the RAMEE system is not operational. Filters are installed between the flow meter and the two-way bypass valve to remove solid particles from the desiccant solution. Thermocouples are installed before and after the exchangers for monitoring the desiccant temperature change through the solution loop.

3.4 Data acquisition system

A National Instruments data acquisition (DAQ) system is used to digitize the electronic signals from the different sensors during the experiments. The DAQ system is comprised of a terminal block, signal conditioner, data acquisition board, a high speed computer and LabVIEW software. Figure 3-12 shows all the sensors and DAQ system for the RAMEETA and Figure 3-13 shows the two LAMEEs are installed in the RAMEETA with the data acquisition system. All the sensors (pressure transducers, RTD, thermocouples) are connected to a terminal block (model: NI SCXI 1303). A terminal block is useful for taking measurements from a wide variety of sensors and signal types. The installed terminal block can hold 32 sensors and is designed especially for high-accuracy temperature measurements. The thermocouples in the RAMEETA are connected directly to the terminal block, while the humidity sensors, RTDs and pressure transducers are all connected to the terminal block through shielded copper paired cables.

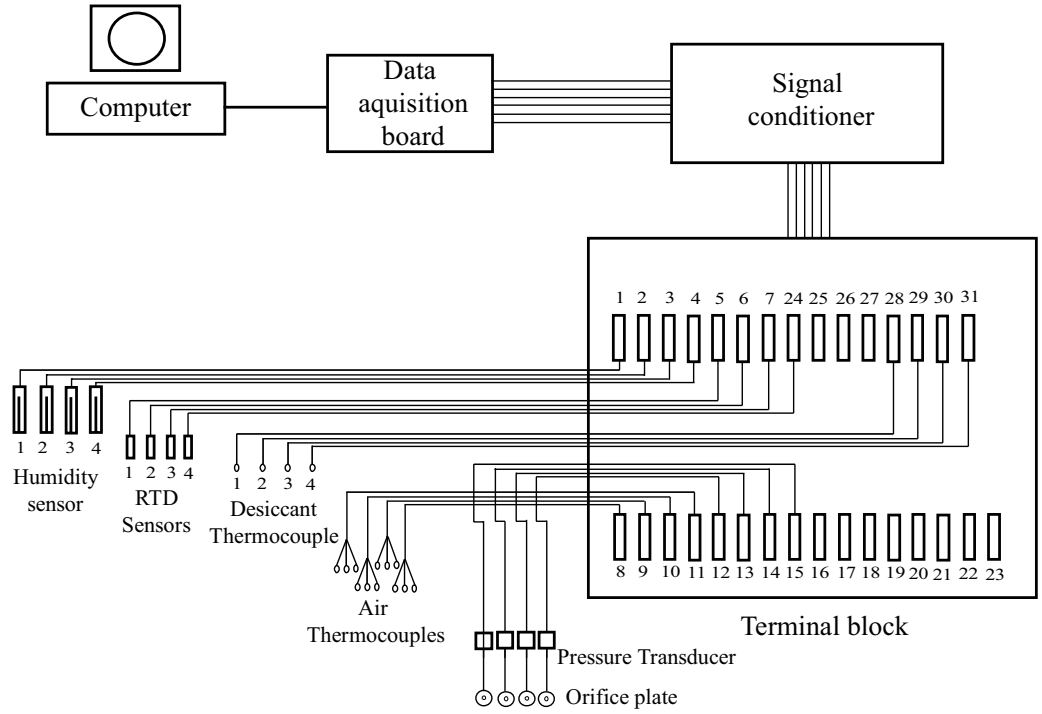

Figure 3-12. Schematic diagram of the data acquisition system

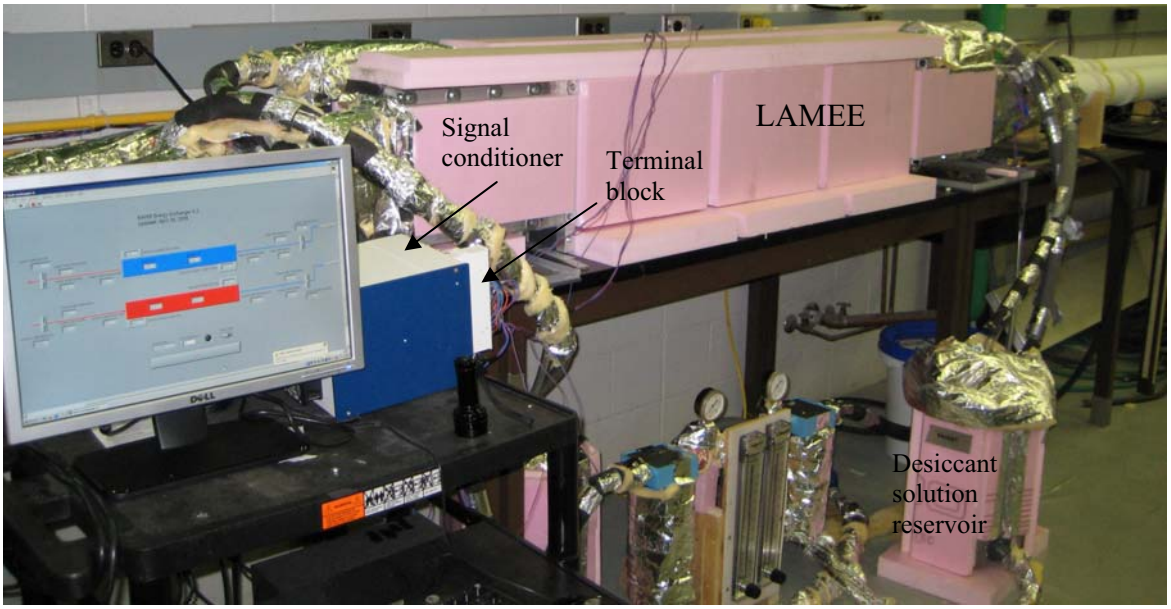

Figure 3-13. Supply and exhaust LAMEE (covered with insulation) installed in the RAMEETA with DAQ system

Voltage signals received from different sensors at the terminal block are sent to a National Instrument Signal conditioner shown in Figure 3-12 and 3-13 (model: NI SCXI 1000). The signal conditioner holds the terminal blocks and synchronizes the timing between the terminal blocks and the data acquisition board.

Conditioned signals from the signal conditioner are sent to the high speed data acquisition board (model: NI PCI 6251). The board can convert the analog signals to digital signals at the maximum rate of 2.8 Mega samples/s with 16-bit accuracy when measuring all channels (NI PCI-6251, 2008).

The data acquisition board sends the digital signals to a desktop computer where they are recorded using the LabVIEW software developed by National Instruments. LabVIEW software is well known to create a measurement application with a custom user interface. In the RAMEETA, a LabVIEW interface is developed in-house to communicate, control and acquire data from the different sensors. In the current RAMEETA system, LabVIEW

software is set to record data at an interval of 10 seconds for the RAMEE test. Each time it records 100 data at the speed of 1 kHz and then averaged over 1 second. The acquired average data in the form of voltage is then converted to temperature, pressure readings using the linear conversion provided by the manufacture and in-house calibration curves. The solution-flow rate is recorded once from the two flow meters and adjusted manually to have the same value during each test.

3.5 Uncertainties of the calculated parameters

Uncertainties of the calculated parameters (e.g. effectiveness, dry air mass flow rate), which are dependent on the uncertainties of the measuring sensors/instruments, are determined using error propagation as described in the ASME PTC 19.1-1998. The general equation for determining the total uncertainty (combining both the precision and bias errors) of any calculated parameter is shown in equation (3.11) below,

$$U_R = \left[\left(\frac{\partial \mathrm{R}}{\partial \mathrm{y}_1} U_{\mathrm{y}_1} \right)^2 + \left(\frac{\partial \mathrm{R}}{\partial \mathrm{y}_2} U_{\mathrm{y}_2} \right)^2 + \ldots + \left(\frac{\partial \mathrm{R}}{\partial \mathrm{y}_\mathrm{j}} U_{\mathrm{y}_\mathrm{j}} \right)^2 \right] \tag{3.11}$$

where $\mathrm{y}_{\mathrm{i},}\,(\mathrm{i}=1 \text{ to } \mathrm{j})$ is the independent variable, $U_{\mathrm{y}_\mathrm{i}}$ is the total uncertainty of the independent variable, y_i (Table 3-2) , and R is the calculated parameter.

$$\mathrm{R} = \mathrm{f}\left(\mathrm{y}_1, \mathrm{y}_2, \ldots., \mathrm{y}_\mathrm{j}\right) \tag{3.12}$$

The sensitivity θ_i of the i-th variable, y_i is defined as

$$\theta_\mathrm{i} = \frac{\partial R}{\partial \mathrm{y}_\mathrm{i}} \tag{3.13}$$

The uncertainty expression then can be re-written in the following form.

$$U_R = \left[\sum_{\mathrm{i}=1}^{\mathrm{j}} \theta_\mathrm{i}^2 U_{\mathrm{y}_\mathrm{i}}^2 \right]^{1/2} \tag{3.14}$$

Based on the general expression shown in equation (3.14), uncertainties of different calculated parameters can be determined. Parameters that require calculated uncertainties include the saturation vapor pressure, vapor pressure, humidity ratio, enthalpy, dry air mass flow rate, and RAMEE effectiveness. Beriault (2009) reports the expressions for estimating uncertainties of different calculated parameters. Expression for the uncertainties involved in the RAMEE supply and exhaust exchanger effectiveness are shown in equations (3.15) and (3.16) below, as an example.

$$U_{\varepsilon_{o,x,(s)}} = \left(\begin{array}{l} \left(\frac{\varepsilon_{o,x,(s)}}{\dot{m}_{air,supply}} U_{\dot{m}_{air,supply}} \right)^2 + \left(\frac{\varepsilon_{o,x,(s)}}{\dot{m}_{air,min}} U_{\dot{m}_{air,min}} \right)^2 + \left(\frac{\varepsilon_{o,x,(s)}}{X_1 - X_2} U_{X_2} \right)^2 \\ + \left(\frac{\varepsilon_{o,x,(s)}}{X_1 - X_3} U_{X_1} \right)^2 + \left(\frac{\dot{m}_{air,supply} X_3}{\dot{m}_{air,min} (X_1 - X_3)^2} U_{X_3} \right)^2 \end{array} \right)^{1/2} \quad (3.15)$$

$$U_{\varepsilon_{o,x,(e)}} = \left(\begin{array}{l} \left(\frac{\varepsilon_{o,x,(e)}}{\dot{m}_{air,exhaust}} U_{\dot{m}_{air,exhaust}} \right)^2 + \left(\frac{\varepsilon_{o,x,(e)}}{\dot{m}_{air,min}} U_{\dot{m}_{min}} \right)^2 + \left(\frac{\varepsilon_{o,x,(e)}}{X_3 - X_4} U_{X_4} \right)^2 \\ + \left(\frac{\varepsilon_{o,x,(e)}}{X_1 - X_3} U_{X_3} \right)^2 + \left(\frac{\dot{m}_{air,exhaust} X_1}{\dot{m}_{air,min} (X_1 - X_3)^2} U_{X_1} \right)^2 \end{array} \right)^{1/2} \quad (3.16)$$

The uncertainty associated with the effectiveness of the RAMEE system which is the average of supply and exhaust exchanger effectiveness can be calculated as,

$$U_{\varepsilon_{o,x}} = \frac{\left(U^2_{\varepsilon_{o,x,(s)}} + U^2_{\varepsilon_{o,x,(e)}} \right)^{1/2}}{2} \quad (3.17)$$

3.6 Overall uncertainties

Data which are recorded using the DAQ system consist of uncertainties. The uncertainty calculations of the different sensors are discussed in Section 3.2. Table 3-3

shows the precision and bias errors and total uncertainty of the different sensors and calculated parameters (i.e. dry air mass flow rate).

Table 3-3. Precision, bias and total uncertainties of all sensors used in the RAMEETA

Measurement	*Precision*	*Bias*	*Uncertainties*	*Units*
RTD	0.02	0.2	0.20	(^{o}C)
Thermocouple	0.08	0.1	0.20	(^{o}C)
Humidity sensor	0.32%	1.0%	1.2%	(% R.H.)
Dry air mass flow rate	0.34	0.31	0.8	(g/s)
Desiccant solution mass flow rate	0.63	0.01	1.4	(g/s)
Pressure transducer	0.07	0.00125	0.16	inch H_2O

As mentioned in the objective (Chapter 1), The RAMEE system will be tested at AHRI summer and winter conditions. Therefore, the uncertainty involves of the calculated effectiveness values using the sensors used at AHRI condition is carried out. Table 3-4 shows the uncertainty (equation 3.17) of the RAMEE system effectiveness (sensible, latent and total effectiveness) at the maximum and minimum air-flow rates of the test facility.

Table 3-4. Uncertainties of the RAMEE system effectiveness at AHRI summer and winter conditions

Test condition	*Mass flow (kg/s)*	*Uncertainty (RAMEE system) (average of supply and exhaust exchanger)*		
		Sensible $U_{\varepsilon_{o,sensible}}$	*Latent* $U_{\varepsilon_{o,latent}}$	*Total* $U_{\varepsilon_{o,total}}$
AHRI summer	0.0018	45%	45%	39%
	0.0438	3%	3%	2%
AHRI winter	0.0018	45%	46%	39%
	0.0438	2%	4%	2%

3.7 Steady-state criteria of the RAMEE system

In order to check if the RAMEE system has reached steady-state conditions during tests, different balance checks of the experimental data may be performed. A balance check can also be used to investigate bias error during tests (Simonson et al., 1999).

Mass balance/conservation of dry air:

Mass balance of dry air may be used as a tool to check any air leakages in the RAMEE system. Mass balance on both the supply and exhaust exchanger are represented mathematically as follows (Simonson et al., 1999).

$$\Delta \dot{m}_{air,supply} = \left| \dot{m}_{air,1} - \dot{m}_{air,2} \right| \leq U_{\Delta \dot{m}_{air,supply}} \tag{3.18}$$

$$\Delta \dot{m}_{air,exhaust} = \left| \dot{m}_{air,3} - \dot{m}_{air,4} \right| \leq U_{\Delta \dot{m}_{air,exhaust}} \tag{3.19}$$

where, $\Delta \dot{m}_{supply}$ and $\Delta \dot{m}_{exhaust}$ is the difference between the measured inlet and outlet mass flow rates at supply and exhaust exchanger. $U_{\Delta \dot{m}_{air,supply}}$ and $U_{\Delta \dot{m}_{air,exhaust}}$ is the uncertainties in the mass flow rate difference and can be determined as (Beriault, 2009).

$$U_{\Delta \dot{m}_{air,supply}} = \left(\left(U_{\dot{m}_{air,1}} \right)^2 + \left(U_{\dot{m}_{air,2}} \right)^2 \right)^{1/2} \tag{3.20}$$

$$U_{\Delta \dot{m}_{air,exhaust}} = \left(\left(U_{\dot{m}_{air,3}} \right)^2 + \left(U_{\dot{m}_{air,4}} \right)^2 \right)^{1/2} \tag{3.21}$$

Water vapor balance/conservation of water vapor:

Water vapor balance (equation 3.22) also needs to be satisfied for the RAMEE system to reach steady-state condition (Simonson et al., 1999).

$$\Delta \dot{m}_{air} W_{air} = \left| \left(\dot{m}_{air,1} W_{air,1} - \dot{m}_{air,2} W_{air,2} \right) + \left(\dot{m}_{aiir,3} W_{air,3} - \dot{m}_{air,4} W_{air,4} \right) \right| \leq U_{\Delta \dot{m}_{air} W_{air}} \tag{3.22}$$

where, $U_{\Delta \dot{m}_{air} W_{air}}$ is the uncertainty in the net difference between the mass flow rate in and out of the exchanger ($\Delta \dot{m}_{air} W_{air}$) and is obtained as follows (Beriault, 2009).

$$U_{\Delta\dot{m}_{air}W_{air}} = \begin{pmatrix} \left(W_{air,1}U_{\dot{m}_{air,1}}\right)^2 + \left(\dot{m}_{air,1}U_{W_{air,1}}\right)^2 + \left(W_{air,2}U_{\dot{m}_{air,2}}\right)^2 + \left(\dot{m}_{air,2}U_{W_{air,2}}\right)^2 \\ + \left(W_{air,3}U_{\dot{m}_{air,3}}\right)^2 + \left(\dot{m}_{air,3}U_{W_{air,3}}\right)^2 + \left(W_{air,4}U_{\dot{m}_{air,4}}\right)^2 + \left(\dot{m}_{air,4}U_{W_{air,4}}\right)^2 \end{pmatrix}^{1/2} \quad (3.23)$$

Energy balance/conservation of energy:

In addition to mass balance and water vapor balance, energy balance also needs to be satisfied to reach steady-state condition (Simonson et al., 1999)

$$\Delta\dot{m}_{air}h_{air} = \left|\left(\dot{m}_{air,1}h_{air,1} - \dot{m}_{air,2}h_{air,2}\right) + \left(\dot{m}_{air,3}h_{air,3} - \dot{m}_{air,4}h_{air,4}\right)\right| \le U_{\Delta\dot{m}_{air}h_{air}} \quad (3.24)$$

where, $U_{\Delta\dot{m}_{air}h_{air}}$ is the uncertainty in the net difference between the energy in and out of the exchanger and is obtained as follows (Beriault, 2009).

$$U_{\Delta\dot{m}_{air}h_{air}} = \begin{pmatrix} \left(h_{air,1}U_{\dot{m}_{air,1}}\right)^2 + \left(\dot{m}_{air,1}U_{h_{air,1}}\right)^2 + \left(h_{air,2}U_{\dot{m}_{air,2}}\right)^2 + \left(\dot{m}_{air,2}U_{h_{air,2}}\right)^2 \\ + \left(h_{air,3}U_{\dot{m}_{air,3}}\right)^2 + \left(\dot{m}_{air,3}U_{h_{air,3}}\right)^2 + \left(h_{air,4}U_{\dot{m}_{air,4}}\right)^2 + \left(\dot{m}_{air,4}U_{h_{air,4}}\right)^2 \end{pmatrix}^{1/2} \quad (3.25)$$

If the conservation of energy is not satisfied, either the test is unsteady or a bias error in the experiment has not been accounted properly.

Effectiveness balances:

Another balance can be used to check the validity of the experimental measurements/results is the effectiveness of the supply and exhaust sides must agree within the uncertainty in the difference (Simonson et al., 1999)

$$\Delta\varepsilon_{o,sensible} = \left|\varepsilon_{o,sensible,(s)} - \varepsilon_{o,sensible,(e)}\right| \le U_{\Delta\varepsilon_{o,sensible}} \quad (3.26)$$

$$\Delta\varepsilon_{o,latent} = \left|\varepsilon_{o,latent,(s)} - \varepsilon_{o,latent,(e)}\right| \le U_{\Delta\varepsilon_{o,latent}} \quad (3.27)$$

$$\Delta\varepsilon_{o,total} = \left|\varepsilon_{o,total,(s)} - \varepsilon_{o,total,(e)}\right| \le U_{\Delta\varepsilon_{o,total}}, \quad (3.28)$$

Also, the uncertainty in the differences between the exhaust effectiveness and the supply effectiveness are calculated as follows (Beriault, 2008).

$$U_{\Delta\varepsilon_{o,sensible}} = \left(\left(U_{\varepsilon_{o,sensible,(s)}}\right)^2 + \left(U_{\varepsilon_{o,sensible,(e)}}\right)^2\right)^{1/2} \quad (3.29)$$

$$U_{\Delta\varepsilon_{o,latent}} = \left(\left(U_{\varepsilon_{o,latent,(s)}}\right)^2 + \left(U_{\varepsilon_{o,latent,(e)}}\right)^2\right)^{1/2} \tag{3.30}$$

$$U_{\Delta\varepsilon_{o,total}} = \left(\left(U_{\varepsilon_{o,total,(s)}}\right)^2 + \left(U_{\varepsilon_{o,total,(e)}}\right)^2\right)^{1/2} \tag{3.31}$$

3.8 Summary

In this chapter, air and solution properties required to evaluate RAMEE performance are identified. The value of mass flow rate of dry air ($\dot{m}_{air}$), h_{air}, W_{air} , T_{air}, T_{sol} are required before and after each exchanger. $\dot{m}_{air}$ is also required for supply and exhaust exchanger. The sensors used to measure these properties are also presented. Differential pressure transducers and orifice plates are used to measure $\dot{m}_{air}$. Humidity sensors and RTDs are used to measure W_{air}. Thermocouples are used to measure T_{air} and T_{sol}, and a rotometer is employed to measure q_{sol} to get the value of $\dot{m}_{sol}$. The calibration process of each sensor is also reported. The calibration curves providing the relationships between the calibrator (transfer standard) set points and the sensor outputs are found to be linear for all sensors.

The test facility (called RAMEETA) used to measure the required air and solution properties using the calibrated sensors are presented in detail. The data acquisition system is also discussed. During the experiments, the signal outputs from the sensors are time averaged and then converted into the pressure, temperature and RH, applying the calibration curves.Bias and precision errors of different sensors are calculated from the calibration data. Total uncertainties of the sensors are determined based on the ASME PTC 19.1 1998 standard using the 95% confidence interval and reported in Table 3-2.

The uncertainty in the calculated parameters due uncertainty in the measured parameters is also discussed. Finally, mathematical expressions for the uncertainty in the

overall supply and exhaust exchanger effectiveness are provided. Uncertainty in the calculated effectiveness values ranges from 2% to 45% for the maximum and minimum air-flow rate of the test facility.

CHAPTER 4
EXPERIMENTAL RESULTS

4.1 Introduction

In this chapter, the performance of the counter-cross-flow RAMEE system, which was designed in chapter 2, is evaluated using the RAMEETA (described in chapter 3). Performance is quantified with three different overall effectiveness values: a) sensible, b) latent and c) total (equation 1.2) at AHRI summer and AHRI winter conditions.

Both transient and steady-state/quasi steady-state effectiveness values are presented. Transient performance of the RAMEE system is important because in some locations the outdoor weather may change drastically in only a few hours. RAMEE system should be able to react quickly in those conditions to avoid low performance. On the other hand, steady-state/quasi steady-state performance is important to assess the economic feasibility of the RAMEE system.

4.2 Test conditions

To evaluate the performance (i.e. effectiveness) of the RAMEE system, tests are conducted at various NTUs and desiccant solution to air capacitance ratios (C_{sol}/C_{air}).The different NTUs are created by varying the air-flow rate through each LAMEE and different C_{sol}/C_{air} values are created by varying the solution-flow rate of $MgCl_2$ while keeping the air-flow rate constant.

Flow configuration

Two different desiccant solution-flow configurations are considered in the tests, a) top-to-bottom and b) bottom-to-top. In the top-to-bottom flow configuration, the

desiccant solution flows from the top header to the bottom header (Figure 3-11). On the other hand, in the bottom-to-top flow configuration the desiccant solution flows from the bottom header to the top header due to pump pressure.

The bottom-to-top flow configuration is expected to provide better effectiveness values because the desiccant solution will flow more uniformly through the LAMEE in this case due to a higher liquid pressure (Erb, 2007) than in the top-to-bottom flow configuration. Therefore, most of the tests are conducted with the bottom-to-top flow configuration. However, some of the tests are also repeated with the top-to-bottom flow configuration to verify if the bottom-to-top flow configuration is better.

Heat loss/gain effect

Heat loss/gain effect of the RAMEE system with the surroundings is investigated by repeating some of the tests after adding extra layer of insulations. The heat loss/gain effect is discussed in detail in Section 4.6.

Different NTUs and C_{sol}/C_{air}

Summer and winter tests are conducted for different NTUs varying from 3.8 to 12.1 and C_{sol}/C_{air} varying from 1.0 to 5.0 when the supply and exhaust inlet conditions are close to the AHRI summer/winter conditions. The pumping rates of the desiccant solution are varied from 0.006 L/s to 0.059 L/s (0.1 to 0.94 GPM, US Gallons). The face velocity is varied from 0.71 m/s to 2.14 m/s (141 fpm to 422 fpm). Figure 4-1(a and b) shows supply inlet (SI_{air}) and exhaust inlet (EI_{air}) conditions for both the AHRI (summer and winter) and actual experimental conditions superimposed on a psychrometric chart. Equilibrium solution concentrations for magnesium chloride ($MgCl_2$) are also shown in

the Figure 4-1. The NTU and C_{sol}/C_{air} of each test are calculated based on the SI_{air} and SI_{sol} properties (Figure 3-8).

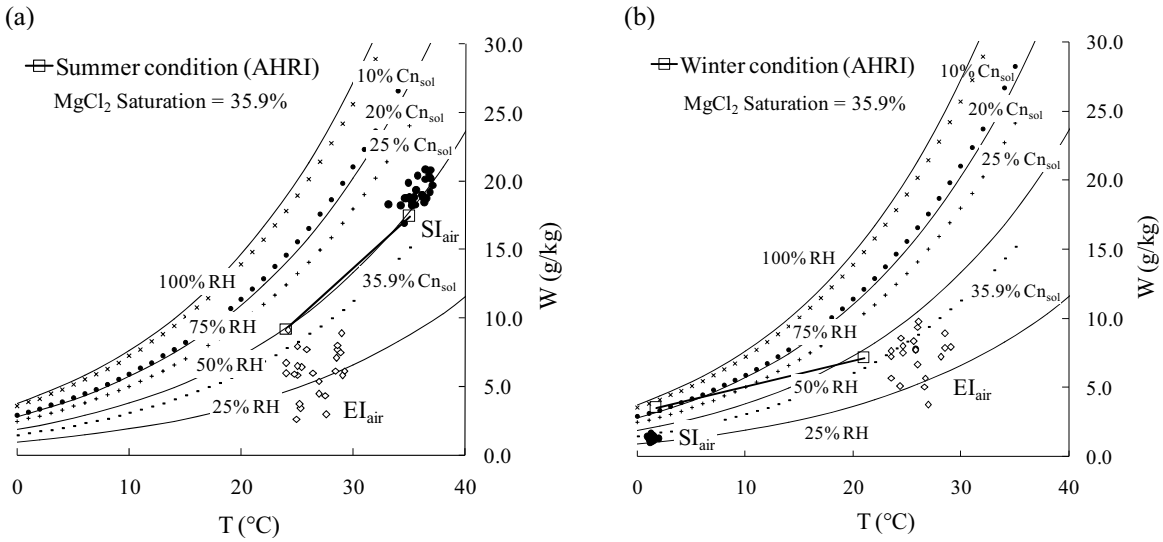

Figure 4-1. AHRI and experimental a) summer and b) winter test conditions superimposed on a psychrometric chart along with equilibrium solution concentration for $MgCl_2$

From Figure 4-1, it is evident that the supply (SI_{air}) and exhaust (EI_{air}) inlet experimental conditions (summer and winter) are slightly different than AHRI conditions. The SI_{air} is closer to the AHRI test condition from the EI_{air} because the SI_{air} is drawn from the environmental chamber while EI_{air} is drawn from the laboratory room which is conditioned by the building HVAC system.

Experimental conditions for each test (summer and winter) are also tabulated in Table 4-1 and 4-2. Each test is recognized by NTU value, C_{sol}/C_{air} ratio and number of the test. For example, "$Test_1$, NTU = 1, C_{sol}/C_{air} = 1" represents Test 1 which is carried out at NTU value of 1 and at C_{sol}/C_{air} ratio of 1.

Table 4-1. Summer experimental test conditions

Test index	NTU	C_{sol}/C_{air}	Experimental measurements								
			Solution -flow rate (GPM)	Temperature (^oC)		RH (%)		Dry air mass flow rate (kg/s)		Face velocity (m/s)	
				1	3	1	3	1	3	1	3
Desiccant solution-flow : bottom-to-top											
1	12.0	1.3	0.10	34.3	24.2	0.52	0.52	0.013	0.014	0.71	0.71
2	12.1	1.9	0.13	34.9	25.0	0.55	0.32	0.013	0.014	0.71	0.71
3	12.0	2.9	0.21	34.6	24.0	0.52	0.38	0.013	0.014	0.71	0.65
4	12.0	4.5	0.32	33.2	24.0	0.56	0.34	0.013	0.013	0.71	0.65
5	8.5	1.0	0.10	36.1	25.4	0.49	0.34	0.019	0.019	1.01	0.95
6	8.5	1.6	0.17	34.7	25.0	0.53	0.43	0.018	0.019	1.01	0.95
7	8.5	2.8	0.28	35.4	24.9	0.51	0.35	0.019	0.019	1.01	0.95
8	8.5	5.0	0.50	35.5	24.7	0.50	0.32	0.019	0.019	1.01	0.95
9	6.9	1.1	0.13	37.0	26.9	0.52	0.26	0.023	0.023	1.25	1.19
10	7.2	1.7	0.21	35.0	25.8	0.52	0.40	0.023	0.024	1.19	1.19
11	6.9	2.9	0.35	35.5	26.9	0.50	0.21	0.023	0.023	1.25	1.19
12	6.9	4.7	0.57	36.5	26.4	0.53	0.30	0.023	0.024	1.25	1.19
13	4.0	1.3	0.28	36.5	28.5	0.52	0.31	0.040	0.041	2.14	2.14
14	4.0	2.0	0.43	36.4	28.6	0.48	0.33	0.040	0.041	2.14	2.08
15	4.0	3.0	0.10	36.8	28.9	0.49	0.32	0.040	0.042	2.14	2.14
16	4.0	4.5	0.13	37.1	28.9	0.49	0.38	0.040	0.041	2.14	2.14
Desiccant solution-flow: top-to-bottom											
32	7.9	3.3	0.4	34.5	25.3	0.49	0.18	0.021	0.021	1.09	1.06
33	7.9	6.0	0.6	35.3	25.2	0.50	0.20	0.021	0.021	1.09	1.07
34	7.9	8.7	0.9	35.3	24.9	0.50	0.14	0.021	0.021	1.09	1.07
35	5.6	2.3	0.4	36.2	27.6	0.49	0.14	0.029	0.031	1.55	1.56
36	5.5	4.2	0.6	36.7	27.5	0.51	0.20	0.029	0.031	1.58	1.56
Desiccant solution-flow : bottom-to-top , extra insulation											
39	4.1	1.3	0.3	35.7	29.0	0.55	0.25	0.039	0.041	2.12	2.10
40	4.1	1.3	0.3	36.6	28.4	0.48	0.27	0.039	0.041	2.12	2.09
41	4.1	3.1	0.6	36.3	28.6	0.49	0.35	0.039	0.040	2.10	2.09
42	4.1	4.4	0.9	36.9	29.2	0.51	0.26	0.039	0.041	2.12	2.10

Table 4-2. Winter experimental test conditions

Test index	NTU	C_{sol}/C_{air}	Solution -flow rate (GPM)	Experimental measurements							
				Temperature (^oC)		RH (%)		Dry air mass flow rate (kg/s)		Face velocity (m/s)	
				1	3	1	3	1	3	1	3
Desiccant solution-flow : bottom-to-top											
17	3.8	1.2	0.3	1.2	28.5	0.50	0.39	0.043	0.041	2.02	2.12
18	3.8	2.0	0.5	1.5	29.1	0.46	0.34	0.044	0.042	2.04	2.15
19	3.8	2.8	0.6	1.3	28.5	0.46	0.34	0.043	0.041	2.01	2.12
20	3.8	4.1	0.9	1.4	28.1	0.45	0.32	0.044	0.041	2.02	2.12
21	6.9	1.0	0.1	1.2	26.0	0.42	0.34	0.024	0.023	1.12	1.18
22	6.9	1.6	0.2	1.0	26.0	0.45	0.47	0.024	0.023	1.12	1.18
23	6.9	2.8	0.4	1.0	26.0	0.47	0.49	0.024	0.023	1.12	1.17
24	6.8	4.4	0.6	1.2	25.6	0.45	0.43	0.025	0.023	1.14	1.19
26	8.3	1.6	0.1	1.6	24.6	0.43	0.41	0.020	0.019	0.93	0.98
27	8.2	2.3	0.2	1.4	24.6	0.42	0.44	0.020	0.019	0.94	0.96
28	8.3	4.8	0.5	1.9	24.4	0.38	0.29	0.020	0.019	0.93	0.97
29	11.5	1.3	0.1	1.3	23.6	0.34	0.34	0.015	0.014	0.67	0.70
30	11.8	2.8	0.2	1.5	23.5	0.37	0.43	0.014	0.014	0.66	0.69
31	11.5	4.2	0.3	1.4	23.5	0.38	0.45	0.014	0.014	0.67	0.69
Desiccant solution-flow : bottom-to-top , extra insulation											
43	6.9	1.1	0.1	1.3	26.6	0.38	0.25	0.024	0.023	1.11	1.17
44	6.9	1.6	0.2	1.1	26.9	0.33	0.18	0.024	0.023	1.11	1.18
45	6.9	2.8	0.4	1.0	26.7	0.39	0.28	0.024	0.023	1.12	1.17

4.3 Test procedures

Before each test, the air in the environmental chamber is conditioned to be close to either AHRI summer or winter condition. It takes about 2-3 hours for the environmental chamber to reach close to the AHRI conditions. All the vacuum fans (Figure 3-8) are operated and solution-flow pumps (SP) are closed during this time. Transient air properties at supply inlet (T_1, RH_1) and exhaust inlet (T_3, RH_3) are monitored by the DAQ system (chapter 3) at this time. Once these inlet conditions reach close to the AHRI condition, the two desiccant solution pumps are switched on and data collection is started

immediately. This time is considered as the beginning time/initial condition (t = 0) of the test.

Once the test is started, each test is carried out until the RAMEE system reaches steady-state conditions or the properties of air and desiccant solution changes very little with time. After recording the transient data, steady-state/quasi steady-state effectiveness values of the RAMEE system at the end of the tests are calculated.

4.4 Typical transient performance of the counter-cross-flow RAMEE system

4.4.1 Summer testing

One of the summer tests data ($Test_3$, NTU = 12.0 and C_{sol}/C_{air} = 2.9) is presented in this section to illustrate the transient RAMEE performance. Table 4-3 shows the test conditions of $Test_3$.

Table 4-3. Conditions of $Test_3$

Parameters	*Values with uncertainty*
NTU	12.0± 0.8
C_{sol}/C_{air}	2.9±0.2
$\dot{m}_{air,supply}$ (kg/s)	0.0136 (±.0008)
$\dot{m}_{air,exhaust}$ (kg/s)	0.0133 (±.0008)
T_1,RH_1 (SI_{air})	34.6^{o}C (±0.2), 52% (±1.2%)
T_3,RH_3 (EI_{air})	24 ^{o}C (±0.2), 38% (±1.2%)
V_{face} (m/s)	0.71 (±0.04)
q_{sol} (SI_{sol}) L/s	0.013 (±0.001)

For the summer AHRI condition, warm and humid air enters at the supply inlet (T_1) and room air enters at the exhaust inlet (T_3) and flows through the air channels of the exchangers and exits at temperatures T_2 and T_4. Desiccant solution enters both the exchangers at 22.6^{o}C at t = 0. At the supply exchanger, warm and humid air loses heat and moisture to the desiccant solution and at the exhaust exchanger room air gains heat and moisture from the circulating desiccant solution.

At the beginning of the test (t = 0) air transfer less amount of heat and moisture to desiccant solution as the desiccant solution first enters the liquid panels of the exchangers. With increasing time the liquid panels are filled with desiccant solution and circulate through the RAMEE system. It is observed that the transport time needed for the desiccant solution to go from the inlet to the outlet header is 17 minutes. Thermal and moisture capacitance effects are higher at this initial stage. As a result, ΔT and ΔW increase sharply at the supply and exhaust exchangers for about 36 minutes as shown in Figure 4-2.

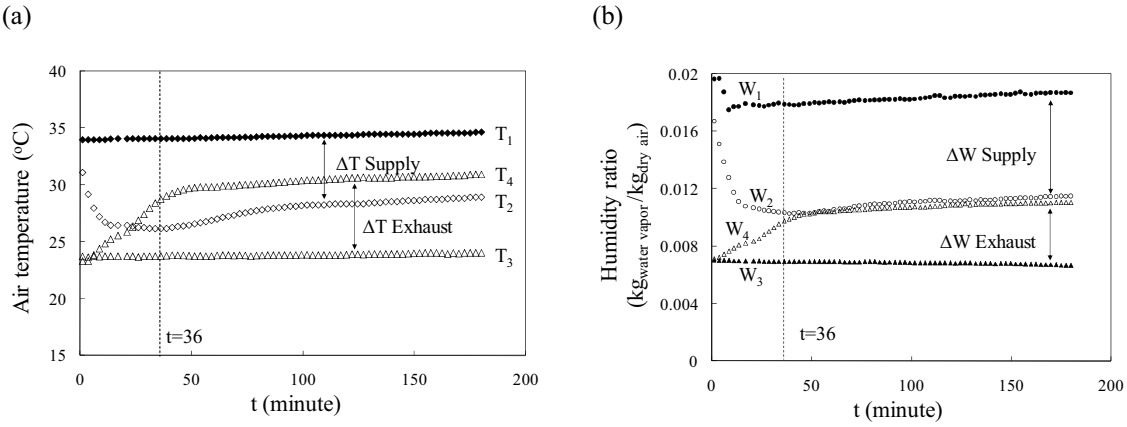

Figure 4-2. Transient air temperature and humidity ratio during summer condition ($Test_3$, NTU = 12.0, C_{sol}/C_{air} = 2.9)

Initially the heat and moisture transfer at the exhaust exchanger is lower than the supply exchanger because the solution (which enters both the exchangers at 22.6°C), gains more heat and moisture at the supply exchanger than the exhaust exchanger due to higher heat and moisture transfer potential at supply exchanger (SI_{air}: T_1 = 34.6°C, W = 0.018) than the exhaust exchanger (EI_{air}: T_3 = 24°C, W = 0.006).

As the experiment progress, the desiccant solution temperature and moisture are elevated from its initial conditions as it gains more heat and moisture at the supply

exchanger than it lose at exhaust exchanger. Due to the increase of solution temperature and moisture content the heat and mass transfer potential between air and solution decreases at the supply exchanger and increases at the exhaust exchanger. As a result, ΔT supply and ΔW supply decrease and ΔT exhaust and ΔW exhaust increase with time. At the end of the test ΔT supply and ΔT exhaust are found to be almost equal, however, ΔW supply is found to be much higher than ΔW exhaust.

Figure 4-3 (a and b) shows the sensible and latent effectiveness (equation 1.2) of $Test_3$. During the test, the air properties at the supply inlet (T_1, W_1) and exhaust inlet (T_3, W_3) change very little with time (Figure 4-2). Therefore, the sensible and latent effectiveness changes based on the heat and mass transfer potential at the supply and exhaust exchangers (i.e. ΔT and ΔW).

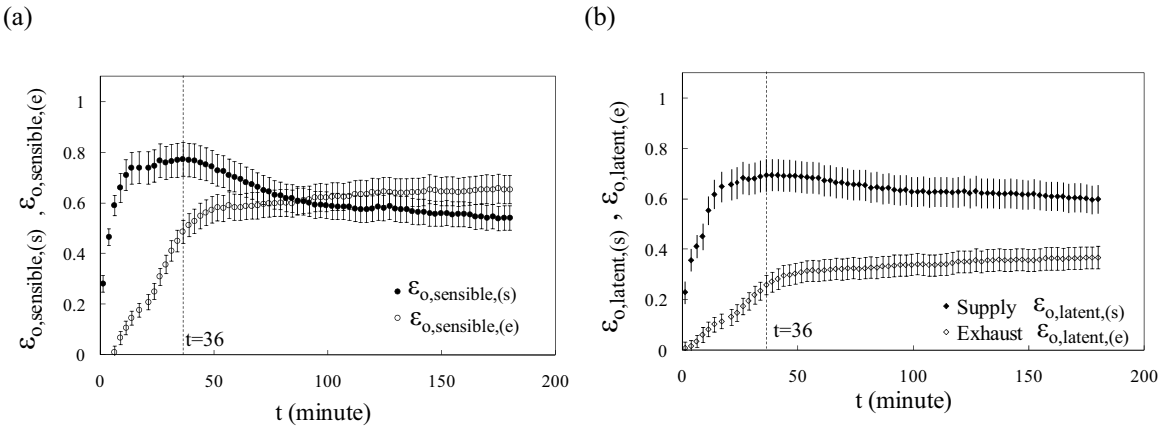

Figure 4-3. Transient sensible a) and latent b) effectiveness during summer condition ($Test_3$, NTU = 12.0, C_{sol}/C_{air} = 2.9)

At t = 0, desiccant solution just enters into the exchangers and as a result ΔT and ΔW are found to be low. Sensible and latent effectiveness are also observed low. With time, the supply sensible and latent effectiveness increase sharply and reach a peak ($\varepsilon_{o,sensible,(s)}$

= 0.77 and $\varepsilon_{o,latent,(s)}$ = 0.69 at t = 36 minute) due to highest potential heat transfer with the initial solution.

Exhaust sensible and latent effectiveness also increases sharply initially (at t = 36, $\varepsilon_{o,sensible,(e)}$ = 0.49, $\varepsilon_{o,latent,(e)}$ = 0.27). With time the effectiveness increases slowly at the exhaust exchanger because after the initial capacitance effect the temperature and moisture transfer in the exhaust exchanger increases due to the warm desiccant solution that is delivered from the supply exchanger.

Figure 4-4 shows the total effectiveness of $Test_3$. Total effectiveness (Figure 4-4) shows similar trends as sensible and latent effectiveness. Initially both the effectiveness are low. As the test proceeds, the $\varepsilon_{o,total,(s)}$ increases to a peak value due to higher heat and moisture transfer potential at initial condition. After reaching a peak value $\varepsilon_{o,total,(s)}$ decreases with time. On the other hand, $\varepsilon_{o,total,(e)}$ increases initially due to higher heat and moisture transfer potential at initial condition and then increases very slowly with time. However, for time greater than (t = 87), the effectiveness values change very little with time.

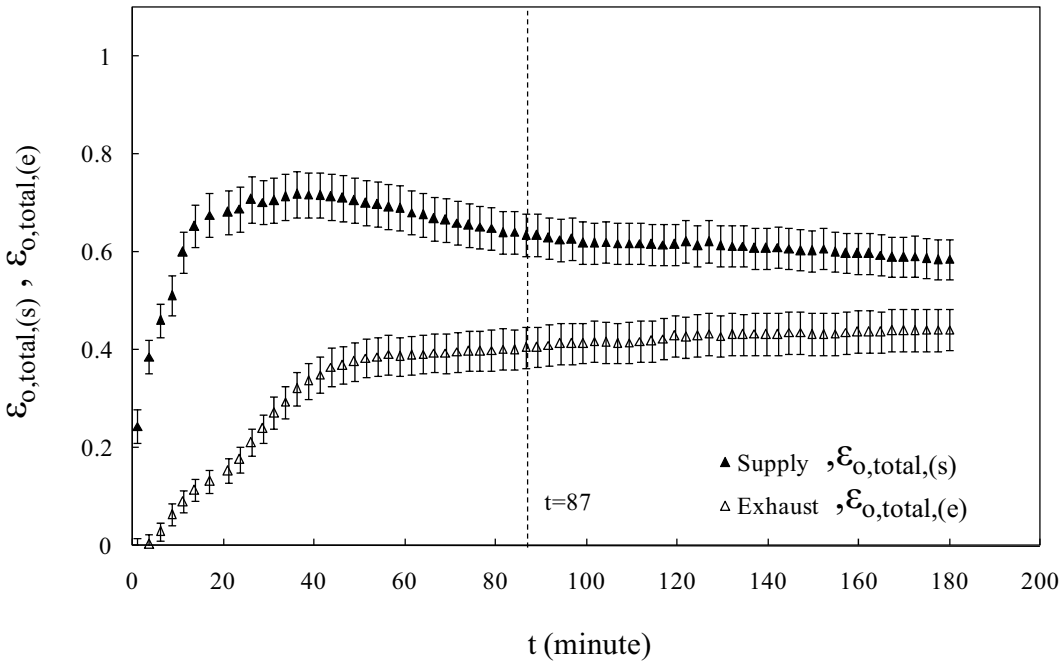

Figure 4-4. Transient total effectiveness during summer condition ($Test_3$, NTU = 12.0, C_{sol}/C_{air} = 2.9)

Although effectiveness and air properties are almost constant at the end of the test (i.e. 180 minutes, Figure 4-2 to 4-4) only conservation of dry air (equation 3.20), is satisfied ($\Delta \leq U_{\Delta}$ is yes for $\dot{m}_{air,supply}$ and $\dot{m}_{air,exhaust}$, Table 4-4) within experimental uncertainties. However, conservation of water vapor ($\dot{m}_{air} W_{air}$, equation 3.23) and energy ($\dot{m}_{air} h_{air}$, equation 3.24) are not satisfied within experimental uncertainties as reported in Table 4-2. Effectiveness balances (equation 3.29 to 3.31) are also not found within the uncertainty limit, which indicates that the RAMEE system has not reach steady-state conditions at the end of the test.

Table 4-4. Conservation of dry air, water vapor, energy and effectiveness balance at the end of the experiment for $Test_3$

	Δ	*Uncertainties in differences , U_Δ*	$\Delta \leq U_\Delta$	*Steady-state or transient*
$\Delta \dot{m}_{air,supply}$	0.000780	0.001157	Yes	steady
$\Delta \dot{m}_{air,exhaust}$	0.000357	0.001157	Yes	steady
$(\Delta \dot{m}_{air} W_{air}, kg/s)$,	5.4E-05	2.2E-05	No	transient
$(\Delta \dot{m}_{air} h_{air}, W)$	0.16	0.10	No	transient
$\Delta \varepsilon_{o,sensible}$	0.16	0.09	No	transient
$\Delta \varepsilon_{o,latent}$	0.26	0.08	No	transient
$\Delta \varepsilon_{o,total}$	0.08	0.07	No	transient

Psychrometric analysis

Heat and moisture transfer processes, which will be taking place in the RAMEE system, can easily be understood by plotting the inlet and outlet air properties (SI_{air}, EI_{air}) of the exchangers on a psychrometric chart. Figure 4-5 shows the psychrometric chart for $Test_3$ at the end of the test.

During summer testing, the temperature and humidity of the supply air (SI_{air}) decrease as the air loses heat and moisture to the cool and dry desiccant solution in the supply exchanger. As a result, the temperature and humidity of the supply air outlet (SO_{air}) are lower than the inlet air (SI_{air}). On the other hand, the air temperature and humidity increase inside the exhaust exchanger as the exhaust air gains heat and moisture from the warm and dilute desiccant solution delivered from the supply exchanger.

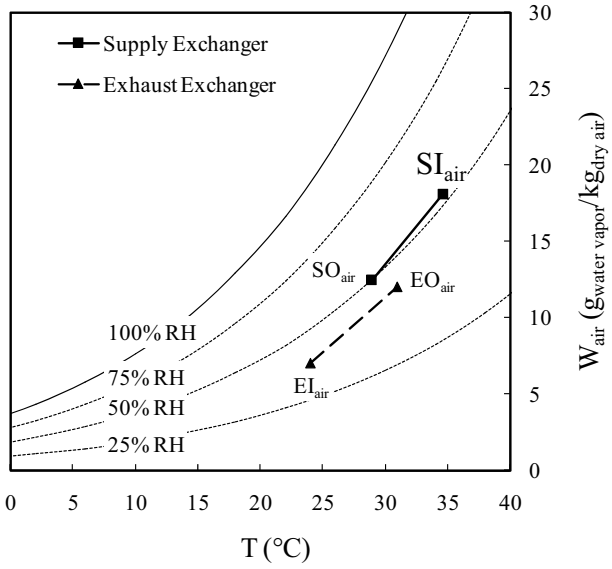

Figure 4-5. Inlet and outlet air properties of the supply and exhaust exchangers on a psychrometric chart at the end of the experiment for $Test_3$ (NTU = 12.0, C_{sol}/C_{air} = 2.9)

4.4.2 Winter testing

During the winter tests, cold and dry air flows through the supply exchanger and room air flows though the exhaust exchanger. Supply air gains moisture and heat from the solution, whereas exhaust air losses moisture and heat to the desiccant solution. This section presents the typical nature of winter test results by presenting results from one of the winter tests. Table 4-5 shows the test conditions of $Test_{30}$.

Table 4-5. Test conditions of $Test_{30}$

Parameters	*Values with uncertainty*
NTU	11.8± 0.8
C_{sol}/C_{air}	2.8±0.2
$\dot{m}_{air,supply}$ (kg/s)	0.0138 (±.0008)
$\dot{m}_{air,exhaust}$ (kg/s)	0.0137 (±.0008)
T_1,RH_1 (SI_{air})	1.5°C (±0.2), 37% (±1.2%)
T_3,RH_3 (EI_{air})	23.5 °C (±0.2), 43% (±1.2%)
V_{face} (m/s)	0.66 (±0.04)
q_{sol} (SI_{sol}) L/s	0.013 (±0.001)

Figure 4-6 shows the transient effectiveness (sensible, latent and total) values obtained during $Test_{30}$. The supply exchanger effectiveness is found to be higher than the exhaust exchanger at the beginning of the test (t = 0). This may be mostly due to heat gain to the supply air from the surroundings and mass transfer to the dry air from the leaked solution inside the exchanger.

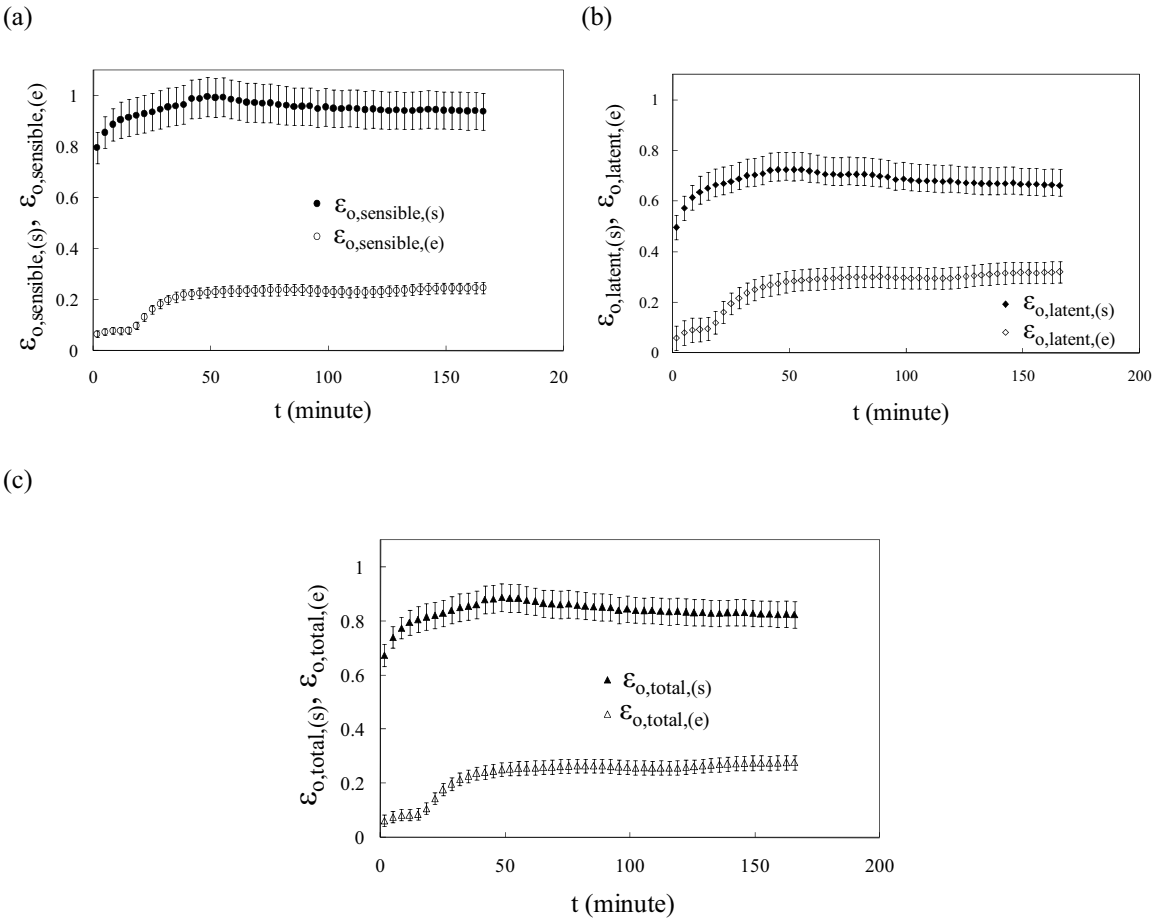

Figure 4-6. Transient effectiveness a) sensible b) latent and c) total during winter test condition ($Test_{30}$, NTU = 11.8, C_{sol}/C_{air} = 2.8)

All the effectiveness values increase initially with a higher rate due to higher heat and moisture transfer to the supply air. After that it decreases slightly at the supply exchanger as the heat and moisture transfer rates between air and solution decrease while circulating

through the RAMEE system. On the other hand, the effectiveness values at the exhaust exchanger increase slightly as the cool and dry solution from the supply exchanger enters into exhaust exchanger and increases heat and moisture transfer potential.

This trend continues as the test proceeds. To investigate if the RAMEE system reaches steady-state condition; conservation of dry air, water vapor, energy and effectiveness balances are calculated (Table 4-6) at the end of the test. Conservation of dry air is within the uncertainty limit but the conservation of water vapor and energy are outside the uncertainty bound. The effectiveness differences ($\Delta\varepsilon_{o,sensible} = 0.69$, $\Delta\varepsilon_{o,latent} = 0.34$, $\Delta\varepsilon_{o,total} = 0.27$) are larger than the uncertainty limits ($U_{\Delta\varepsilon_{o,sensible}} = 0.08$, $U_{\Delta\varepsilon_{o,latent}} = 0.08$, $U_{\Delta\varepsilon_{o,total}} = 0.06$). Transient effectiveness difference, and transient water vapor and energy at the end of the test indicate that the RAMEE system is not yet reached steady-state condition.

Table 4-6. Conservation of dry air, water vapor, energy and effectiveness balance at the end of the experiment for $Test_{30}$

	Δ	*Uncertainties in differences , U_Δ*	*Steady-state or transient*
$\Delta\dot{m}_{air,supply}$	0.000583	0.000053	steady
$\Delta\dot{m}_{air,exhaust}$	0.000053	0.001157	steady
$(\Delta\dot{m}_{air} W_{air}, kg/s)$	2.74E-05	9.7111E-06	transient
$(\Delta\dot{m}_{air} h_{air}, W)$	0.273644	0.05357892	transient
$\Delta\varepsilon_{o,sensible}$	0.69	0.08	transient
$\Delta\varepsilon_{o,latent}$	0.34	0.08	transient
$\Delta\varepsilon_{o,total}$	0.27	0.06	transient

The conditions at the end of the $Test_{30}$ can be better visualized by plotting the inlet and exit air properties of the exchangers on a psychrometric chart (Figure 4-7). Since

$\dot{m}_{air,supply} \approx \dot{m}_{air,exhaust}$ (Table 4-3) the lengths of the lines would be equal. Since the exhaust air line is much shorter, the energy transfer is much lower in the exhaust exchanger than in the supply exchanger.

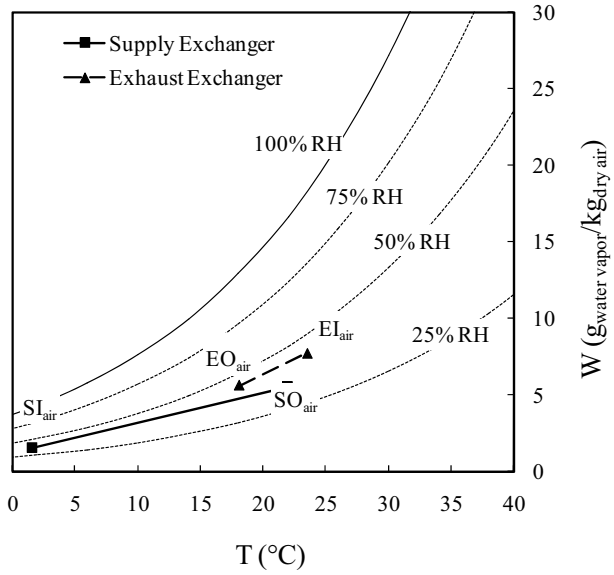

Figure 4-7. Inlet and outlet air properties of the supply and exhaust exchangers on a Psychrometric chart at the end of the experiment for $Test_{30}$ (NTU = 11.8, C_{sol}/C_{air} = 2.8)

4.4.3 Summary of transient summer and winter test results

From the effectiveness and psychrometric analysis for a typical summer and winter tests it is found that the RAMEE system does not reach steady-state conditions even though the air temperature, solution temperature and air humidity ratio become nearly constant at the end of the experiment after a run of about 180 minutes. As a result, we cannot use the effectiveness values of the individual exchanger but we may be able to use the average effectiveness or RAMEE effectiveness ($\varepsilon_{o,sensible}$, $\varepsilon_{o,latent}$, $\varepsilon_{o,total}$, equation 1.4). The following section will address this with the help of transient simulation results carried out by Seyed Ahmadi (2008).

4.5 Transient simulated effectiveness of a cross-flow RAMEE system

Since a transient numerical model for a counter-cross-flow RAMEE system is not available, the transient results in this section will be for a cross-flow RAMEE. Seyed Ahmadi (2008) developed a numerical model to investigate the transient behavior of a cross-flow RAMEE system. The study showed that the initial desiccant solution concentration ($Cn_{sol,initial}$) mass of the desiccant solution, heat loss/gain in between the exchangers (Q_{be}) of the solution with the surrounding has significant impacts on the transient response of the RAMEE system. Seyed Ahmadi (2008) introduced a dimensionless heat loss/gain coefficient (σ_{sol}), which is based on solution properties defined for the supply exchanger as,

$$\sigma_{sol,supply} = \frac{Q_{be,supply}}{\left| C_{sol,6} T_{sol,6} - C_{sol,5} T_{sol,5} \right|} \tag{4.1}$$

where, C_{Sol} is the heat capacity rate of desiccant solution. The numbers 5 and 6 indicate the position of temperature and C_{sol} (Figure 3-8). Negative values of σ indicate heat loss from the system, while heat gain to the system results in a positive coefficient. Heat loss/gain (Q_{be}) from the desiccant solution is described as it flows from the outlet of one exchanger to the inlet of the other exchanger. For example, $Q_{be,supply}$ for the supply side includes heat/loss gain in the a) exhaust exchanger outlet header, b) supply exchanger inlet header, c) supply reservoir, d) desiccant solution piping connecting the outlet header of the exhaust exchanger to the inlet header of the supply exchanger and the e) pump SP-1 (Figure 4-8).

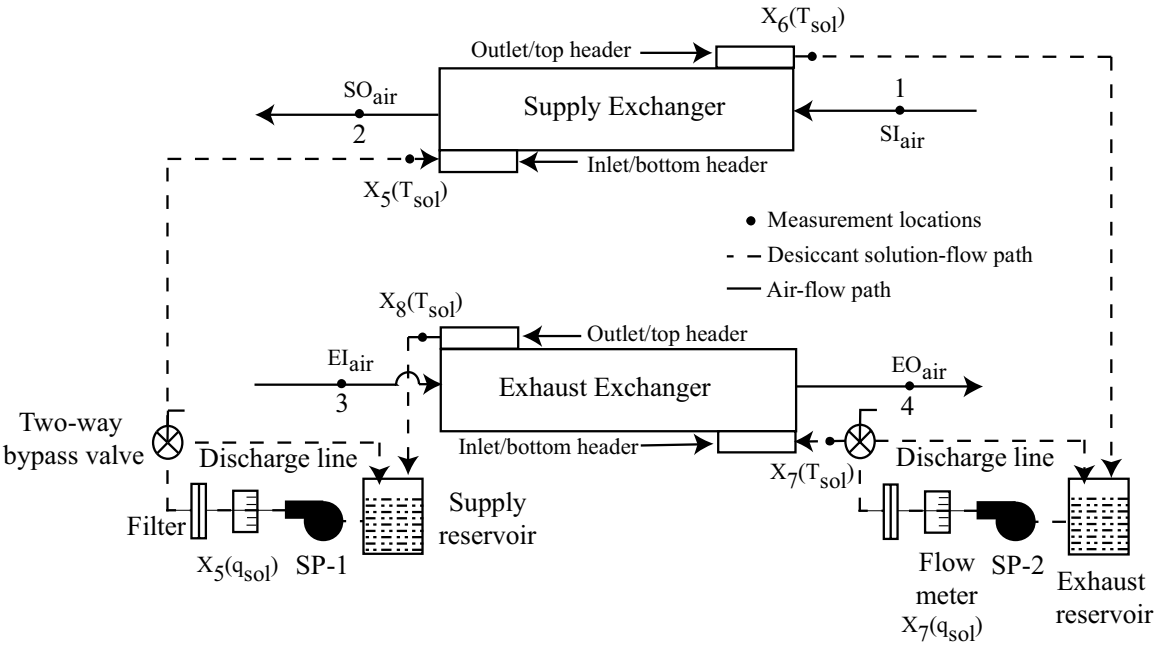

Figure 4-8. Different components at the air and solution-flow path of the RAMEE system

He introduced another dimensionless parameter to consider the effect of the mass of desiccant solution in the system, defined as

$$\lambda = \frac{\text{Mass of desiccant solution in the exchangers}}{\text{Total mass of desiccant solution in the system}} \tag{4.2}$$

The mass of solution in the RAMEE system includes exchangers, headers, piping and storage tanks. He introduced another parameter to account the effect of desiccant solution concentration change from the steady-state condition. The parameter is defined as,

$$\Delta Cn = Cn_{sol,initial} - Cn_{sol,steady\text{-}state} \tag{4.3}$$

Figure 4-9 (Seyed Ahmadi, 2008) shows the effect of solution mass to reach steady-state condition of the RAMEE system at AHRI summer and winter conditions. It is observed that, when the mass of the solution is increased in the RAMEE system, more solution circulation is required to reach the steady-state condition.

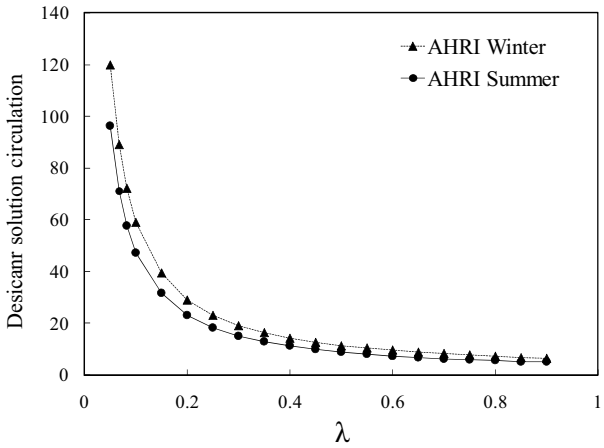

Figure 4-9. Change in the number of desiccant solution circulations to reach quasi steady-state condition for the RAMEE system due to different size of storage tanks for AHRI operating conditions (NTU = 5, C_{sol}/C_{air} = 3, σ = 0, ΔCn = 0), (Seyed Ahmadi, 2008, Figure 4-11)

Figure 4-10a (Seyed Ahmadi, 2008) shows the effect of heat loss/gain on the effectiveness values of a RAMEE system. It is found that the heat loss/gain effect increases the difference between the supply and exhaust exchanger effectiveness values. However, the average effectiveness does not vary once the RAMEE system has reached a quasi steady-state condition.

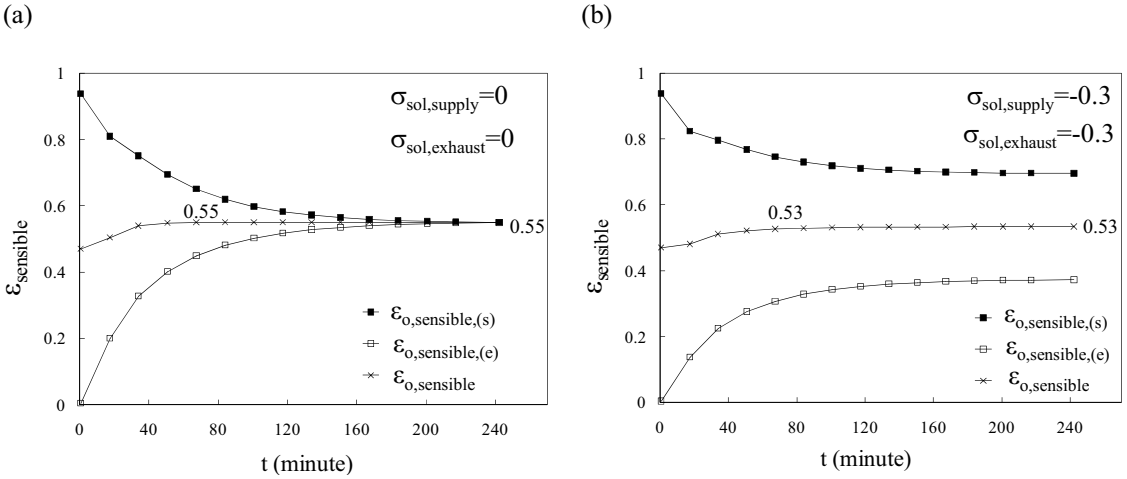

Figure 4-10. Transient sensible effectiveness of the RAMEE system a) without heat loss b) with heat loss for AHRI summer operating conditions (NTU = 5, C_{sol}/C_{air} = 3, λ = 0.15, and ΔCn = 0), (Seyed Ahmadi, 2008, Figure 4-12a)

For example when, $\sigma_{sol,supply} = \sigma_{sol,exhaust} = 0$ (i.e. no heat loss at the supply and exhaust exchangers) and $\Delta Cn = 0$ (i.e. no concentration difference of the desiccant solution), system reaches steady-state at t = 240 minutes. But when $\sigma_{sol,supply} = \sigma_{sol,exhaust} = -0.3$ and $\Delta Cn = 0$, the difference between supply and exhaust exchanger sensible effectiveness is around 0.20 at t = 240 (Figure 4-10b). However, the average effectiveness becomes constant once it reaches a quasi steady-state condition (e.g. at $\sigma_{sol} = -0.3$, $\varepsilon_{o,sensible} = 0.53$ and at $\sigma_{sol} = 0$, $\varepsilon_{o,sensible} = 0.55$).

Figure 4-11 shows the effect of solution concentration difference for the AHRI winter condition. When $\Delta Cn = 0$ and $\sigma_{sol} = 0$, the sensible effectiveness reaches a steady-state condition at 300 minutes. Effectiveness difference of 0.20 is found at t = 300 minutes when $\Delta Cn = 7.6\%$ (Figure 4-10b). However, average effectiveness values are found constant once the RAMEE system has reached quasi steady-state condition.

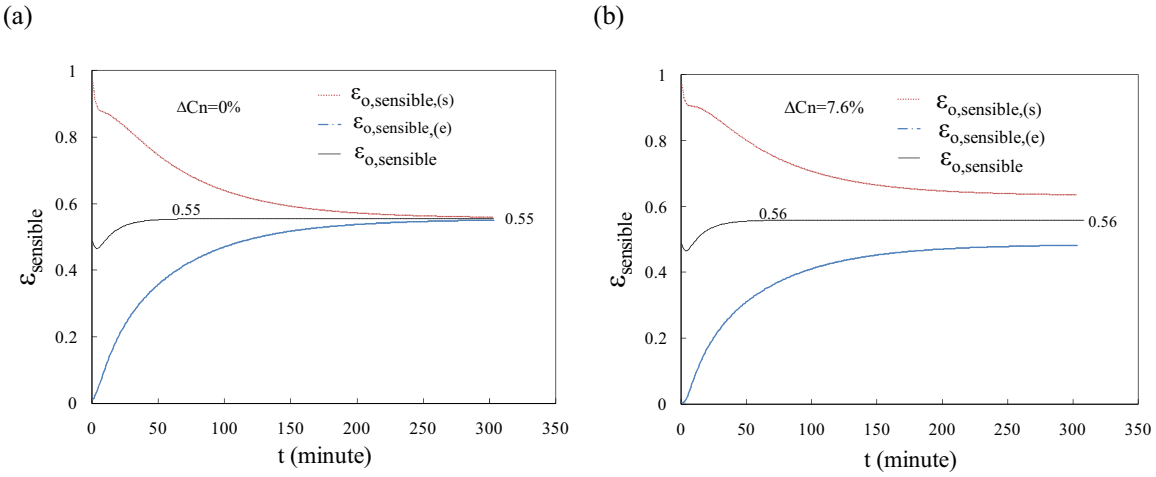

Figure 4-11. Sensible effectiveness variation with time for AHRI winter condition with a) $\Delta Cn = 0.0\%$, b) $\Delta Cn = 7.6\%$ at (NTU = 5, $C_{sol}/C_{air} = 3$, $\lambda = 0.15$, $\sigma_{sol} = 0$), (Seyed Ahmadi, 2008, Figure 4-18a)

The above study showed that the transient average effectiveness fluctuates at the beginning of the simulation. However, once the system effectiveness reaches a quasi steady-state condition, the transient average effectiveness maintains a nearly constant value untill the end of the experiment (Figure 4-10 and 4-11). Therefore, the average effectiveness value of the RAMEE system at a quasi steady-state condition could be used for reporting the performance of the RAMEE system. A quasi steady-state condition of the test for this study is defined as follows,

$$\varepsilon_{\text{quasi steady-state}} = \varepsilon_{x,t+10} - \varepsilon_{x,t} \leq 1\% \tag{4.4}$$

In equation (4.4), x is the sensible, latent or total effectiveness and t is the time (minute) of the test. Equation (4.4) shows that if the difference in effectiveness during a 10 minute time interval is less than or equal to 1% then the RAMEE system could be said to have reached a quasi steady-state condition. This is also evident from Figure 4-10 and 4-11. Experimental results also show a similar trend. Figure 4-12 shows the average total effectiveness during summer ($Test_3$) and winter ($Test_{30}$) change about 1% once they have reached a quasi steady-state condition.

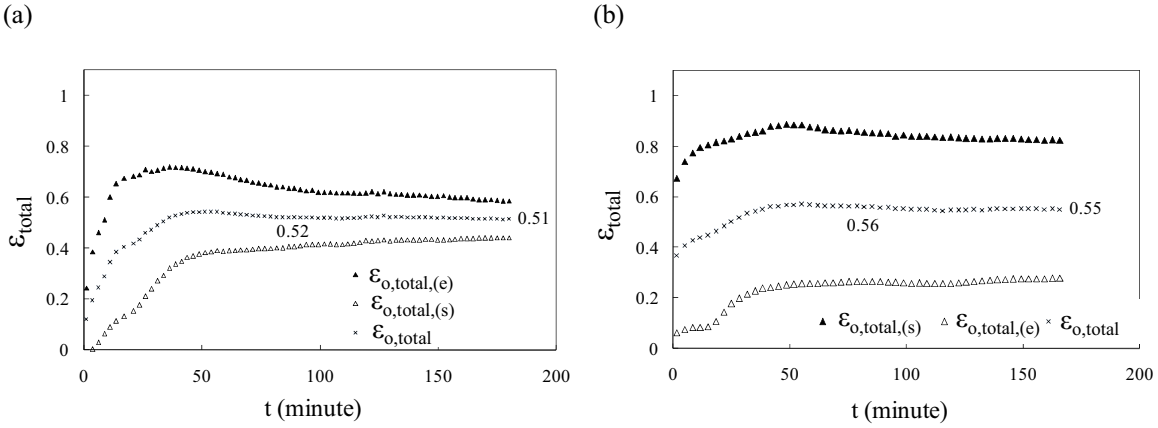

Figure 4-12. Total effectiveness variation with time for a) AHRI summer ($Test_3$) b) AHRI winter ($Test_{30}$) conditions

4.6 Heat loss/gain

4.6.1 Summer

It is found in the cross-flow simulation result that the external heat loss/gain of the RAMEE system introduces a difference between supply and exhaust exchanger effectiveness values. As the difference is also found in the experimental effectiveness values, the influence of external heat loss/gain on the RAMEE system performance is investigated experimentally.

In order to investigate the effects of heat loss/gain, the insulation of the exchangers is improved and some of the experiments are repeated. Extra insulation layers are added on some uncovered surfaces of the exchangers as well as on the existing insulations of the test setup. Approximately, the conduction resistance value of the piping insulation is increased from 0.50 K/W to 0.55 K/W (10% increase) and the conductive resistance value of the exchanger wall insulation is increased 36%.

Figure 4-13 shows the effect of the extra layer of insulation by representing the air and solution temperature for $Test_{41}$ and $Test_{15}$ at the end of the test. Figure 4-13 shows that heat loss through piping and exchanger wall are reduced after adding the extra insulation. For example, the supply exchanger temperature difference (ΔT_{12}) is reduced from 6.7^{o}C to 5.5^{o}C with the extra insulation which indicates that the extra layer of insulations is minimizing the heat loss.

(a)

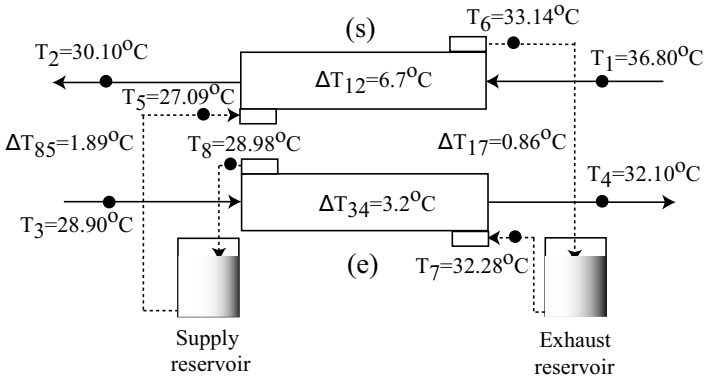

(b)

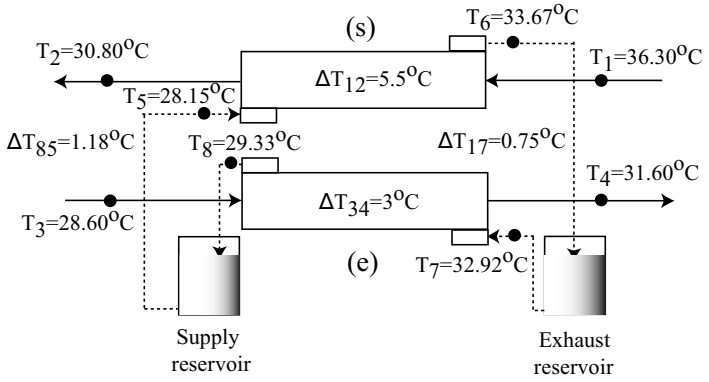

Figure 4-13. Air and desiccant solution temperature during summer condition at t = 73 minutes (NTU ≈ 4, $C_{sol}/C_{air} \approx 3$) a) before extra insulation, $Test_{15}$ b) after extra insulation, $Test_{41}$

The recovered heat with the extra insulation, which would be lost, otherwise, reduces the temperature differences between the desiccant solution and the air temperatures at the supply exchanger and increases at the exhaust exchanger. Thus, the sensible effectiveness at the supply exchanger is reduced, but it is increased at the exhaust exchanger. Due to these effects, $\Delta\varepsilon_{o,sensible}$ is reduced at the end of the test (t = 73) (Figure 4-14).

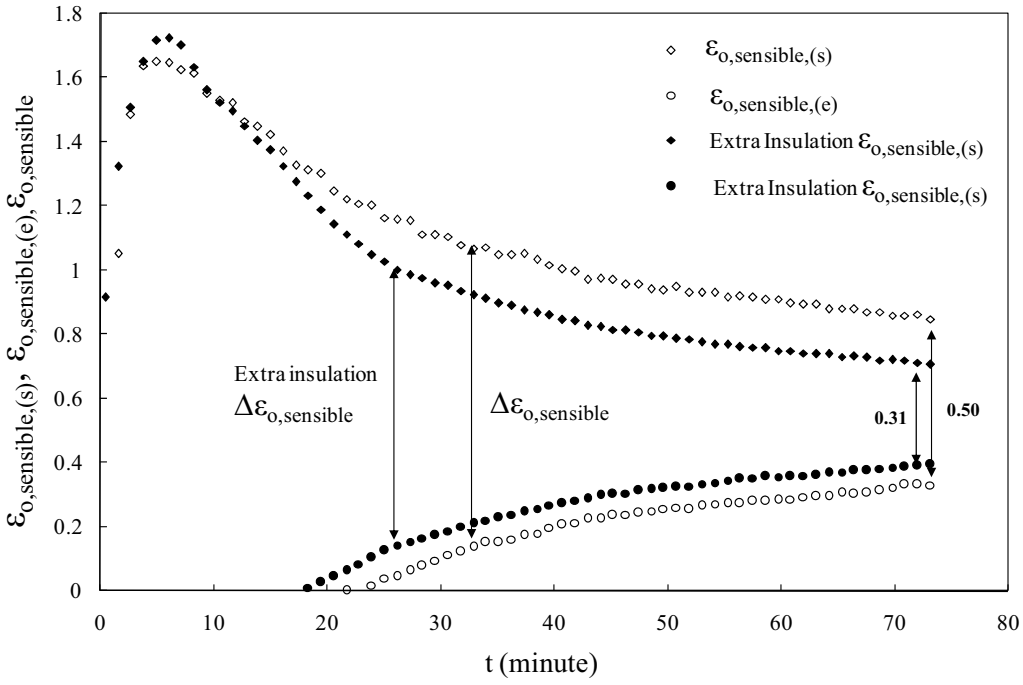

Figure 4-14. Transient sensible effectiveness before and after extra insulation during summer testing condition ($Test_{41}$ and $Test_{15}$, NTU = 4, $C_{sol}/C_{air} \approx 3$)

The above study indicates that reducing the heat loss/gain of the RAMEE system by adding extra insulation during the summer test condition reduces the difference between $\varepsilon_{o,sensible,(s)}$ and $\varepsilon_{o,sensible,(e)}$ and the time to reach quasi steady-state. A similar trend is also observed from numerical results by Seyed Ahmadi (2008) shown in Figure 4-10.

Heat loss/gain amount

The heat loss/gain is estimated for different sections/components of the RAMEE system for $Test_{41}$. More specifically, the heat loss/gain amount between the exchanger and its surroundings is estimated for each exchanger (Q) and in between exchanger (Q_{be}). For the supply exchanger, Q_{supply} includes the heat loss/gain from the supply reservoir, SP-1, transitions, inlet and outlet headers of the supply exchanger and exchanger wall (Figure 4-8). Similarly for the exhaust exchanger, $Q_{exhaust}$ includes the heat

loss/gain amount from the exhaust reservoir, SP-1, transitions, the exchanger wall and the inlet and the outlet headers of the exhaust exchanger. On the other hand, Q_{be} is defined in Section 4.5.

After estimating the heat loss/gain amount from different sections of the RAMEE system, they are compared with the total energy transfer amount (considering air enthalpy change) of each exchanger using equations (4.5) and (4.6). The equations are presented based on the supply side. Table 4-7 shows the results of the heat loss/gain analysis for $Test_{41}$.

$$\alpha_{supply} = \frac{Q_{supply}}{\dot{m}_{air,2} h_{air,2} - \dot{m}_{air,1} h_{air,1}} \tag{4.5}$$

$$\sigma_{air,supply} = \frac{Q_{be,supply}}{\dot{m}_{air,2} h_{air,2} - \dot{m}_{air,1} h_{air,1}} \tag{4.6}$$

Table 4-7. Amount of heat loss from the RAMEE system ($Test_{41}$)

	Supply	*Exhaust*
Q (W)	-33.78	-46.6
α	-0.04	-0.12
σ_{air}	-0.02	-0.08

Table 4-5 shows that heat losses ($Q = 46.6$ W, and $\alpha = 0.12$) are greater on the exhaust side than on the supply side ($Q = 33.78$ W, and $\alpha = 0.04$) because the exhaust exchanger reservoir and piping receive heated desiccant solution from the supply exchanger which transfers more amount of energy with the surroundings. It should be noted that the surroundings are close to exhaust air temperature conditions.

It is also observed that a significant amount of the heat loss occurs through the piping and reservoir (which is described by σ_{air}). If the length of piping of the RAMEE system

is large, which is expected in buildings where the supply and exhaust exchangers are not side-by-side, the heat transfer through the piping walls will increase significantly.

4.6.2 Winter

Figure 4-15 presents winter test results before and after the extra insulation (NTU = 6.9, C_{sol}/C_{air} = 2.8) and shows that heat loss/gain is present in the winter testing. Recovered heat due to improved insulation reduces the difference between the supply and exhaust effectiveness and also changes the system effectiveness.

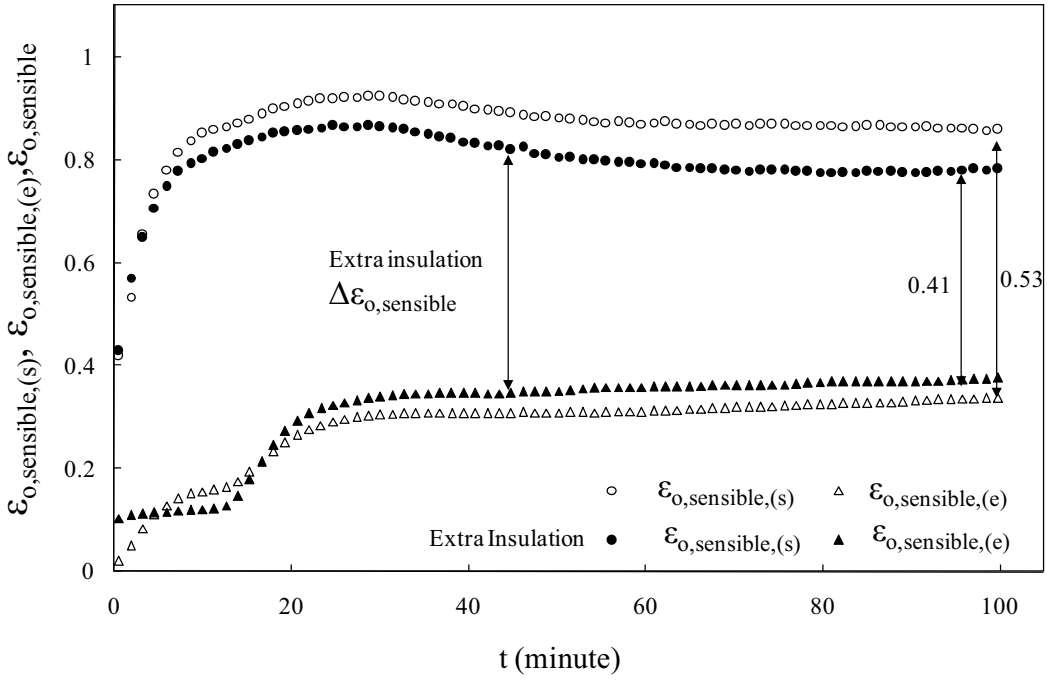

Figure 4-15. Sensible effectiveness before ($Test_{23}$, NTU = 6.9, C_{sol}/C_{air} = 2.8) and after ($Test_{45}$, NTU = 6.9, C_{sol}/C_{air} = 2.8) extra insulation

The sensible effectiveness difference $\Delta\varepsilon_{o,sensible}$ is decreased from 0.53 to 0.41 at the end of the test. The heat loss/gain amount from different components of the RAMEE system is also estimated (equations 4.5, 4.6) for $Test_{45}$ and tabulated in Table 4-8. The positive sign indicates that heat is gained from the surroundings.

Table 4-8. Amount of heat gain of the RAMEE system ($Test_{45}$)

	Supply Exchanger	*Exhaust exchanger*
Q (W)	44	58
α	0.07	0.23
σ_{air}	0.02	0.20

4.6.3 Summary of heat loss/gain

The above analysis shows that there is still a significant amount of heat loss/gain present in the RAMEE system even after the extra layer of insulation. Therefore, more insulation is warranted to reduce the heat loss/gain and reduce the effectiveness difference between supply and exhaust exchanger. Due to heat loss/gain the single exchanger effectiveness may not be used to report the RAMEE effectiveness but the average effectiveness for the supply and exhaust values can be used to report RAMEE effectiveness as shown in Section 4.5.

4.7 Other considerations

4.7.1 Effect of desiccant solution-flow configuration

The effect of desiccant solution-flow configuration is investigated by comparing the total effectiveness values ($\varepsilon_{o,total}$) of the RAMEE system with a) top-to-bottom and b) bottom-to-top flow configurations: Figure 4-16 shows the total effectiveness values varying with C_{sol}/C_{air} at NTU = 7 (bottom-to-top) and 7.9 (top-to-bottom). In both cases, the effectiveness is low at low C_{sol}/C_{air} and increases as C_{sol}/C_{air} increases. For high values of C_{sol}/C_{air}, the effectiveness is nearly constant with increasing value of C_{sol}/C_{air} in the system. Figure 4-16 shows that the top-to-bottom flow configuration has lower effectiveness than the bottom-to-top flow configuration.

This is because, in the top-to-bottom flow configuration, some places inside the liquid panels may not be filled or may not have the same mass flow per unit area with the

desiccant solution which may reduce the heat and mass transfer rate between air and desiccant solution. That is, liquid flow mal-distribution will reduce the effectiveness. In the bottom-to-top flow configuration, those empty or low flow regions are filled with the desiccant solution resulting in an increase in the effectiveness values. Mal-distribution of the liquid flow will have a smaller effect for bottom-to-top liquid flows, especially when C_{sol}/C_{air} is small.

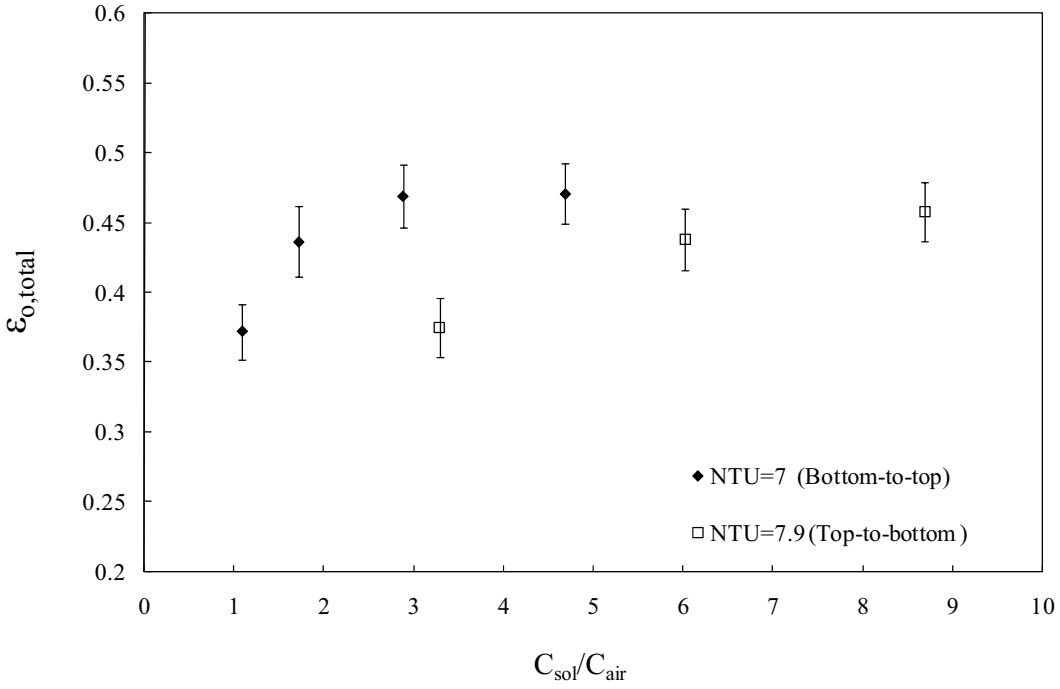

Figure 4-16. RAMEE total effectiveness comparison between top-to-bottom and bottom-to-top desiccant solution-flow configuration

Figure 4-16 shows that, in the bottom-to-top flow configurations, lower C_{sol}/C_{air} values are needed to fill the panel volume of the exchanger with desiccant solution due to higher solution pressure than in the top-to-bottom flow configuration. This trend is evident in Figure 4-16 where the total effectiveness becomes apparently constant for bottom-to-top flow after $C_{sol}/C_{air} = 3$. In the case of top-to-bottom flow (NTU = 7), an

increasing trend is observed even at C_{sol}/C_{air} = 9. One cannot conclude that mal-distribution effects do not exist beyond C_{sol}/C_{air} = 9. It can be said that the direction of flow through each exchanger is not important for $C_{sol}/C_{air} > 9$.

4.7.2 Effect of transient solution-flow rate

Each summer and winter test is carried out with a constant C_{sol}/C_{air} ratio and NTU value. This procedure does not reflect the effects of transient C_{sol}/C_{air} on the effectiveness values of the RAMEE system. The heat and moisture transfer rates in a RAMEE system could be controlled by changing the flow rate of the desiccant solution. To investigate this control strategy, an experiment is conducted at NTU = 8.5 for the bottom-to-top flow configuration at the AHRI summer condition. The C_{sol}/C_{air} value is varied from 5 to 2.8 during the experiment once the RAMEE system has reached a quasi steady-state condition.

Changes of C_{sol}/C_{air} from 5 to 2.8 have a smaller effect on the average effectiveness, but decreases to 0.9 reduce effectiveness. This is consistent with Figure 4-16 and other research (Fan 2006, Seyed Ahmadi 2008, Vali 2009). At a C_{sol}/C_{air} value of 5, the supply sensible effectiveness value is observed to be nearly constant at around 0.60 (t = 184) and it is increased to 0.64 (t = 264) when the C_{sol}/C_{air} value is 2.8 (Figure 4-17a). This trend is expected for the sensible effectiveness because with lowering the C_{sol}/C_{air} value, the mass flow rate decreases and $\varepsilon_{o,sensible,(s)}$ increases. However, when the C_{sol}/C_{air} value is reduced to 0.9 the sensible effectiveness value decreases due to low heat transfer potential at low solution-flow rate. Similar behavior is observed at the exhaust exchanger with varying C_{sol}/C_{air} (Figure 4-17).

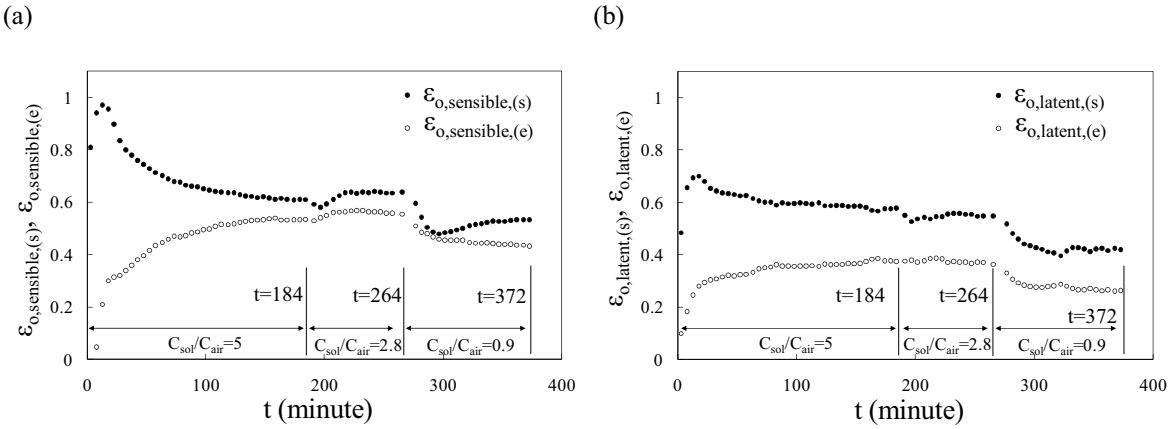

Figure 4-17. Effect of desiccant solution-flow rate change on a) sensible b) latent effectiveness values during summer condition ($Test_{55}$, NTU = 8.5, C_{sol}/C_{air} = 5, 2.8, 0.9)

In case of latent effectiveness $\varepsilon_{o,latent,(s)}$ and $\varepsilon_{o,latent,(e)}$ are higher at high C_{sol}/C_{air} (0.58 at t = 184 and C_{sol}/C_{air} = 5) and gradually decreases with low C_{sol}/C_{air} values (0.42 at t = 372 and C_{sol}/C_{air} = 0.9, Figure 4-16b). The trend is expected as the increased desiccant solution-flow rate at high C_{sol}/C_{air} values increases the latent effectiveness. Latent effectiveness decreases at low C_{sol}/C_{air} value due to low moisture transfer potential (ΔW) caused by the low solution flow rate.

Total effectiveness shows the combined effect of sensible and latent effectiveness (Figure 4-18). $\varepsilon_{o,total,(s)}$ decreases from 0.59 to 0.45 with changing C_{sol}/C_{air} from 5 to 0.9. Whereas $\varepsilon_{o,total,(e)}$ decreases from 0.41 to 0.30. The study indicates the transient C_{sol}/C_{air} will affect the quasi steady-state condition of the RAMEE system and effectiveness values.

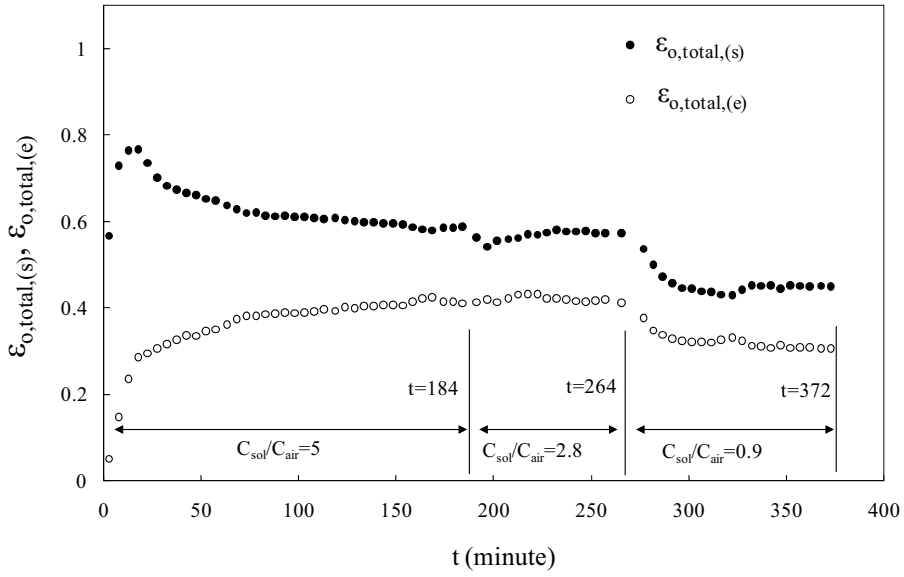

Figure 4-18. Effect of desiccant solution-flow rate change on total effectiveness values during summer condition ($Test_{55}$, NTU = 8.5, C_{sol}/C_{air} = 5, 2.8, 0.9)

4.8 Quasi steady-state effectiveness of the RAMEE system

This section reports the quasi steady-state (equation 4.4) RAMEE effectiveness values for summer and winter conditions for all the tests. Sensible, latent, and total effectiveness of the RAMEE system for summer and winter tests are plotted as a function of C_{sol}/C_{air} values for different NTUs in Figure 4-19 and the results are tabulated in Appendix-C. Effectiveness values are also plotted against face velocity (V_{face}). Figure 4-19 shows that, the effectiveness values (sensible, latent and total) are low at low C_{sol}/C_{air} be and increasing with increasing C_{sol}/C_{air}. The Effectiveness values are found to be quite insensitive to NTU. The sensible effectiveness values are higher for both summer (a maximum value of 0.66) and winter (a maximum value of 0.62) conditions than the latent effectiveness values (maximum value of 0.50 for summer and 0.49 for winter conditions). In case of total effectiveness, the maximum value during summer test condition is 0.53

(NTU = 12. and C_{air}/C_{sol} = 4.5). In case of winter conditions, a peak total effectiveness of 0.55 is found (NTU = 11.8, C_{sol}/C_{air} = 2.8).

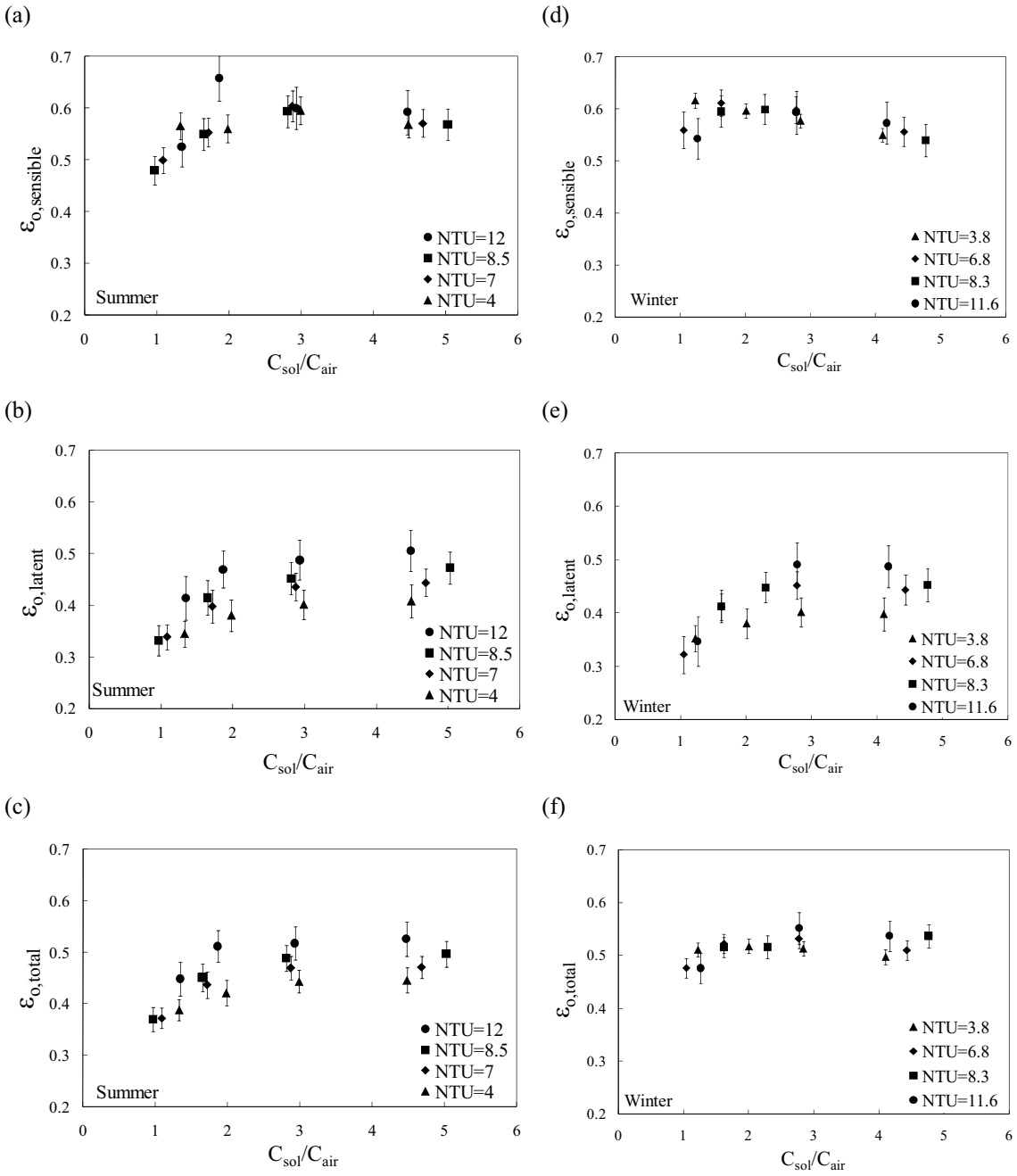

Figure 4-19. Quasi steady-state RAMEE effectiveness (sensible , latent and total) for summer and winter testing

Figure 4-20 shows the effect of face velocity on quasi steady-state total effectiveness values at different C_{sol}/C_{air} ratios.

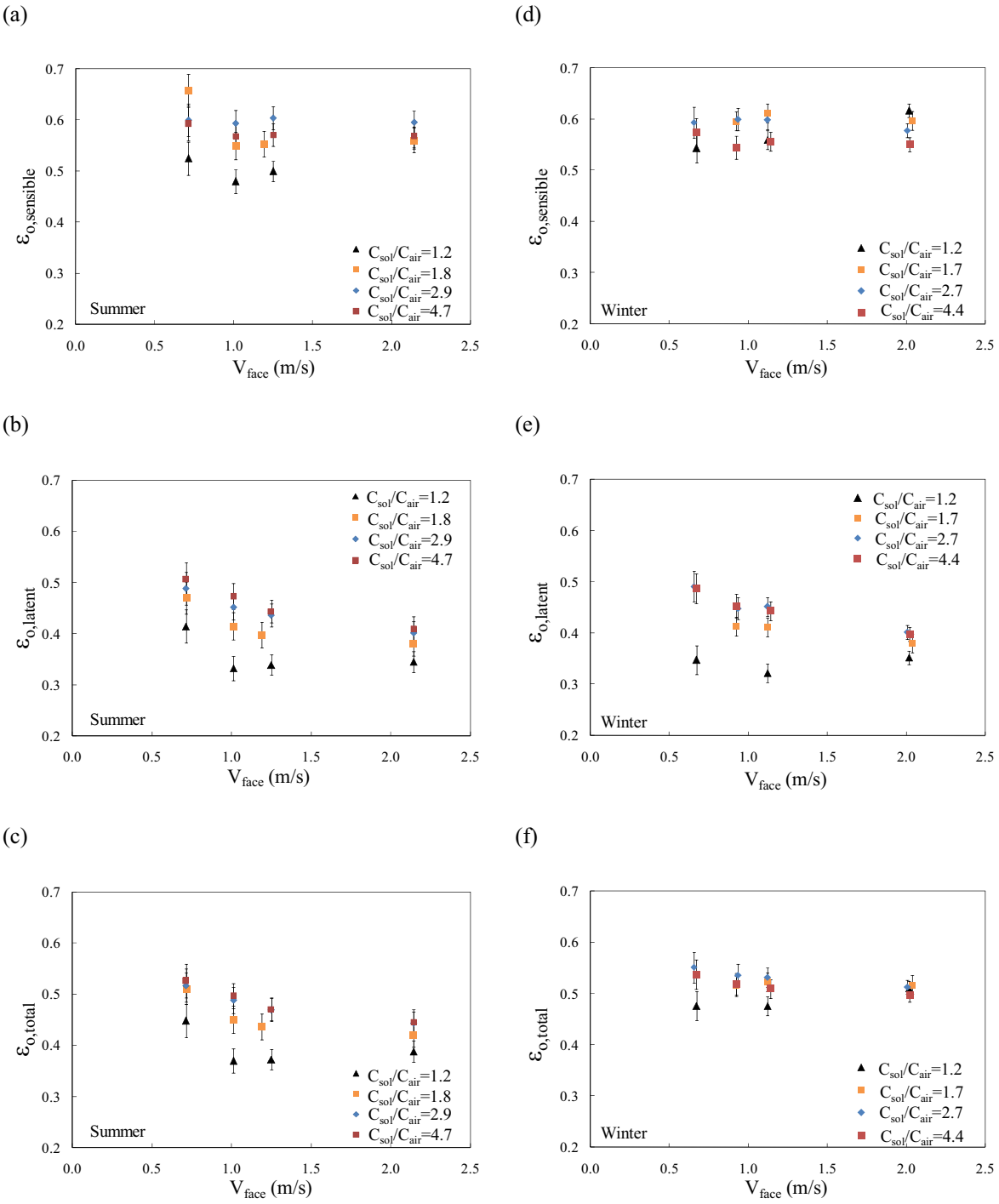

Figure 4-20. Quasi steady-state RAMEE total effectiveness varying with V_{face} and C_{sol}/C_{air}

Figure 4-20 shows that total effectiveness values decrease with increasing V_{face} and decreasing $C_{sol}/C_{air.}$ At the target V_{face} (2 m/s), the RAMEE effectiveness is found lower than the designed value (0.65).The lower effectiveness than the designed value (0.65 of overall effectiveness) may be due to the use of heat transfer based correlation in the LAMEE design process, heat loss/gain effects in the experiments, mal-distributed desiccant solution-flow in the experiment, desiccant solution leakage in the experiment.

Vali (2009) shows that for the current RAMEE system with the Propore^{TM} membrane around NTU of 12 is required to achieve 65% overall effectiveness in comparison to NTU of 4.5 used in the current design. However, in order to achieve NTU = 12 more membrane surface area is required. This will result in more liquid panels and more fan power to maintain face velocity of 2 m/s. Instead of increasing membrane surface area another option would be to search for a better membrane with higher water vapor permeability. This is also evident from the test results. Figure 4-19(a) and (d) shows that maximum sensible effectiveness is found close to the design value (around 0.60). Lower than design effectiveness indicates heat loss/gain in the system. Seyed Ahmadi (2008) also showed that heat/loss gain reduce the overall effectiveness of the RAMEE system.

In case of the latent effectiveness, RAMEE system reaches around 0.40 at around 2 m/s. Latent effectiveness can be increased by using a micro-porous membrane with the higher permeability value. Future investigations are warranted in this issue to improve the RAMEE performance. Lower latent effectiveness is lowering the total effectiveness of the RAMEE system which is found to be 0.45 (C_{sol}/C_{air} = 4.7) for summer and 0.50 (C_{sol}/C_{air} = 4.4) for winter condition at V_{face} = 2 m/s.

The other two possible reasons (mal-distributed desiccant-flow and desiccant solution leakage) is better understood when the results are compared with numerical results. Therefore, these two issues are discussed in chapter 5.

4.9 Summary

In this chapter, test results for the counter-cross-flow RAMEE performance are presented near the AHRI summer and winter conditions for various NTU and C_{sol}/C_{air} values. The experimental test conditions are found slightly different from the AHRI conditions especially for the exhaust inlet air properties.

Typical summer and winter test data are presented as a function of time to describe the transient behavior of the RAMEE system. From the typical test data, it is found that the RAMEE system does not reach steady-state conditions even though the air temperature, solution temperature and air humidity ratio become nearly constant at the end of the experiment. However, once the system reaches quasi steady-state condition, average effectiveness change very little with time. Thus RAMEE effectiveness are reported as the average of supply and exhaust exchanger effectiveness at quasi steady-state condition.

It is also found from the typical test data and the numerical simulation data of a cross-flow RAMEE system that significant heat loss/gain is present in all the tests. Therefore heat loss/gain effects are investigated for both the summer and winter test conditions by adding extra layer of insulations. It is found that extra layer of insulation reduces $\Delta\varepsilon_{o,\,sensible}$ and reduces the time to reach quasi steady-state

The quasi steady-state system effectiveness values (sensible, latent and total) are reported for both summer and winter test conditions. The maximum total effectiveness

($\varepsilon_{o,\,total}$) of the RAMEE system for the summer condition testing is found to be 0.53 at NTU 12 and C_{sol}/C_{air} = 4.5. In case of winter condition testing, the maximum total effectiveness is found 0.55 (NTU = 11.8, C_{sol}/C_{air} = 2.8).

The total effectiveness of the RAMEE at 2 m/s is found to be 0.45 (C_{sol}/C_{air} = 4.7) for summer and 0.50 (C_{sol}/C_{air} = 4.4) for winter conditions, which is lower than the design target (65%) based on heat transfer only and described in Chapter 2. This suggests that the current design method which is based on heat transfer correlations is not accurate for designing the RAMEE system. The RAMEE system design based on numerical simulation described in section 2.2.4.2 may be used for future RAMEE design. Other possible reasons may be due to heat loss/gain effects in the experiments, lower than expected water vapor permeability of the membrane, mal-distributed desiccant solution-flow in the experiment and desiccant solution leakage in the experiment.

CHAPTER 5
COUNTER-CROSS-FLOW RAMEE PERFORMANCE COMPARISONS

5.1 Introduction

In this chapter, the experimental effectiveness values ($\varepsilon_{o,sensible}$, $\varepsilon_{o,latent}$ $\varepsilon_{o,total}$) of the counter-cross-flow RAMEE system are compared with predicted effectiveness values obtained from the numerical model developed by Vali (2009). Only summer tests are considered as Vali (2009) reported numerical effectiveness values of the summer tests only. The experimental effectiveness of the counter-cross-flow RAMEE system is also compared with the experimental effectiveness of a cross-flow RAMEE system (Erb, 2007) for both summer and winter operating conditions to investigate counter-cross-flow RAMEE system performance compared to cross-flow RAMEE system performance.

5.2 Comparison between experimental and numerical effectiveness values (summer tests)

In this section, experimental and numerical (Vali, 2009) effectiveness values for the counter-flow RAMEE system are compared for summer operating conditions. Table 5-1 tabulates different parameters which are used in the numerical model (Vali, 2009).

Table 5-1. Parameters used in the numerical model (Vali, 2009)

Parameters	*Values*	*Comments*
Supply inlet temperature	35°C	AHRI summer
Supply Inlet RH	49%	test condition
Exhaust inlet temperature	24°C	
Exhaust inlet RH	49.5%	
Desiccant solution	$MgCl_2$	
Exchanger dimensions	$1.8 \times 0.2 \times 0.086$ m	
Average air-flow gap gap, $t_{air,avg}$	4.4 mm	
Average liquid panel gap , $t_{sol,avg}$	2.7 mm	
Membrane	Propore™	
Membrane thickness, t_{mem}	0.2 mm	Mike Larson (2007)
Membrane thermal conductivity	0.334 W/m	Mike Larson (2007)
Number of heat transfer units (NTU)	4 to12	
Membrane permeability (K_m)	16.6 x 10-7(kg/m.s)	Mike Larson (2007)

As shown in Table 5-1, AHRI summer test conditions are used in the numerical model; while the experimental conditions are slightly different than AHRI summer conditions due to limitation in setting the exhaust inlet air temperature and humidity ratio in the RAMEETA (chapter 4).

Vali (2009) carried out sensitivity analysis and showed that sensible $(\varepsilon_{o,sensible})$ and latent $(\varepsilon_{o,latent})$ effectiveness of the RAMEE system changed only by ±1% if the inlet air humidity ratio changes in the range of ± 2 g/kg (the maximum difference between the experimental conditions and AHRI conditions). Vali (2009) also shows that $\varepsilon_{o,sensible}$ changes less than 1% if the temperature variation is ±2°C around AHRI summer test conditions. This 2°C temperature difference is larger than the difference between the experimental and AHRI testing conditions as shown in Table 5-1. The sensitivity analysis suggests that effectiveness variation due to difference between AHRI and experimental summer conditions is minimal.

Figure 5-1 shows the comparison between experimental and numerical data for RAMEE sensible, latent and total effectiveness at different values of C_{sol}/C_{air} and NTU.

(a)

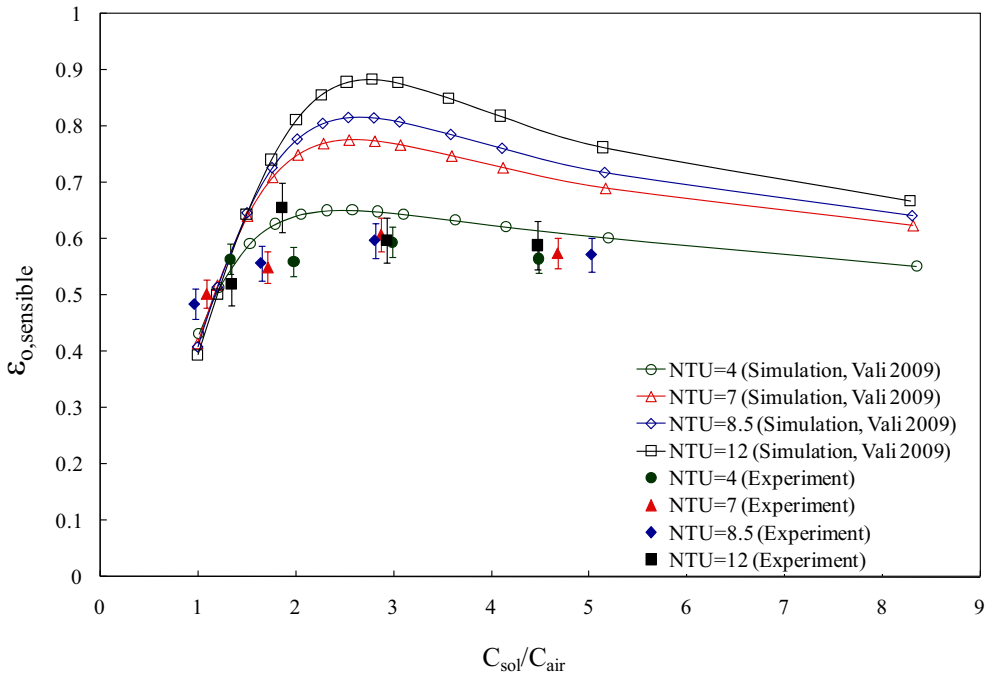
$\varepsilon_{o,sensible}$
C_{sol}/C_{air}
NTU=4 (Simulation, Vali 2009)
NTU=7 (Simulation, Vali 2009)
NTU=8.5 (Simulation, Vali 2009)
NTU=12 (Simulation, Vali 2009)
NTU=4 (Experiment)
NTU=7 (Experiment)
NTU=8.5 (Experiment)
NTU=12 (Experiment)

(b)

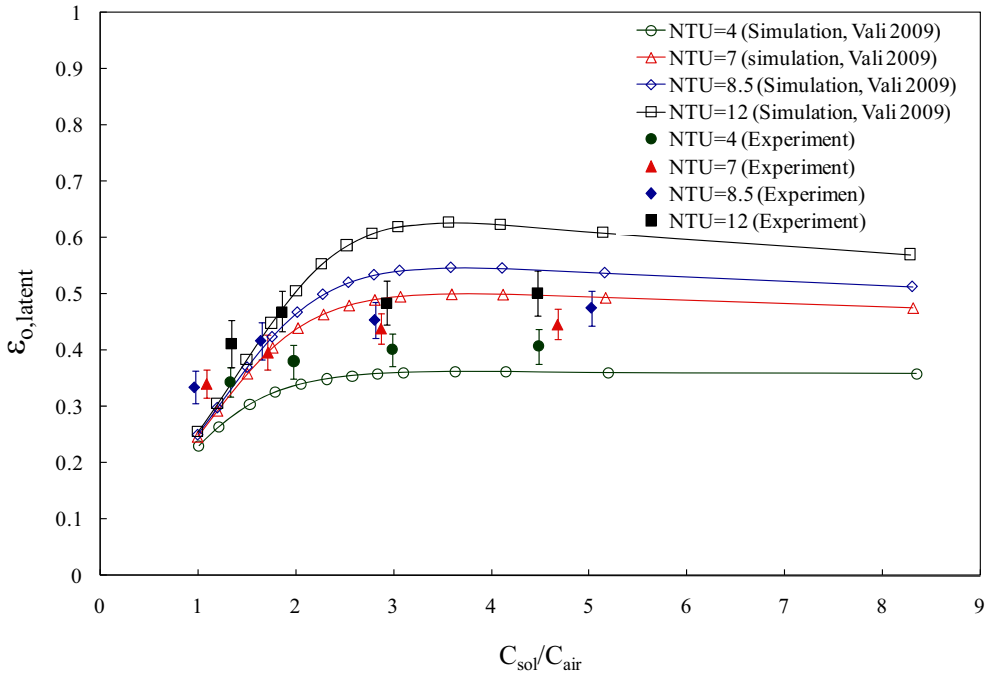
$\varepsilon_{o,latent}$
C_{sol}/C_{air}
NTU=4 (Simulation, Vali 2009)
NTU=7 (simulation, Vali 2009)
NTU=8.5 (Simulation, Vali 2009)
NTU=12 (Simulation, Vali 2009)
NTU=4 (Experiment)
NTU=7 (Experiment)
NTU=8.5 (Experimen)
NTU=12 (Experiment)

(c)

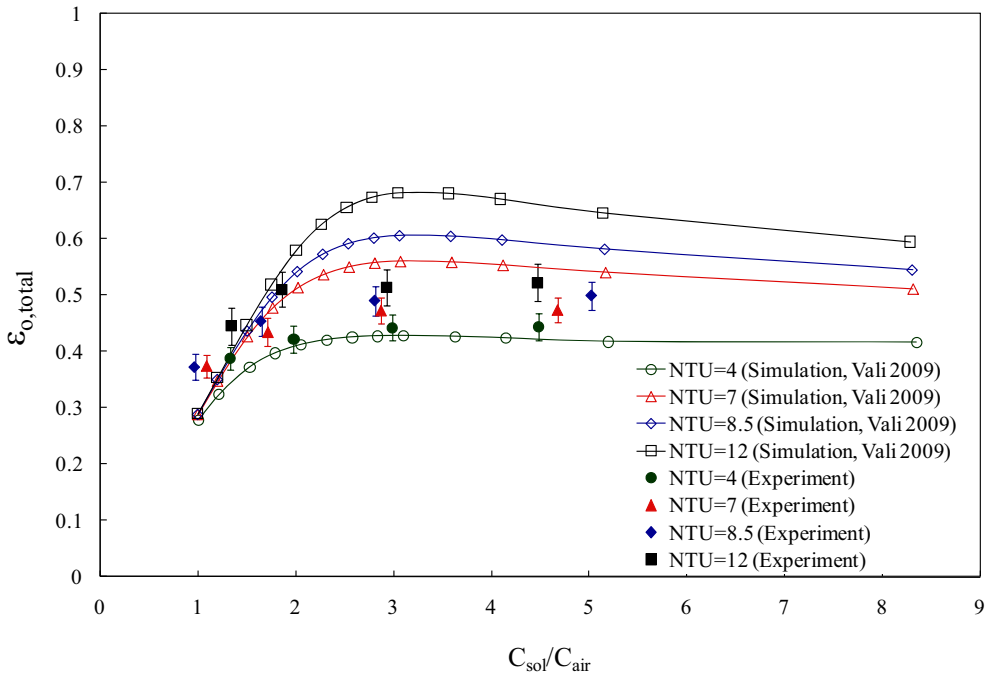

Figure 5-1. Experimental and numerical (a) sensible, (b) latent and (c) total effectiveness of the counter-cross-flow RAMEE system for summer operating conditions

Figure 5-1 shows that the experimental and numerical data have similar trends. Both experimental and numerical effectiveness values are low at low C_{sol}/C_{air} values and reach a peak with increasing C_{sol}/C_{air}. The numerical effectiveness decrease after reaching the peak value, while this decreasing trend is only observed in the experimental data for sensible effectiveness. It can also be seen that the experimental effectiveness are not as sensitive to NTU as the numerical data.

To quantify the difference between numerical and experimental effectiveness values, the root mean square error (RMSE, equation 5.1) and average absolute difference (AAD, equation 5.2) are used. Table 5-2 shows RMSE and AAD for different NTUs during summer conditions.

$$\mathrm{RMSE} = \sqrt{\frac{\sum_{1}^{N} (\varepsilon_{\mathrm{numerical}} - \varepsilon_{\mathrm{experimental}})^2}{N}} \tag{5.1}$$

$$\mathrm{AAD} = \frac{\left|\varepsilon_{\mathrm{numerical}} - \varepsilon_{\mathrm{experimental}}\right|}{N} \tag{5.2}$$

where,ε is effectiveness and N is the number of data points.

Table 5-2. RMSE and AAD values for RAMEE sensible, latent and total effectiveness during summer tests

	RMSE				*AAD*			
NTU	4	7	8.5	12	4	7	8.5	12
Sensible	0.06	0.14	0.16	0.20	0.06	0.14	0.15	0.18
Latent	0.05	0.06	0.07	0.09	0.05	0.05	0.06	0.08
Total	0.03	0.08	0.08	0.11	0.03	0.07	0.08	0.08

As a further illustration the experimental and numerical data for the RAMEE total effectiveness $(\varepsilon_{o,total})$ values as in Figure 5-1 (c) are presented for individual NTUs in Figure 5-2. RMSE and AAD values and uncertainty in C_{sol}/C_{air} in the experimental data are also included in Figure 5-2.

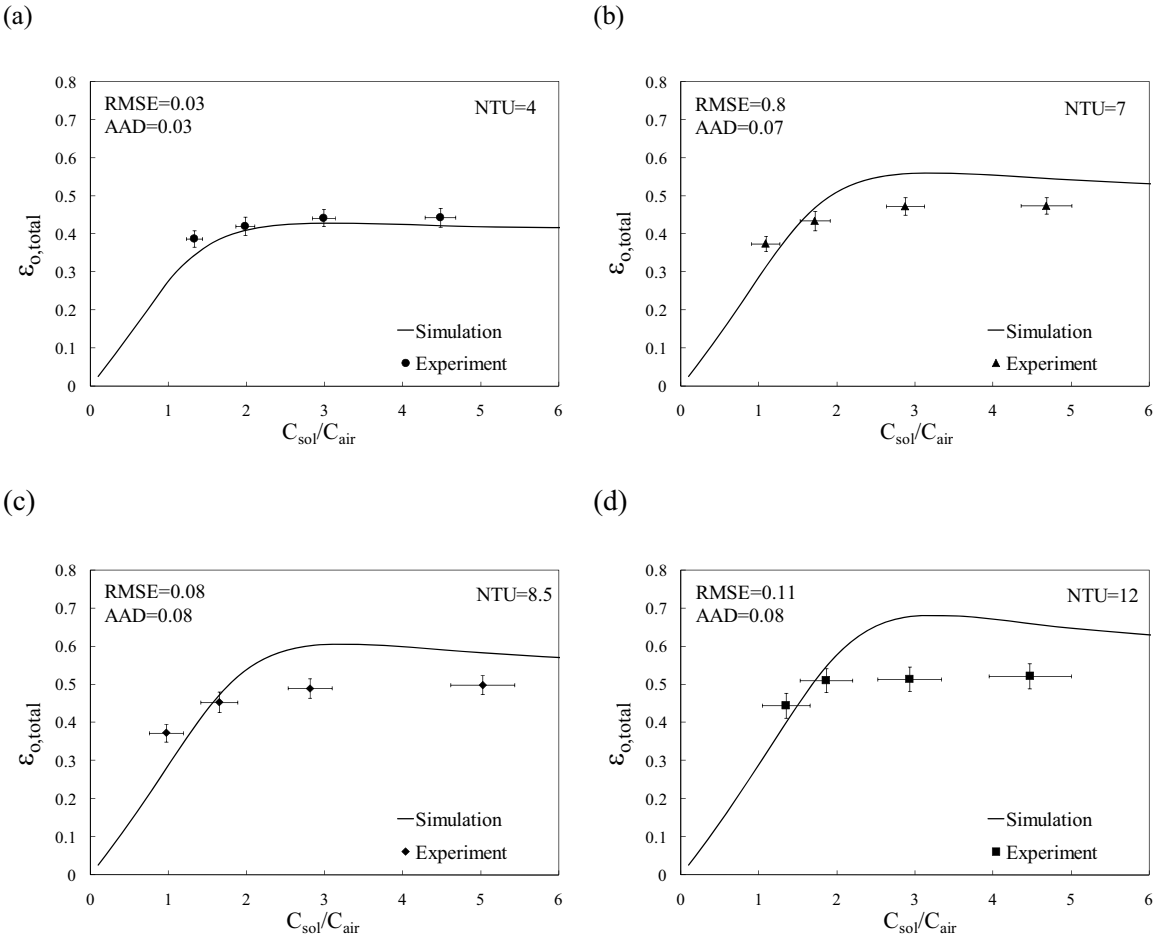

Figure 5-2. Experimental and numerical total effectiveness of the counter-cross-flow RAMEE system for summer operating conditions when (a) NTU = 4, (b) NTU = 7, (c) NTU = 8.5 and (d) NTU = 12

Figure 5-2 shows that the numerical and experimental data agree within the experimental uncertainty mainly at lower NTUs. For example RMSE and AAD for NTU = 4 are found 0.03 and 0.03 (Figure 5-2a). With increasing NTUs, the differences between the numerical and experimental total effectiveness increase and exceed the experimental uncertainty (e.g. at NTU = 12, RMSE and AAD are 0.11 and 0.08 respectively).

5.3 Reasons for discrepancies between experimental and numerical data

The discrepancies between experimental and numerical data may be due to mal-distributed desiccant solution-flow in the experiment, desiccant solution leakage in the experiment, uncertainties in membrane properties (thickness and water vapor permeability) and heat loss/gain effect in the experiment, uncertainties in the estimation of average air and solution-flow gap. These will be discussed in separate sections to better explain the discrepancies between experimental and numerical data.

5.3.1 Mal-distributed solution-flow

In the numerical model, it is assumed that solution and air-flow gap are constant throughout the entire exchanger and that all the liquid panels are filled with an equal amount of desiccant solution. In each counter-cross-flow exchanger the air and liquid flow gap are not constant due to flexible propore^{TM} membrane, outer screen deflection and length (1.8 m) of the exchanger. As a result, some liquid panels may have more flow than others. As well variations in the gaps for any particular panel will cause variations in the flow rate not modelled in Vali's (2009) model. The non-uniformity in fluid flow inside the exchangers could contribute to the differences between experimental and numerical data.

In addition to the non-uniform fluid flow between different liquid panels in each LAMEE some areas of the LAMEE may have reduced heat and mass transfer rates due to lower flow rates in these areas. As the NTU of the RAMEE system is increased at a constant C_{sol}/C_{air} by reducing the fluid flow rates, the experimental heat and mass transfer surface area may be less than that used by the numerical model which assumes ideal laminar flow in each panels. This could cause the experimental effectiveness to be lower

than the numerical effectiveness at higher NTUs, which is consistent with the results in Figure 5-2.

On the other hand, higher air and desiccant solution mass flow rates at low NTUs (for a constant C_{sol}/C_{air}) would result in more uniformly distributed flows within the exchangers. As a result, the numerical effectiveness has better agreement at low NTUs as shown in Figure 5-2.

5.3.2 Average air and solution-flow gap

Average air and desiccant solution-flow gap was estimated using membrane deflection and outer screen deflection and used in the numerical model to determine convective heat transfer coefficient. Membrane deflection of 1 mm was considered based on the study of Larson (2006). In case of the outer screen, a 1 mm deflection is assumed in between two round spacers which adds uncertainty in these values. In addition to that, it is difficult to estimate the average air-flow and solution-flow gap. As a result, the uncertainty in the average air and solution flow gaps could contribute the discrepancies between experimental and numerical values.

5.3.2 Desiccant solution leakage

Experimental and numerical discrepancies may be due to the leakage of desiccant solution into the air channels during the experiment which is not considered in the model. At lower NTUs, the desiccant solution mass flow rate is higher which may result in more solution leakage within the exchangers. Desiccant solution leakage into the air channels can increase moisture transfer rates and latent effectiveness in the experiments because of direct contact between the leaked desiccant solution and air stream. Figure 5-1 (b) shows that the experimental effectiveness values are higher than the numerical values for the

lower NTU (NTU = 4) and this may be due to desiccant solution leakage in the experiment.

5.3.3 Membrane water vapor permeability

The water vapor permeability of the membrane affects the latent effectiveness of the RAMEE system $(\varepsilon_{o,latent})$ by increasing or decreasing moisture fluxes through the membrane. $\varepsilon_{o,latent}$ will increase if the membrane permeability increase, and decrease if the membrane permeability decreases.

It is very difficult to measure the permeability of a membrane accurately due to the complexity of simulating exact operating condition of the RAMEE system, which leads to significant uncertainties in the permeability measurements. Using the permeability and uncertainty ($K_m = 1.66\times10^{-6} \pm 3.5\times10^{-7}$ kg/(m·s)) for Propore^{TM}, as measured by Larson (2006) , Vali (2009) carried out a sensitivity study on membrane permeability for summer condition at NTU = 10, H_{mem}/L = 0.5 and $L_{sol,e}/L$ = 0.1. Vali (2009) reported that increases the membrane permeability in the range of its associated uncertainty increases $\varepsilon_{o,latent}$ up to 2.2% and decreasing the membrane permeability decreases $\varepsilon_{o,latent}$ by up to 3% at $C_{sol}/C_{air}\approx3$. Membrane permeability variations with experimental uncertainty bounds also affect the RAMEE system sensible effectiveness $(\varepsilon_{o,sensible})$ up to ±1.5%. These fluctuations are smaller than the discrepancies between the experimental and numerical data at high NTUs but they may explain part of the differences.

5.3.4 Membrane thickness

The thickness of the membrane also has a great impact on the overall mass transfer coefficient and number of transfer units (Vali, 2009). In the numerical model a membrane thickness of 0.2 mm was used, which was reported by Mike Larson (2006). While

measuring the membrane thickness, it was found that the thickness of the membrane is 0.2 mm when it is compressed but it can be measured up to 0.5 mm. Increasing the membrane thickness increases the mass transfer resistance of the semi-permeable membrane and reduces the number of mass transfer units and the latent effectiveness of the RAMEE system $\left(\varepsilon_{o,latent}\right)$. Alternatively, lower membrane thickness results in higher latent effectiveness. Vali (2009) carried out a sensitivity analysis for summer condition at NTU = 10, H_{mem}/L = 0.5 and $L_{sol,e}/L$ = 0.1 and reported that if the membrane thickness is increased from 0.2 mm to 0.5 mm it will reduce the maximum $\varepsilon_{o,latent}$ (at $C_{sol}/C_{air}\approx 3$) by approximately 13%. For this same thickness change the sensible $\left(\varepsilon_{o,sensible}\right)$and total $\left(\varepsilon_{o,total}\right)$effectiveness of the RAMEE system will be reduced by 2% and 9% respectively. These results show that membrane thickness has significant impact on the numerical effectiveness values.

5.3.5 Heat loss effect in the experiment

In the current counter-cross-flow numerical model, steady-state effectiveness values are predicted without considering possible heat loss/gain in the experiment. However, heat losses are evident from the experimental results during summer tesing. Heat losses increases the difference between supply and exhaust exchanger effectiveness values. RAMEE effectiveness will also change. Seyed Ahmadi (2008, Figure 4-15a) showed that if heat loss effect is considered , at the worst case scenario (i.e. $\sigma_{sol} = -1$) sensible $\left(\varepsilon_{o,sensible}\right)$and latent $\left(\varepsilon_{o,latent}\right)$effectiveness of a cross-flow RAMEE system could be reduced up to 14% and 6% (at NTU = 5, C_{sol}/C_{air} = 3, ,λ = 0.15, ΔCn_{sol} = 0,summer condition).

5.4 Comparison between counter-cross-flow and cross-flow experimental results

The aim of this thesis is to improve RAMEE system performance by using a counter-cross-flow design rather than the previous cross-flow design of Erb (2007). The physical dimensions and design characteristics of the cross and counter-flow exchangers are different as shown in Table 5-3, but they were tested at similar values of NTU and C_{sol}/C_{air} to allow a direct comparison (Figure 5-3). However, V_{face} was lower in cross-flow RAMEe system. For example, V_{face} of cross-flow system was 0.18 m/s (NTU = 11) in comparison to V_{face} of 0.71 m/s (NTU = 12) in counter-cross-flow system.

Table 5-3. Specifications of counter-cross-flow and cross-flow RAMEE system

Parameters	*Counter-cross-flow RAMEE*	*Cross-flow RAMEE (Erb et al., 2009)*
Desiccant solution	$MgCl_2$	$MgCl_2$
Membrane	Propore™	Propore™
Exchanger dimensions ($H_{mem}xLxW$)	$0.2 \times 1.8 \times 0.089$ m	$0.3 \times 0.6 \times 0.1$ m
Air-flow gap (t_{air})	3.18 mm	4.76 mm
Liquid flow gap (t_{sol})	1.50 mm	1.70 mm
Number of liquid panels	10	10

Figure 5-3 presents the counter-cross-flow and cross-flow RAMEE effectiveness values for both summer and winter operating conditions. The total effectiveness of the counter-cross-flow RAMEE system (which gives very close performance to counter-flow exchanger) is found to be 10% to 20% higher than cross-flow RAMEE system. A similar trend is also observed for a single counter-flow heat exchanger (sensible effectiveness) compared to a cross-flow exchanger (Incropera and Dewitt, 2002).

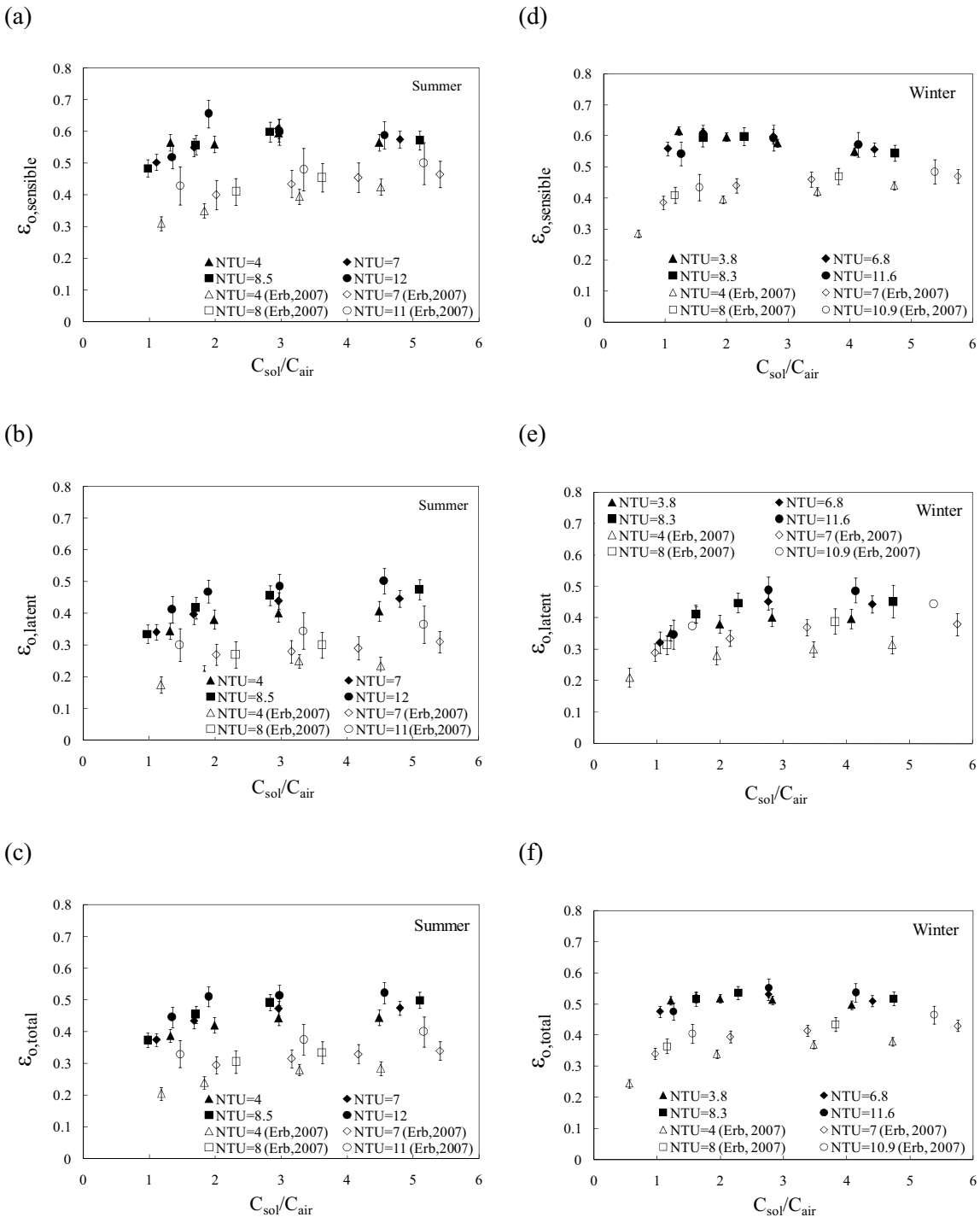

Figure 5-3. Comparison between counter and cross flow (Erb, 2007) RAMEE system effectiveness during summer (a,b,c) and winter (d,e,f) operating conditions

Figure 5-3 (c and f) also show that, the total effectiveness $\left(\varepsilon_{o,total}\right)$ of a counter-cross-flow exchanger is nearly constant for C_{sol}/C_{air} values of 3 or higher. However, in the cross-flow exchanger, the increasing trend for effectiveness is found after C_{sol}/C_{air} of 3 or higher. This indicates that mal-distribution flow may be reduced in the current counter-cross-flow RAMEE design.

5.5 Summary

In this chapter, counter-cross-flow RAMEE experimental effectiveness are compared with predicted numerical effectiveness values. The comparison shows that both the experimental and numerical data show the same general trends for effectiveness as a function C_{sol}/C_{air}. The numerical and experimental effectiveness are in good agreement for lower NTU values (e.g. NTU = 4). The discrepancy between the measured and predicted total effectiveness are within experimental uncertainty bounds for NTU = 4 (RMSE = 0.03, AAD = 0.03). However, the differences between the numerical and experimental effectiveness increase at higher NTUs and lower solution-flow rates. The discrepancies between the numerical and experimental effectiveness may be due to non-uniform solution-flow inside the exchangers, uncertainty in average air and solution-flow gap, the desiccant solution leakage into the air channels, uncertainty in the permeability and thickness of the membrane used in the numerical model heat loss during the experiments.

The experimental effectiveness of the counter-cross-flow RAMEE system are also compared with experimental effectiveness of a cross-flow RAMEE system (Erb, 2007) for both summer and winter operating condition. The counter-cross-flow RAMEE total

effectiveness values for similar operating conditions is found to be 10 to 20% higher than cross-flow system. In case of V_{face}, the counter flow RAMEE design is improved.

CHAPTER 6
SUMMARY, CONCLUSION AND FUTURE WORK

6.1 Summary and conclusions

This study is part of a larger research project to design, test and develop prototypes of a Run-Around Membrane Energy Exchanger (RAMEE) system based on industry recommended criteria and ASHRAE standards. The overall objective of this thesis project is to design, build and test a counter-cross-flow RAMEE system to achieve competitive overall effectiveness, to conduct performance testing of the designed RAMEE system and to investigate any discrepancies between the theoretical/numerical model and the measured test data.

The RAMEE is an energy recovery system capable of exchanging sensible and latent energies between the exhaust and supply air-streams in an HVAC system. Since the ducts for the supply and exhaust for the RAMEE system can be located far apart it is for retrofit HVAC applications and buildings for which transfer of exhaust air into the supply air is not permitted. The objectives of the present research are divided into four categories (chapter 1). The following sections describe how those objectives are addressed in different chapters of this thesis.

The two identical counter-cross-flow Liquid-to-Membrane Energy Exchangers (LAMEEs) are designed to obtain an overall effectiveness of 65% for the RAMEE system at a face velocity of 2 m/s. The exchanger design is based on the heat exchanger theory and the study of Vali (2009). The geometric flow-path design used in this study has liquid entrance and exit headers in the cross-flow direction relative to the air-flow and

these are located at the diagonally opposite corners of each exchanger as a result most of the liquid flow is counter-flow to the air-flow. The flow path design will result in an exchanger performance nearly as high than that of a pure counter-flow LAMEE but with an added advantage of having the liquid headers outside the air-flow path. As a design constraint, the pressure drop inside the air-flow channels is constrained to less than 0.5 inch of water (125 Pa) at 2 m/s. On the other hand, liquid side pressure drop is based on the height of the exchanger which is the vertical distance between the two liquid headers. One LAMEE is employed in the supply line and a second LAMEE is employed in the exhaust line of the RAMEE system. The two LAMEEs are then coupled with a liquid line running in a run around closed-loop between the exchangers.

The design parameters to be selected are: desiccant solution, exchanger membrane surface aspect ratio, entrance ratio, liquid panel and air channel design for the liquid and air-flow, materials and membrane selection, membrane area design, and estimates of the convective heat transfer coefficient and overall heat transfer coefficient. In the current design, $MgCl_2$ salt solution is selected for the coupling liquid for the RAMEE. A membrane surface aspect ratio (H_{mem}/L) of 1/9 and entrance ratio ($L_{sol,e}/L$) of 1/24 are chosen because the total effectiveness for the RAMEE was predicted to be very close to a system using two counter-flow exchanger (Vali, 2009). Based on different case studies, the exchanger size is determined as 1800 mm x 200 mm x 86 mm. Detail specifications of the exchangers/LAMEEs are tabulated in Table 2-2. Each exchanger is constructed with ten liquid panels. Micro-porous membrane with the brand name Propore^{TM} is used for transferring sensible and latent energy based on the study of Larson (2006). The

membrane area is estimated based on the available flat-plate heat transfer correlation as no heat and mass transfer correlation was available.

The RAMEE system has been tested in a test apparatus developed by Erb (2007). Differential pressure transducers and orifice plates are used to measure the air-flow rate ($\dot{m}_{air}$). Humidity sensors and RTDs are used to measure the air humidity ratio (W_{air}) upstream and downstream of each LAMEE. Thermocouples are used to measure the air and solution flow temperatures. T_{air} and T_{sol}, and a rotometer is employed to measure the liquid flow rate ($\dot{m}_{sol}$). The NI data acquisition system controlled via an in-house LabVIEW program acquires data from all the sensors. To evaluate the RAMEE performance different tests are designed at the AHRI summer and winter operating conditions (AHRI STANDARD 1060, 2005). The tests include variations of the NTU and C_{sol}/C_{air} values. However, the experimental test conditions are found slightly different from the ideal AHRI conditions due to the uncontrolled exhaust inlet conditions of the test apparatus.

Three types of effectiveness values (i.e. sensible, latent, and total effectiveness) are determined from the measured data to evaluate the RAMEE performance. Total uncertainties including the sensor precision errors and measurement bias errors are determined based on the ASME PTC 19.1 1998 standard using the 95% confidence interval (reported in Table 3-2). Measurements illustrate the transient and quasi steady-state behavior of the RAMEE system. From the typical test data, it is found that the RAMEE system does not reach steady-state conditions even though the air temperature, solution temperature, and air humidity ratio become nearly constant at the end of the tests. As a result, the average effectiveness values of the RAMEE are calculated

(equations 1.2) from the measured quasi steady-state data based on the study of Seyed Ahmadi (2008). The maximum total effectiveness ($\varepsilon_{o,\,total}$) of the RAMEE system for the summer testing conditions is found to be 53% at NTU of 12.0 and C_{sol}/C_{air} of 4.5. In case of the winter testing conditions, the maximum total effectiveness found to be 55% (NTU = 11.8, C_{sol}/C_{air} = 2.8). At the target face velocity of around 2 m/s, the total effectiveness of the RAMEE system which is found to be 0.45 (C_{sol}/C_{air} = 4.7) for summer and 0.50 (C_{sol}/C_{air} = 4.4) for winter test condition. The lower effectiveness than the target design value (65% of total effectiveness) may be due to inapplicability of sensible heat transfer correlations for the RAMEE system design, lower than expected water vapor permeability of the membrane, the mal-distributed desiccant solution-flow in the experiment, desiccant solution leakage in the experiment, and heat loss/gain effects in the experiment.

The counter-cross-flow RAMEE experimental effectiveness values are compared with a numerical model (Vali, 2009). The comparison shows that both the experimental and numerical results follow similar general trends for the change in effectiveness as C_{sol}/C_{air} changes. The numerical and experimental effectiveness are in better agreement for lower NTU values [e.g. Average Absolute Difference (AAD) of 3% at NTU = 4] than for higher NTU values (e.g. AAD of 8% at NTU = 12). The discrepancies between the numerical and experimental effectiveness at higher NTUs may be due to the mal-distributed desiccant solution-flow in the experiment, desiccant solution leakage in the experiment, and heat loss/gain effects in the experiment and uncertainty in the permeability and thickness of the membrane used in the numerical model.

The experimental effectiveness of the present counter-cross-flow RAMEE system are also compared with the experimental effectiveness of a cross-flow RAMEE system (Erb, 2007) for both the summer and winter operating conditions. The counter-cross-flow RAMEE effectiveness are found to be 10% to 20% higher than those for the cross-flow RAMEE system.

6.2 Future work

From the test data, effectiveness values are found lower than the designed effectiveness values at 2 m/s. Discrepancies are also found at higher NTU values when the experimental values are compared with numerical effectiveness. To achieve the target effectiveness at 2 m/s following issues need to be addressed

- A membrane with higher water vapor permeability values needs to be found.
- Sufficient insulation of the supply and exhaust exchanger is needed to reduce the heat loss/gain to a small fraction of the exchanger heat rate.
- The LAMEE design should be improved to reduce mal-distribution flow inside the exchangers.
- The membrane permeability values needs to be determined accurately to be used in the numerical model.
- The average air and solution-flow gap needs to be accurately estimated.

To reduce the discrepancies between the experimental data and numerical simulations changes should be made to the numerical model as listed below.

- Mal-distribution effects need to be added.
- Heat loss/gain effects also need to be included.

- Transient effects should be included in the numerical model to predict the quasi-steady-state behavior of the RAMEE system during typical conditions

In this study, only $MgCl_2$ solution has been used as the desiccant solution. It is believed that the type of the desiccant solution also affects the system performance. Therefore, the performance of a RAMEE system using different desiccant solutions should be studied to search and determine the best desiccant solution for the RAMEE system. In addition to the performance, the best desiccant solution should be determined considering the cost, operating conditions, availability, and safety. The impacts of frosting on the air side and crystallization of the salt solution on the performance of the system are other additional topics for future investigation.

Lastly, this study has tested the counter-cross-flow RAMEE system in a laboratory environment. A field study should be done to test the counter-cross-flow RAMEE system in actual buildings. The field test should be recommended to investigate both the design load and the part load controls of the RAMEE system. From the experimental data, it is evident that the RAMEE system might require a long time to reach steady-state conditions. The study carried out by Seyed-Ahmadi (2008) also showed long time delays to reach steady state in a cross-flow RAMEE system. This may limit the applications of the RAMEE system in cases when the system operates with large step changes in the inlet conditions. Therefore, methods are needed to control the system and reduce the transient times.

.

LIST OF REFERENCES

AHRI STANDARD 1060, 2005. *Performance rating for air-to-air exchangers for energy recovery ventilation equipment.* Arlington: Air-Conditioning & Refrigeration Institute.

ANSI/ASHRAE STANDARD 55-2004, *Thermal environmental conditions for human occupancy.* Atlanta: American Society of Heating, Refrigerating, and Air-Conditioning Engineers.

ANSI/ASHRAE STANDARD 62.1-1981, *Ventilation for acceptable indoor air quality.* Atlanta: American Society of Heating, Refrigerating, and Air-Conditioning Engineers.

ANSI/ASHRAE STANDARD 62.1-2004, *Ventilation for acceptable indoor air quality.* Atlanta: American Society of Heating, Refrigerating, and Air-Conditioning Engineers.

ANSI/ASHRAE STANDARD 84-2008, *Method of test for air-to-air heat/energy exchangers.* Atlanta: American Society of Heating, Refrigerating, and Air-Conditioning Engineers.

ANSI/ASHRAE STANDARD 90.1-2007, *Energy standards for buildings except for low-rise residential buildings.* Atlanta: American Society of Heating, Refrigerating, and Air-Conditioning Engineers.

ASHRAE, 2005. ASHRAE Handbook-Fundamentals. Atlanta: American Society of Heating, Refrigerating, and Air-Conditioning Engineers.

ASHRAE, 2004. ASHRAE Handbook-HVAC Systems and Equipment. Atlanta: American Society of Heating, Refrigerating, and Air-Conditioning Engineers.

ASME PTC 19.1-1998, *Test uncertainty.* New York: American Society of Mechanical Engineers.

Bennett, I.J.D., Besant, R.W., Schoenau, G.J. and Johnson, A.B., 1994. Procedure for optimizing coils in a run-around heat exchanger system. *ASHRAE Transactions,* **100**(1), pp. 442-451.

Beriault, D., 2009. *Development and testing of a new Run-Around Membrane Energy Exchanger (RAMEE) system for buildings,* M.Sc Thesis in progress, Department of Mechanical Engineering, University of Saskatchewan, Saskatoon.

Besant, R.W. and Forsyth, B.I., 1988. The design of a run-around heat recovery system. *ASHRAE Transactions,* **94**(2), pp. 511-531.

Besant, R.W. and Simonson, C.J., 2003. Air-to-air energy recovery. *ASHRAE Journal,* **45**(4), pp. 42-52.

Besant, R.W. and Simonson, C.J., 2000. Air-to-air energy recovery. *ASHRAE Journal,* **42**(5), pp. 31-32.

CES EDU PACK, 2007. Granta Design Limited, Cambridge, United Kingdom.

Cisternas, L.A. and Lam, E.J., 1991. Analytic correlation for the vapor pressure of aqueous and non-aqueous solutions of single and mixed electrolytes: Part II - Application and extension, *Fluid phase equilibria*, **62**(1), 11-27.

Charles, N.T. and D. W. Johnson, 2008. The occurrence and characterization of fouling during membrane evaporative cooling. *Journal of Membrane Science,* **319**, pp. 44-53.

Dhital, P., Besant, R.W. and Schoenau, G.J., 1995. Integrating run-around heat exchanger systems into the design of large office buildings. *ASHRAE Transactions,* **101**, pp. 979-991.

Avallone, E.A. and Baumeister, T., 1996. Marks' Standard Handbook for Mechanical Engineers. 10th edn. Atlanta: McGraw-Hill.

Emerson, W.H., 1984. Making the most of run-around coil systems. *Journal of Heat Recovery Systems,* **4**(4), pp. 265-270.

Erb., B., 2007. *Run-around membrane energy exchanger prototype-2 testing, Summer work report.* Saskatoon, Saskatchewan: Department of Mechanical Engineering, University of Saskatchewan.

Erb., B., 2006. *Designing and testing a run-around heat and moisture recovery system, Summer work report.* Saskatoon, Saskatchewan: Department of Mechanical Engineering, University of Saskatchewan.

Erb., B., Ahmadi., M.S., Simonson, C.J. and Besant, R.W., 2009. Experimental measurements of a run-around membrane energy exchanger (RAMEE) with comparison to numerical modeling. *ASHRAE Transactions,* **111**(1), pp. 901-910.

Fan, H., 2005. *Modeling a run-around heat and moisture recovery system*, Department of Mechanical Engineering, University of Saskatchewan, Saskatoon.

Fan, H., Simonson, C.J., Besant, R.W. and Shang, W., 2006. Performance of a run-around system for HVAC heat and moisture transfer applications using cross-flow plate exchangers coupled with aqueous lithium bromide. *HVAC&R Research,* **12**(2), pp. 313-336.

Fan, H., Simonson, C.J., Besant, R.W. and Shang, W., 2005. Run-around heat recovery system using cross-flow flat-plate heat exchangers with aqueous ethylene glycol as the coupling fluid. *ASHRAE Transactions,* **111**(1), pp. 901-910.

Fehrm, M., Reiners, W. and Ungemach, M., 2002. Exhaust air heat recovery in buildings. *International Journal of Refrigeration,* **25**, pp. 439-449.

Forsyth, B.I. and Besant, R.W., 1994. The design of a run-around heat recovery system. *ASHRAE Transactions,* **2**, pp. 511-531.

Hemingson, H., 2005. *Preliminary testing for run around heat and moisture exchanger, Summer work report.* Saskatoon, Saskatchewan: Department of Mechanical Engineering, University of Saskatchewan.

Incropera, F.P. and Dewitt, D.P., 2002. Fundamental of heat and mass transfer. 5th edn. New York. McGraw-Hill.

ISO STANDARD 5167-1, *Measure of fluid flow by means of pressure differential devices.* International Organization of Standardization.

Johnson, A.B., Besant, R.W. and Schoenau, G.J., 1995. Design of multi-coil run-around heat exchanger systems for ventilation air heating and cooling. *ASHRAE Transactions,* **101**, pp. 967-978.

Johnson, D.W., Yavuzturk, C. and Pruis, J., 2003. Analysis of heat and mass transfer phenomena in hollow fiber membranes used for evaporative cooling. *Journal of Membrane Science,* **227**(1-2), pp. 159-171.

Kays, W.M. and Crawford, M.E., 1980. Convective heat and mass transfer. 2nd edn. United States of America: New York. McGraw-Hill.

Kistler, K.R. and Cussler, E.L., 2002. Membrane modules for building ventilation. *Chemical Engineering Research and Design,* **80**(1), pp. 53-64.

Larson, M.D., 2006. *The performance of membrane in a newly proposed run-around heat and moisture exchanger*, M.Sc Thesis, Department of Mechanical Engineering, University of Saskatchewan, Saskatoon.

Larson, M.D., Simonson, C.J., Besant, R.W. and Gibson, P.W., 2007. The elastic and moisture transfer properties of polyethylene and polypropylene membranes for use in liquid-to-air energy exchangers. *Journal of Membrane Science,* **302**(1-2), pp. 136-149.

MINI-1200, 2004. *Two-pressure humidity generator, operation and maintenance manual.* New Mexico: Thunder Scientific Corporation.

NI PCI-6251, 2008-last update, high-speed M series multifunction data acquisition [Homepage of National Instruments], [Online]. Available: http://sine.ni.com/nips/cds/view/p/lang/en/nid/14124.

Niu, J.L. and Zhang, L.Z., 2001. Membrane-based enthalpy exchanger: material considerations and clarification of moisture resistance. *Journal of Membrane Science,* **189**(2), pp. 179-191.

Perez-Lombard, L., Ortiz, J. and Pout, C., 2008. A review on buildings energy consumption information. *Energy & Buildings,* **40**(3), pp. 394-8.

Redlich, C., A., Spacer, J. and Cullen. M., R., 1997. Sick-building syndrome. *Occupational medicine,* **349**(1), pp. 1013-1016.

Seyed Ahmadi, M., 2008. *Modeling the transient behaviour of a run-around heat and moisture exchanger system*, M.Sc Thesis, Department of Mechanical Engineering, University of Saskatchewan, Saskatoon.

Shah, R.K. and London, A.L., 1978. Laminar flow forced convection in ducts. New York: Academic Press.

Simonson, C.J., Ciepliski, D.L. and Besant, R.W., 1999. Determining the performance of energy wheels: Part I-Experimental and numerical method. *ASHRAE Transactions,* **105**(1), pp. 174-187.

Vali., A., 2009. *Modeling a run-around heat and moisture exchanger using two counter/cross flow exchangers*, M.Sc Thesis, Department of Mechanical Engineering, University of Saskatchewan, Saskatoon.

VALIDYNE-P855, 2007-last update, P855 digitally compensated differential pressure transmitter [Homepage of Validyne Engineering], [Online]. Available: http://www.validyne.com/data_pdf/p855.pdf.

White, F. M., 2005. Fluid Mechanics. 5th edition. New York: McGraw-Hill.

Zaytsev, I.D. and Aseyev, G.G., 1992. Properties of aqueous solutions of electrolytes. CRC Press, Inc.

Zeng, Y.Y., 1990. *A study of the performance of run-around heat recovery system using aqueous glycol/air as the coupling fluid*, M.Sc Thesis, Department of Mechanical Engineering, University of Saskatchewan, Saskatoon.

Zeng, Y.Y., Besant, R.W. and Rezkallah, K.S., 1992. Performance of a run-around system using a two-phase, gas-liquid coupling fluid. *ASHRAE Transactions,*

98(l), 563-573.

Zhang, L.Z. and Jiang, Y., 1999. Heat and mass transfer in a membrane-based energy recovery ventilator. *Journal of Membrane Science,* **163**(1), pp. 29-38.

APPENDIX-A
DESICCANT SOLUTION AND AIR PROPERTIES

A.1 Desiccant solution properties

Density

The density of the desiccant solution was calculated by using equation (A.1) (Zaytsev and Aseyev, 1992, page 1724).

$$\log\rho_{sol} = \log\rho_{w} + \sum b_i Cn_{sol,i} \tag{A.1}$$

$$\rho_{w} = 1000 - 0.062t - 0.00355T_{sol}^{\ 2} \tag{A.2}$$

$$b_i Cn_{sol} = (b_1 + b_2 T_{sol} + b_3 T_{sol}^{\ 2}) \times \frac{Cn_{sol}}{100} \tag{A.3}$$

Where

ρ_{sol} is the density of the desiccant solution (kg/m^3),

ρ_{w} is the density of the water (kg/m^3),

T_{sol} is the temperature of the desiccant solution (°C),

b_1, b_2, b_3 are density constants for particular solutions and,

Cn_{sol} is the desiccant solution concentration

Specific heat

Specific heat of the desiccant solution was calculated by using equation (A.4) reported in Zaytsev and Aseyev (1992, page.1732).

$$c_{p,sol} = 134225.4\left(\frac{273.15 + T_{sol}}{100}\right)^{-6.5} + 3490\left(\frac{273.15 + T_{sol}}{100}\right)^{0.14} + \frac{Cn_{sol}}{100}\left(r_1 + r_2\frac{Cn_{sol}}{100} + r_3 T_{sol} + r_4 T_{sol}^2\right) \quad (A.4)$$

Where

$c_{p,sol}$ is the heat capacity of the desiccant (J/kg.K),

r_1, r_2, r_3 and r_4 are the constants for a particular salt solution.

Viscosity

Zaytsev and Aseyev (1992, page1728) reported the following correlations (equation A.5 and A.6) for calculating dynamic viscosity of the desiccant solution.

$$\log\mu_{sol} = \log\mu_w + \sum_i (r^*_i Cn_{sol,i}) \quad (A.5)$$

$$r^*_i\, Cn_{sol} = \left(r^*_1 + r^*_2\, T_{sol} + r^*_3\, T_{sol}^{\,2}\right)_i \times Cn_{sol} \quad (A.6)$$

Where

μ_{sol} is the viscosity of the desiccant solution ,($N.s/m^2$)

μ_w is the viscosity of water ,($N.s/m^2$)

r^*_1, r^*_2, r^*_3 are the constants for a particular solution.

Thermal conductivity

Zaytsev and Aseyev (1992, page.1739) reported the following correlations (equation A.7 and A.8) for calculating thermal conductivity of the desiccant solution.

$$k_{sol} = k_w\left[1 - \sum_i \beta_i Cn_{sol\,i}\right] \quad (A.7)$$

$$k_w = 0.5545 + 0.00246T_{sol} - 0.00001184T_{sol}^{\,2} \quad for \quad T_{sol} = (0, 100^oC) \quad (A.8)$$

where

k_{sol} is the thermal conductivity of the desiccant solution

k_w is the thermal conductivity of water

β is the coefficient ($\beta_{MgCl_2} = 0.4779$)

A.2 Air properties

Saturation air pressure can be calculated using equation (A.9) when the airstream temperature is measured to be more than 273.15 K (0°C) (ASHRAE, 2005, page.6.2).

$$P_{air,sat} = \exp\left(\begin{array}{l}\dfrac{8c}{(T_{air}+273.15)} + 9c + 10c(T_{air}+273.15) + 11c(T_{air}+273.15)^2 + \\ 12c(T_{air}+273.15)^3 + 13c(\ln(T_{air}+273.15))\end{array}\right) \quad \text{(A.9)}$$

Here, $8c, 9c, 10c, 11c, 12c, \text{and} 13c$ are all saturation pressure constants, and are given as follows

$8c = -5800.22$

$9c = 1.3915$

$10c = -0.04864$

$11c = 4.2E-05$

$12c = -1.4E-08$

$13c = 6.54597$

APPENDIX B
LEAKAGE TESTING OF LIQUID PANELS

B.1 Leakage testing of liquid panels

Leakage testing of the liquid panels is very important to reduce or eliminate any leakages inside a LAMEE while it is in operation. Leakages can corrode the supply and exhaust air ducts. Large leeks can also change the effectiveness values (Vali, 2009) as the leaked desiccant solution comes in direct contact with the air streams & moisture transfer occurs in a higher rate. Therefore, prior to installing the liquid panels in a LAMEE, it was tested in a leakage testing apparatus developed by Beriault (2009). The leakage test apparatus is primarily constructed with metal and plastic clamps to hold a liquid panel and two liquid headers (Figure B-1 and B-2)

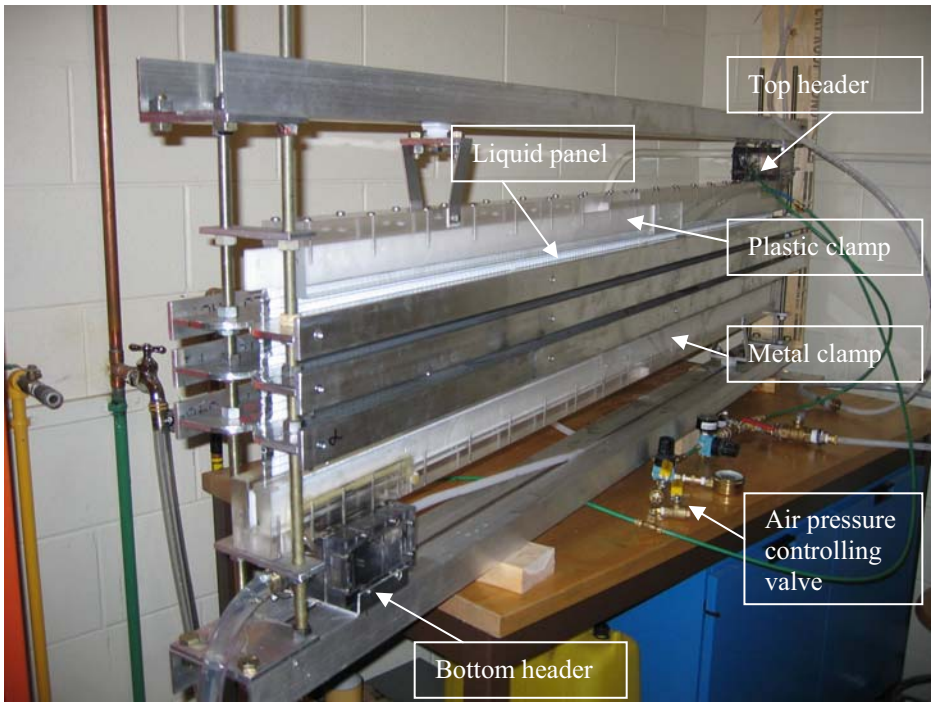

Figure B-1. Leakage test apparatus with a liquid panel mounted on it

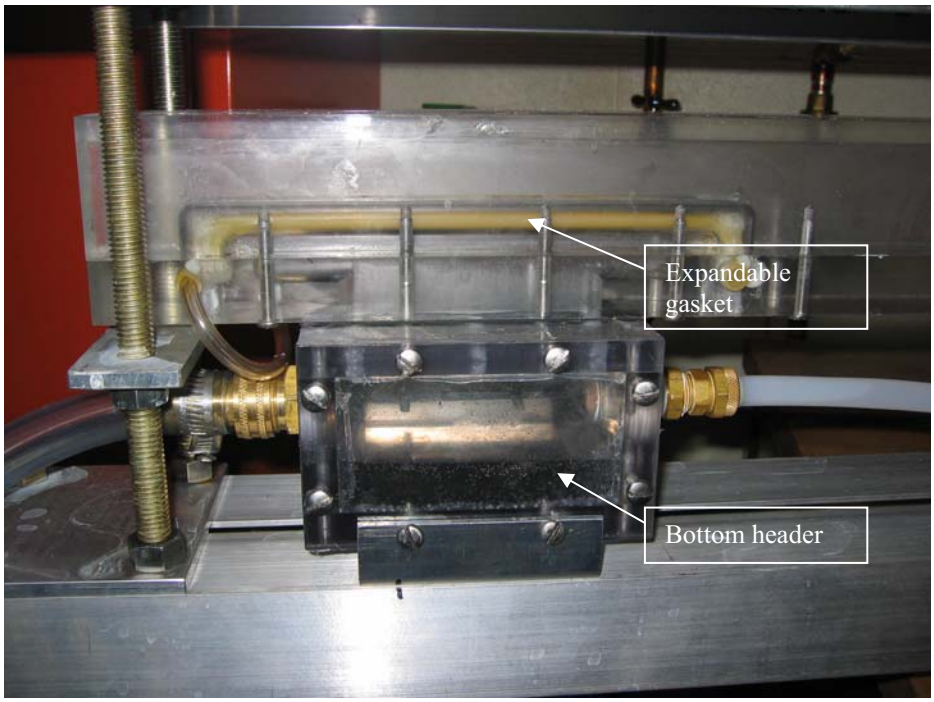

Figure B-2. Bottom header of the leakage test apparatus

The plastic clamps hold in the top and bottom edges of the panel along the length (L) as shown in Figure B-1. The metal clamps hold in the middle part of the liquid panel longitudinally. The two liquid headers as shown in Figure B-1 and B-2 are located at the end of the plastic clamps and are aligned with the entrance of the liquid panel.

APPENDIX C
TEST RESULTS

C.1 Summer test

Table C-1. Counter-cross-flow RAMEE performance during summer testing

NTU	C_{sol}/C_{air}	Effectiveness								
		Supply LAMEE			Exhaust LAMEE			RAMEE		
		Sensible	Latent	Total	Sensible	Latent	Total	Sensible	Latent	Total
Desiccant solution-flow : bottom-to-top										
12.0	1.3	37%	58%	51%	67%	25%	38%	52%	41%	45%
12.1	1.9	60%	57%	58%	72%	37%	44%	66%	47%	51%
12.0	2.9	54%	60%	59%	65%	37%	44%	60%	49%	52%
12.0	4.5	51%	63%	60%	67%	38%	45%	59%	51%	53%
8.5	1.0	51%	41%	44%	46%	26%	31%	48%	33%	37%
8.5	1.6	45%	57%	54%	66%	27%	37%	55%	42%	45%
8.5	2.8	62%	56%	58%	57%	34%	40%	59%	45%	49%
8.5	5.0	61%	58%	59%	53%	37%	41%	57%	47%	50%
6.9	1.1	59%	43%	47%	41%	25%	28%	50%	34%	37%
7.2	1.7	46%	54%	52%	64%	25%	35%	55%	40%	44%
6.9	2.9	72%	49%	54%	50%	39%	41%	60%	44%	47%
6.9	4.7	61%	57%	58%	54%	32%	37%	57%	44%	47%
4.0	1.3	79%	46%	53%	34%	22%	25%	57%	34%	39%
4.0	2.0	77%	50%	56%	35%	26%	28%	56%	38%	42%
4.0	3.0	85%	52%	59%	34%	28%	29%	60%	40%	44%
4.0	4.5	74%	55%	60%	39%	26%	29%	57%	41%	45%
Desiccant solution-flow: top-to-bottom										
7.9	3.3	68%	33%	41%	30%	35%	34%	49%	34%	38%
7.9	6.0	68%	43%	48%	44%	38%	39%	56%	40%	44%
7.9	8.7	70%	45%	50%	43%	41%	42%	56%	43%	46%
5.6	2.3	72%	35%	41%	21%	27%	26%	46%	31%	34%
5.5	4.2	73%	42%	48%	40%	30%	31%	56%	36%	40%
Desiccant solution-flow : bottom-to-top , extra insulation										
4.1	1.3	76%	44%	49%	31%	25%	26%	54%	35%	38%
4.1	1.3	76%	42%	49%	32%	27%	28%	54%	35%	39%
4.1	3.1	71%	53%	57%	40%	27%	30%	55%	40%	43%
4.1	4.4	81%	49%	55%	40%	32%	33%	61%	40%	44%

Table C-2. Uncertainty associated with counter-cross-flow RAMEE performance during summer testing

NTU	C_{sol}/C_{air}	Effectiveness								
		Supply LAMEE			Exhaust LAMEE			RAMEE		
		Sensible	Latent	Total	Sensible	Latent	Total	Sensible	Latent	Total
Desiccant solution-flow : bottom-to-top										
12.0	1.3	4%	7%	5%	6%	5%	5%	4%	4%	3%
12.1	1.9	6%	6%	4%	7%	4%	5%	4%	4%	3%
12.0	2.9	5%	6%	4%	6%	5%	5%	4%	4%	3%
12.0	4.5	5%	7%	5%	7%	5%	5%	4%	4%	3%
8.5	1.0	4%	5%	4%	4%	3%	3%	3%	3%	2%
8.5	1.6	4%	5%	4%	5%	4%	4%	3%	3%	3%
8.5	2.8	5%	5%	4%	4%	4%	4%	3%	3%	3%
8.5	5.0	4%	5%	4%	4%	4%	4%	3%	3%	3%
6.9	1.1	4%	4%	3%	3%	3%	3%	3%	2%	2%
7.2	1.7	4%	5%	4%	4%	4%	3%	3%	3%	3%
6.9	2.9	5%	4%	3%	4%	4%	3%	3%	3%	2%
6.9	4.7	4%	4%	3%	4%	3%	3%	3%	3%	2%
4.0	1.3	4%	4%	3%	3%	3%	3%	3%	3%	2%
4.0	2.0	4%	5%	4%	3%	4%	3%	3%	3%	2%
4.0	3.0	4%	4%	3%	3%	4%	3%	3%	3%	2%
4.0	4.5	4%	5%	4%	3%	4%	3%	3%	3%	2%
Desiccant solution-flow : bottom-to-top , extra insulation										
7.9	3.3	5%	4%	3%	3%	3%	3%	3%	3%	2%
7.9	6.0	5%	4%	3%	4%	3%	3%	3%	3%	2%
7.9	8.7	5%	4%	3%	3%	3%	3%	3%	3%	2%
5.6	2.3	4%	3%	3%	3%	3%	2%	3%	2%	2%
5.5	4.2	4%	3%	3%	3%	3%	3%	3%	2%	2%
Desiccant solution-flow top-to-bottom										
4.1	1.3	4%	4%	3%	4%	3%	3%	3%	2%	2%
4.1	1.3	4%	4%	3%	3%	3%	3%	3%	3%	2%
4.1	3.1	4%	5%	4%	4%	4%	3%	3%	3%	2%
4.1	4.4	4%	4%	3%	4%	3%	3%	3%	2%	2%

C.2 Winter test

Table C-3. Counter-cross-flow RAMEE performance during winter testing

NTU	C_{sol}/C_{air}	Effectiveness								
		Supply LAMEE			Exhaust LAMEE			RAMEE		
		Sensible	Latent	Total	Sensible	Latent	Total	Sensible	Latent	Total
Desiccant solution-flow : bottom-to-top										
3.8	1.2	76%	42%	62%	47%	28%	40%	62%	35%	51%
3.8	2.0	72%	48%	63%	48%	28%	41%	60%	38%	52%
3.8	2.8	68%	50%	61%	47%	31%	41%	58%	40%	51%
3.8	4.1	67%	54%	63%	43%	26%	37%	55%	40%	50%
6.9	1.0	79%	53%	69%	33%	12%	26%	56%	32%	48%
6.9	1.6	86%	47%	69%	36%	36%	36%	61%	41%	52%
6.9	2.8	86%	50%	70%	34%	40%	37%	60%	45%	53%
6.8	4.4	79%	53%	68%	32%	35%	34%	56%	44%	51%
8.3	1.6	92%	52%	74%	27%	31%	29%	60%	41%	52%
8.2	2.3	88%	55%	74%	32%	34%	33%	60%	45%	54%
8.3	4.8	77%	81%	78%	32%	10%	26%	54%	45%	52%
11.5	1.3	89%	67%	82%	19%	3%	14%	54%	35%	48%
11.8	2.8	94%	66%	83%	25%	32%	28%	59%	49%	55%
11.5	4.2	92%	64%	80%	22%	33%	27%	57%	49%	54%
Desiccant solution-flow : bottom-to-top , extra insulation										
6.9	1.1	74%	65%	71%	35%	-9%	23%	55%	28%	47%
6.9	1.6	76%	102%	81%	41%	-27%	27%	59%	37%	54%
6.9	2.8	78%	72%	76%	37%	18%	32%	58%	45%	54%

Table C-4. Uncertainty associated with counter-cross-flow RAMEE performance during winter testing

NTU	C_{sol}/C_{air}	Uncertainty								
		Supply LAMEE			Exhaust LAMEE			RAMEE		
		Sensible	Latent	Total	Sensible	Latent	Total	Sensible	Latent	Total
Desiccant solution-flow : bottom-to-top										
3.8	1.2	2%	3%	2%	2%	4%	2%	1%	2%	1%
3.8	2.0	2%	4%	2%	2%	4%	2%	1%	3%	1%
3.8	2.8	2%	4%	2%	2%	4%	2%	1%	3%	1%
3.8	4.1	2%	4%	2%	2%	4%	2%	1%	3%	1%
6.9	1.0	4%	5%	3%	2%	5%	2%	2%	3%	2%
6.9	1.6	4%	4%	3%	2%	3%	2%	2%	3%	2%
6.9	2.8	4%	4%	3%	2%	3%	2%	2%	3%	2%
6.8	4.4	4%	4%	3%	2%	4%	2%	2%	3%	2%
8.3	1.6	6%	4%	4%	2%	4%	2%	3%	3%	2%
8.2	2.3	5%	5%	4%	2%	4%	3%	3%	3%	2%
8.3	4.8	5%	8%	4%	2%	6%	2%	3%	5%	2%
11.5	1.3	7%	7%	5%	2%	6%	2%	4%	5%	3%
11.8	2.8	8%	7%	5%	2%	4%	3%	4%	4%	3%
11.5	4.2	8%	7%	5%	2%	4%	3%	4%	4%	3%
Desiccant solution-flow : bottom-to-top , extra insulation										
6.9	1.1	4%	7%	3%	2%	8%	2%	2%	5%	2%
6.9	1.6	4%	12%	4%	2%	13%	2%	2%	9%	2%
6.9	2.8	4%	7%	3%	2%	6%	2%	2%	4%	2%